



Cross section of the $^{13}C(\alpha, n)^{16}O$ reaction at low energies

Ph.D. thesis
submitted October 31, 2018

PhD Candidate
Giovanni Francesco Ciani

Advisors

Dot. rer. nat. Alba Formicola
INFN, Laboratori Nazionali del Gran Sasso

Prof. Filippo Terrasi
Università degli Studi della Campania
INFN, Napoli

Alla Felicitá

"Je buvais à pleins verres les étoiles"
Les Fiançailles, Guillaume Apollinaire

Contents

Introduction	xv
1 Introduction to the problem	1
1.1 Cross section and reaction rate in Nuclear Astrophysics	1
1.1.1 The astrophysical factor S(E)	2
1.1.2 The reaction rate and cross section	4
1.2 Relevance of the $^{13}\text{C}(\alpha, n)^{16}\text{O}$ reaction	5
1.2.1 Background signal in the spectroscopy of geoneutrinos	8
1.3 The State of the art	9
2 The LUNA experiment	17
2.1 The LUNA setup	17
2.2 Measurement of background reduction	19
2.3 A feasibility study for $^{13}\text{C}(\alpha, n)^{16}\text{O}$ reaction at LUNA 400	26
3 The setup characterization	29
3.1 Neutron detectors	29
3.2 Detector design	31
3.3 The experimental LUNA setups	42
3.4 Experimental efficiency measurements	50
4 The target characterization	63
4.1 Target preparation	63
4.2 Experimental quantities	66
4.3 Target characterization at 2 MV Tandetron at MTA ATOMKI .	69
4.4 Target characterization at LUNA accelerator	77
4.5 Conclusions after the characterization	84
5 Data analysis and results	85
5.1 The gamma shape analysis with $^{13}\text{C}(p, \gamma)^{14}\text{N}$	85
5.2 $^{13}\text{C}(\alpha, n)^{16}\text{O}$ cross section at low energy	97
5.3 Results and uncertainties	102
Conclusions	107
A Measurement runs	111
Bibliography	124

List of Figures

1.2	The presence of a sub-threshold resonance can influence the behaviour of the astrophysical S(E)-factor extrapolation, giving a wrong estimation at low energies	3
1.4	Hertzsprung-Russel diagram	5
1.5	(Colour online) AGB star structure (not in scale): an C-O core is surrounded by a He burning shell. This is separated from an outer H burning shell by an He rich intershell region. The external convective envelope is at the surface.	7
1.6	AGB star evolution over time	8
1.7	Level scheme of the ^{17}O compound nucleus	10
1.8	NACRE S(E)-factor extrapolation of $^{13}C(\alpha, n)^{16}O$	12
1.9	Heil's extrapolation R-matrix fit	14
1.10	R-matrix fit with THM parameters.	14
2.1	The LUNA accelerator and the two beamlines	18
2.2	The LUNA solid beam line	18
2.3	The total muon flux measured for the various underground sites as a function of the equivalent vertical depth	20
2.5	Setup for the commissioning of the 3He counters	23
2.6	Comparison of neutron background measured in a surface lab (blue spectrum) and in the LNGS Underground (black spectrum). The flux was measured using 18 unshielded 3He counters.	23
2.7	Particular of an 3He background spectrum acquired in the underground lab of LNGS. The red bars and the blue ones indicates the neutron peak and the integration region for the alpha intrinsic background, respectively.	24
2.8	Comparison of LNGS neutron background measured with two different 3He counters. Blue spectrum refers to the stainless steel, while the red spectrum to aluminum.	25
2.9	(Colour online) Detection limit according to Rucker's Formula: the green and the blue line indicate the Detection Limit L_d for a measurement in LNGS underground measurement and in a surface Laboratory, respectively	27
2.10	(Colour online) The corrective factor due to the electron screening effect calculated with and adiabatic approximation	28
3.1	Example of an arrangement of 12 counters with an active length of 40 cm in one ring. Detectors are embedded in the polyethylene block. The central hole mimics the target chamber.	32

3.2	(Colours online) Overall setup efficiency as a function of the distance of the counters from the target. The simulation was carried out with 12,16 and 18 counters (dot dashed blue, continuous red, dashed green lines, respectively). Increasing the number of counters the minimum distance necessary to allocate all the counters becomes larger	33
3.3	Example of arrangement of He3 counters in two concentric rings: in this case $N_1 = 5, N_2 = 9$	33
3.4	Efficiency as a function of neutron energy for different counters' length	34
3.5	Efficiency as a function of neutron energy for different number of counters configurations	35
3.6	(Colour online) The efficiency of ^3He detector array as a function of r_1 and r_2 , simulated with an isotropic source emitting 2.5 MeV neutrons. The values have been obtained keeping the number of counters in each ring at $N_1= 6, N_2 = 12$, with active lengths $L_1= 25 \text{ cm}, L_2= 40 \text{ cm}$, respectively. The internal radius is 30 mm.	36
3.7	(Colour online) The efficiency of 3He detector array as a function of r_1 and r_2 , simulated with an isotropic source emitting 2.5 MeV neutrons. The values have been obtained keeping the number of counters in each ring at $N_1= 6, N_2 = 12$, with active lengths $L_1= 25 \text{ cm}, L_2= 40 \text{ cm}$, respectively. HR is The internal radius is 35 mm.	37
3.8	Efficiency of the setup as a for two different size of the target chamber	38
3.9	Efficiency as a function of polyethylene size. The L_z , the dimension parallel to the counter direction, is fixed at 50 cm. Even with an increase of the L_x and L_y the efficiency fluctuates within relative 2%	39
3.10	Geometry for the environmental background. Neutrons are generated on the surface of a 2 m radius sphere, in transparent red in Figure, with the direction toward the polyethylene.	40
3.11	Efficiency as a function of neutron energy for the setup in case of a pointlike beamspot (red curve), a centered extended 2D gaussian beamspot (blue curve) and a not centered extended 2D gaussian beamspot. The efficiency is always the same within relative 1%	41
3.12	The study of systematic uncertainties due to mis disposition of 3He counters in the polyethylene matrix: green, light blue and violet solid lines represents the efficiency curves with a mis disposition of counters along the z axis, in the x-y plane and with an asymmetric polyethylene shielding, respectively They are normalized to the correct position of counters (black lines)	42
3.13	Geant4 visualization of the Multi Target setup	43

3.14 (Colour online) Single target setup efficiency as a function of neutron energy: black stars are the overall efficiency, the blue and the red lines are respectively the partial efficiency related to the outer and inner rings of the detector	44
3.15 The MT holder, where three targets can be inserted in the chamber and can be changed without breaking the vacuum, preserving the measurement conditions	45
3.16 Geant4 visualization of the Multi Target setup	46
3.17 (Colour online) Efficiency as a function of neutron energy for the Multi Target chamber setup: black stars are the overall efficiency, the blue and the red lines are respectively the partial efficiency related to the outer and inner rings of the detector	46
3.18	47
3.19 Picture of the setup used for the $^{13}\text{C}(\alpha, n)^{16}\text{O}$ cross section measurement	48
3.20 Cartoon of the setup	49
3.21 Comparison between environmental background and the AmBe spectrum	49
3.22 Scheme of the neutron detection electronics chain	51
3.23 The Americium Berilium spectrum	51
3.24 Safety Sheet of the 10 n/s AmBe source available at LNGS . .	52
3.25 The source mounted in the two setup: in (A) and (B) are shown the ST target holder and the MT target holder, respectively . .	52
3.26 Example of spectrum acquired with the AmBe source mounted inside the LUNA detector. The peak is fitted with the Function 3.3 (red line)	54
3.27 AmBe simulated spectrum implemented in the primary generator Geant4 code: red dots are the reference value from /hypernews.slac.stanford.edu	55
3.28 Setup used for the activation measurement: the ^{51}V target irradiated with proton is inserted in the blue container, shielded by external environmental background	57
3.29 An example of γ -ray spectrum from the ^{51}V decay. The 320 keV peak is fitted with a Gaussian curve plus a linear background.	57
3.30 A neutron spectrum acquired during the efficiency campaign with the $^{51}\text{V}(p, n)^{51}\text{Cr}$ reaction: the neutron peak is evident and the pulser peak is at higher energies	58
3.31 Scheme of the activation measurement. At T_0 a number of $N_{51\text{Cr}}$ are produced after the proton irradiation of ^{51}V . The activation measurement start after a time transient in T_1 . at half of the irradiation measurement the Number of ^{51}Cr nuclides is $N_{1\text{Cr}51} = N_{51\text{Cr}} e^{-\lambda(T_{av} - T_0)}$	58
3.32 Comparison between efficiency experimental blue points calculated with the $^{51}\text{V}(p, n)^{51}\text{Cr}$ reaction and the MC Geant4 efficiency red curve scaled of a factor 0.82 to overlap data.	60
3.33 Comparison between efficiency experimental acquired with the Multi Target setup. The blue points are calculated with the $^{51}\text{V}(p, n)^{51}\text{Cr}$ reaction and the MC Geant4 efficiency red curve is scaled down of a factor 0.82 to overlap data.	61

3.34 Comparison between efficiency experimental acquired with the Multi Target setup. The blue points are calculated with the $^{51}V(p,n)^{51}Cr$ reaction and the MC Geant4 efficiency red curve is scaled down of a factor 0.82 to overlap data.	61
4.1 The evaporation setup: on the left the vacuum chamber and on the right the control panel for the beam, the vacuum system and the monitoring of the quartz. All these parts will be described in next sections.	65
4.2 The vacuum chamber and all the main components: in white the hole where the electron beam comes from, in red the melting pot of the material, in green the nipper where the backing is hold, in light blue the quartz used to monitor the evaporation process.	65
4.3 Beam controller	66
4.4 Enriched ^{13}C target evaporated: It is visible on the top the lighter zone where the target was hold during the evaporation procedure	66
4.5 The setup used at MTA Atomki for the measurement of the $^{13}C(p,\gamma)^{14}N$ reaction; the HPGe is at 0° respect to the beamline direction	69
4.6 Example of spectrum acquired, the red part is the ROI used for the analysis.	70
4.7 (Colour online) Comparison between the spectrum acquired during the $^{13}C(p,\gamma)^{14}N$ measurement and a background, in red and in blue respectively. Spectra are normalized to time. In the region of interest the background is negligible.	71
4.8 The excitation function of the $^{13}C(p,\gamma)^{14}N$ reaction at $E_R = 1748$ keV. Parameters of the fit are listed in Table 4.2	72
4.9 Evaporation uniformity test on ^{13}C targets	73
4.10 Plot of the thickness of the target measured with the resonance scan and the thickness monitored online with the evaporator: the Pearson correlation coefficient shows a moderate correlation	74
4.11 Comparison of the $^{13}C(p,\gamma)^{14}N$ excitation function of a natural carbon and an enriched one (blue squares and red points, respectively). Uncertainties are at the level of 3%.	75
4.12 Level scheme of the ^{14}N compound nucleus. The cyan area indicates the energy window that could be exploited by the LUNA accelerator. In brackets the proton energy needed to populate a level beyond the Q value. No resonant states can be populated with the LUNA machine	77
4.13 (Color online) The tail of the $E_r = 551$ keV resonance and the direct capture component are plotted as a function of energy separately. The ratio between the two is on right Y axis.	78
4.14 The set up used for the ^{13}C target characterization, described in the text.	79
4.15 Spectrum emitted from the $^{13}C(p,\gamma)^{14}N$ with a proton energy $E_p = 1748$ keV. The red zone indicates the integration Region of interest for the Yield evaluation.	80

4.16 Yield in the ROI of the peak DC→ GS as a function of the cumulative charge: error bars include statistical uncertainties and a 3% of systematic uncertainty due to the reading of the charge: the degradation estimated is 17% after 33 C of protons.	81
4.17 Gamma spectrum of the $^{13}\text{C}(p, \gamma)^{14}\text{N}$ reaction at $E_p = 310$ keV. The total charge accumulated is 5.7 C.	82
4.18 Spectra acquired for the evaluation of possible Alpha Beam Induced Background: blue, green and red spectra are the natural background, the blank backing and the natural target, respectively.	83
 5.2 (Colour online) Comparison $DC \rightarrow GS$ transition in γ -ray spectra acquired on the same target at different accumulated alpha charge: blue, red, green and violet spectra have been acquired on a fresh target and after 1C, 2C and 3C of alpha, respectively. The yield decreased clearly with the increasing of the cumulative charge.	88
5.3 Simulation of straggling effect	89
5.5 Full width half maximum of HPGe	91
5.7 Inactive contribution to stopping power for different pollutants with appropriate values of N_i/N_a	93
5.10 Gamma Shape Fit	95
5.11 Stoichiometric ratio as a function of cumulative charge	96
5.12 Gamma Shape Fit	97
5.13 Probability density function of alpha energy due to straggling effect in a target of 180 nm	98

List of Tables

1.1	Overview of the ANC parameter in literature for the $E_x=6356$ keV state of ^{17}O	11
1.2	Direct measurements summary	11
2.1	Background measurements in LNGS	21
2.2	Neutron background measured in different international Underground Laboratories	22
2.3	Counts per month in the region on interest of neutron spectra between $900 < E < 1100$ keV. The maximum limit is 300 counts/months for the validation of each counter	24
2.4	$^{13}C(\alpha, n)^{16}O$ reaction rate as a function of alpha energy. Calculation are based on quantities specified in the text and on cross section by Heil.	26
3.1	Main specification of 3He counters by GE	31
3.2	Radii of the two rings that maximise the setup efficiency for two different target chambers target chamber Radii	37
3.3	Rejection factor of the setup for different neutron energies	40
3.4	Features of the Single Target Chamber	43
3.5	Features of the Multi Target Chamber	45
3.6	Time and neutrons detected in the two rings during the calibration measurements with the 10 n/s AmBe source for ST and MT setup. efficiency is calculated using Formula 3.2.	53
3.7	Results from the fit of the sum spectrum of the Ambe source acquired with the Single Target Setup	54
3.8	Geant4 simulations results with the AmBe source simulated	55
3.9	Parameters used in Formula 3.6 for the efficiency evaluation with the $^{51}V(p, \gamma)^{51}Cr$ reaction.	59
3.10	Single target setup efficiency measurements	59
3.11	Multi target setup efficiency measurements	60
4.1	Setting of the evaporator parameters	66
4.2	Parameters extracted from the fit of the excitation function in Figure 4.8	71
4.3	Fit parameters from the resonance scan in P1,P2,P3	72
4.4	Summary of the parameters of the evaporated targets produced in November 2017	74
4.5	Parameters of the resonance at $E_R = 551keV$	78
4.6	Measurement performed with the LUNA400 accelerator for the characterization of one ^{13}C target	80
4.7	Quantities measured for the evaluation of possible Alpha Beam Induced Background	83

5.1	Scheme of a cycle of measurement for a ^{13}C target	86
5.2	Full Width Half Maximum fitted for three secondary peaks: in the last column the extrapolation at 7843 keV.	90
5.3	Fit parameters for a target (T12). In the right part of the table there are the parameters fit with the proton run analysis; on the left part the are the extrapolated stoichiometric ratio used during the alpha run analysis.	96
5.4	Summary of measurements performed in the first campaign: the charge Q_{tot} accumulated and the number of net counts N_n have been used to evaluate the reaction yield	100
5.5	Cross section evaluated considering different possible inactive nuclei in the analysis. Values agree within the uncertainties. . .	102
5.6	Experimental cross section	103
5.7	Experimental S(E)-factor of $^{13}\text{C}(\alpha, n)^{16}\text{O}$	103

Introduction

Humanity has always been linked with the sky and the stars.

All the elements heavier than helium are only produced in stars, in the so called nucleosynthesis processes.

A star is a gaseous system in equilibrium between the gravitational force, which would lead to the stellar collapse and the stellar pressure (gas + radiation pressure) which counteracts the gravity force. But a star is hot and thus irradiates photons from the surface. The energy produced in these reactions balances the energy losses from the surface, allowing stars to evolve and live for billions of years. Almost all the light elements up to lithium are produced in the so called Big Bang Nucleosynthesis, in the 3 minutes immediately after the Big Bang. Nuclei up to iron ($Z < 26$) are produced by means of nuclear fusion processes between charged particles. Charged particle fusion reactions producing elements heavier than iron are endothermic processes. The nucleosynthesis after iron continues mainly through neutron capture processes: the s-process and the r-process.

The main candidate as neutron source for s process in the low mass ($1 < M/M_{\odot} < 4$) Asymptotic Giants Branch (AGB) stars is the $^{13}\text{C}(\alpha, n)^{16}\text{O}$ ($Q = 2.2216 \text{ MeV}$) reaction [1]. Typical temperature of this stellar environment is $T = 10^8 \text{ K}$, that corresponds to an energy range $140 < E < 230 \text{ keV}$. The knowledge of the cross section with a small uncertainty in this energy window, the Gamow window, permits to constrain the reaction rate and improving the astrophysical models. The main problem is that these astrophysical energies are well below the Coulomb potential, so cross section is extremely low in the order of picobarn.

Previous works in literature have provided cross section at high energies with large uncertainties, mainly due to high Earth surface neutron background and to the difficulties to keep under control the target behaviour during the alpha irradiation. The lowest point measured with a direct measurement has been performed at $E = 280 \text{ keV}$ [2], with an uncertainty larger than 50%.

One needs to approach the low energies cross section values through extrapolation procedures: in the case of the $^{13}\text{C}(\alpha, n)^{16}\text{O}$ reaction, this is more complex since a near threshold resonance of the ^{17}O compound nucleus extends its tail up to the Gamow window. However indirect measurement methods, such as ANC [3] and Trojan Horse Method [4] can measure the cross section inside the Gamow window, but in any case they need normalization with respect to direct data. An accurate direct measurement approaching the Gamow window is mandatory.

My Phd work has been devoted to the $^{13}\text{C}(\alpha, n)^{16}\text{O}$ reaction absolute cross section measurement in the framework of the Laboratory for Underground Nuclear Astrophysics (LUNA) experiment [5].

The 400 kV accelerator is installed in the Underground Gran Sasso National

Laboratory: thanks to the 1400 m of rocks (3400 meters of water equivalent) the cosmic background is strongly suppressed with respect to Earth surface: muonic component is reduced by six orders of magnitude, neutron component by three orders of magnitude.

For the first time, the LUNA collaboration faces out a neutron measurement. In this scientific framework, I strongly contributed to the development and characterization of the first neutron detector with a low intrinsic background, ideal to measurements of rare events a low background environment.

In Chapter 1, I will elucidate the astrophysical importance of the $^{13}\text{C}(\alpha, n)^{16}\text{O}$ reaction as a seed of s process. I will give an overview on the state of the art of the measurement, pointing out the sources of the present uncertainties in the literature works.

In Chapter 2 I will illustrate the advantages of the underground laboratory to measure low cross sections, due to the strong suppression of the cosmic background. In the last section I will carry out a feasibility study that confirms the need of an underground measurement.

In Chapter 3 I will present the two setups that have been designed for the neutron measurements: the Multi Target Setup and the Single Target Setup. We built detectors based on a 18 ^3He counters with a low intrinsic background array, embedded in a polyethylene moderator. Firstly I developed a simulation code based on Geant4 libraries, for designing a high efficiency setup and at the same time compact and easy to handle.

The efficiency curve evaluated with simulations was validate by a devoted experimental campaign performed at MTA Atomki (Debrecen, Hungary).

In Chapter 4 I will get into the heart of this PhD work, describing the target preparation campaign that I personally coordinated. Targets have been produced at MTA Atomki evaporating 99% enriched ^{13}C powder on tantalum backings. Target monitoring turned out a crucial aspect to keep low the systematics uncertainties, so I made big efforts in order to characterize the targets used for the measurements: two complementary campaigns have been scheduled. In the first step, immediately after the evaporation, the thick target yield approach with the $^{13}\text{C}(p, \gamma)^{14}\text{N}$ wide resonance at $E_{p,lab} = 1748$ keV was exploited at the 2MV tandem installed at MTA Atomki. In the second step the direct capture component at lower energies was used for the LUNA campaign and the stability of targets under high intensity proton beam was tested.

In Chapter 5 an innovative analysis developed to take into account the ^{13}C target modification due to an irradiation with an intense alpha beam is described: an alternation of proton beam and alpha beam has been thought to properly correct the data acquired.

I have measured cross section in energy range $260 < E < 305$ keV, reaching the lowest point measured with a direct measurement. Thanks to the accurate analysis the overall uncertainties of the cross section is unprecedentedly of 15%.

In the last paragraph of the fifth Chapter results are compared with literature and discussed.

Chapter 1

Introduction to the problem

In this chapter I will introduce the main concepts of nuclear astrophysics reactions, and how measurements at stellar energies, in the so called Gamow energy region, influence the reaction rate (section 1.1).

According to the stellar mass, the stellar evolution is different, but the common aspect is that the energy necessary to balance energy losses from the stellar surface is produced from nuclear fusion processes.

These nuclear processes, are also responsible for the nucleosynthesis processes: indeed two light nuclei produce an heavier one and emit other reaction products (γ -rays or other charged particles).

All the elements up to iron are synthesized by means of charged particle nuclear fusion.

These processes become endothermic for nuclei heavier than Iron, so the production of heaviest nuclei ($Z > 26$) is possible through subsequent neutron capture processes: slow neutron captures (Section 1.2) (*s-process*) or rapid neutron captures (*r-process*).

In my PhD work I will focus on the main neutron source for the *s* process in low mass Asymptotic Giants Branch (AGB) stars: the $^{13}\text{C}(\alpha, n)^{16}\text{O}$ reaction. I will, briefly, overview the nuclear aspects of the $^{13}\text{C}(\alpha, n)^{16}\text{O}$ reaction and state of the art (Section 1.3).

Several authors studied this reaction through direct and indirect methods. Despite the experimental efforts performed, cross section values are provided with large uncertainties, at the expense of astrophysical models that need cross sections within a precision of 10% in the stellar energy region of interest.

1.1 Cross section and reaction rate in Nuclear Astrophysics

In the hot stellar internal environments atoms are mainly totally ionized. The matter is a plasma of free electrons and charged nuclei in equilibrium with the radiation which is, in mean, neutral. Radiation and particles are in thermodynamical equilibrium, thus the distribution of particles' velocities inside stars can be described by the Maxwell-Boltzmann distribution with an average temperature T .

Charged nuclei repel each other due to the Coulomb force, proportional to the nuclear electric charge, generating the so called Coulomb barrier.

Only when this is overcome (or penetrated thanks to the tunnel effect) charged particle nuclear fusion reactions can occur.

The average energy of nuclei $E = kT$, where k is the Boltzmann constant, is well below the Coulomb potential.

Classically only projectiles in the tail of the Maxwell Boltzmann distribution would have enough energy.

The Quantum tunnelling effect, however, allows particles with smaller energies to penetrate the Coulomb barrier, so that a nuclear reaction is possible at lower energies with a probability P that, in the s-wave process condition, is

$$P(E) = \exp(-2\pi\eta) \quad (1.1)$$

where $\eta = \frac{Z_1 Z_2 e^2}{\epsilon_0 h v}$ is the so called Sommerfeld parameter, $Z_1 e, Z_2 e$ are the electric charges of the nuclei involved in the reaction and $v \propto \sqrt{E}$ is their relative velocity.

The Maxwell Boltzmann distribution and the probability to overcome the Coulombian barrier have opposite behaviour as a function of energy: the first one decreases with increasing energy, the second rapidly increases.

The product of the two, proportional to the reaction rate, generates a maximum in a narrow energy region: the so called Gamow window.

This energy range is the optimal energy for reactions at a given temperature in the star, placing very strong constraints on the charged-particle reactions responsible for producing fusion energy in stars and consequently on their reaction rates.

An example of this convolution is shown in Figure 1.1, assuming an average stellar temperature of 10^9 K. Blue and yellow curves represent the Maxwell-Boltzmann distribution and the tunnelling probability. The green curve is their convolution: the peak is around 200 keV.

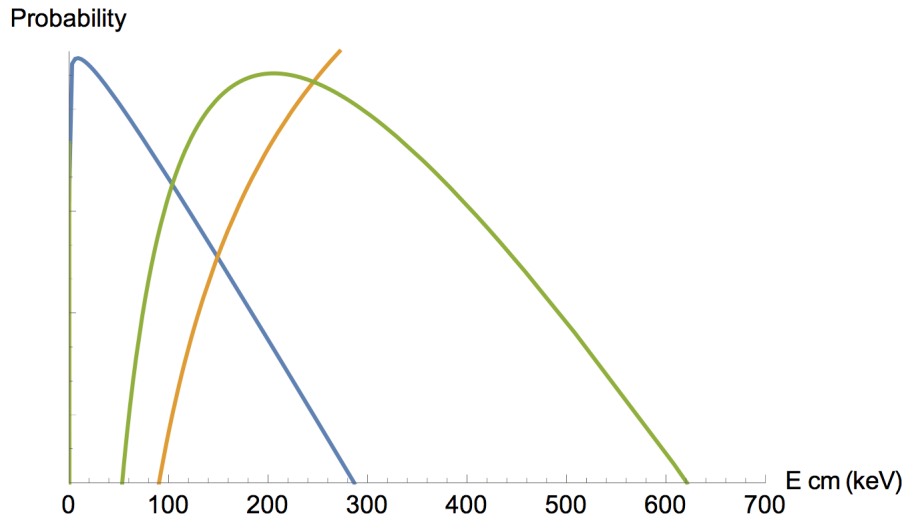


FIGURE 1.1: (Colour online) Illustration of the Gamow peak as a product of Maxwell-Boltzmann energy distribution and tunnelling probability, represented by the green, blue and yellow solid lines, respectively.

1.1.1 The astrophysical factor $S(E)$

The cross section $\sigma(E)$ is directly proportional to the above mentioned probability of overcoming the Coulomb barrier: $\sigma(E) \propto e^{-2\pi\eta}$, where the energy

dependence is in the Sommerfeld parameter η .

At the same time, in a classical treatment, it is also proportional to the geometrical area of projectile and target nucleus: $\sigma(E) \propto \lambda^2 \pi \propto 1/E$.

For these reasons it is possible to factorize the cross section as:

$$\sigma(E) = \frac{1}{E} S(E) e^{-2\pi\eta} \quad (1.2)$$

where $S(E)$ is called astrophysical $S(E)$ -factor. It contains all the strictly nuclear effects and for nonresonant reactions it is a smooth function of energy.

Factoring out the exponential dependency on energy, the astrophysical factor varies much less rapidly than the cross section with the decrease of energy, allowing a more robust extrapolation in the astrophysical energy range of interest.

Nevertheless the extrapolation procedure, based on high energy data, can cause an additional uncertainty due to the possible presence of a near(sub-)threshold resonance that could dominate the $S(E)$ -factor at lower energies.

A sketch illustrating this is shown in Figure 1.2 [6].

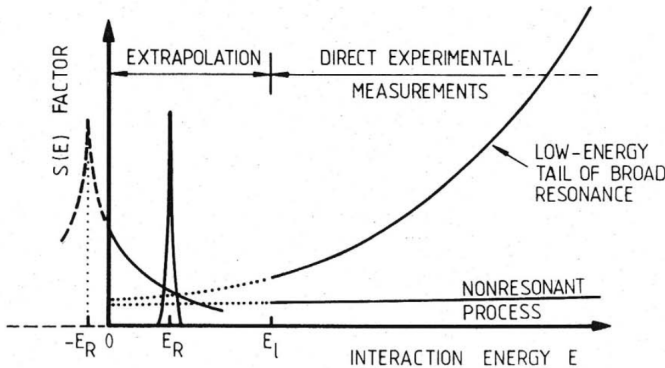


FIGURE 1.2: A sub-threshold resonance influences the behaviour of the astrophysical $S(E)$ -factor: the extrapolation would give a wrong estimation at low energies[6].

Another issue is the electron cloud surrounding the interacting nuclei that lead to a screened cross section which is larger than the bare nucleus one: in the stellar plasma, indeed, nuclei are fully ionized. This condition does not occur during the laboratory measurement. In the latter case the attractive force between the electron cloud around the target and the projectiles makes Coulomb barrier thinner and the probability to overcome it becomes larger: this is the so called electron screening effect.

This generates an enhancement in the $S(E)$ -factor, so that a correction of the experimental data is mandatory in order to take into account this effect, as shown in Figure 1.3 [6].

One common model considers a nearly perfect gas at relatively low density for which the average Coulomb energy between two neighbouring nuclei is much smaller than their thermal energy[7].

A detailed analysis of the problem is described by Rolfs and Rodney [6].

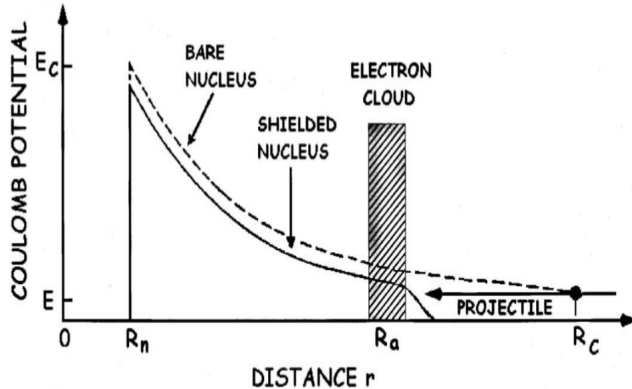


FIGURE 1.3: A sketch of electron screening effect: the Coulomb potential is reduced and drops to zero outside the atomic radius R_a .

Here I would like only to point out that the cross section enhancement is proportional to a factor $e^{U_e/kT}$, where U_e is the potential energy due to the electron screening.

Thus from laboratory measurements and the theoretical treatment of atomic electron screening one should evaluate the cross section of bare nuclei. Then to calculate the rate in the stellar interiors the effect of plasma electron screening must be taken into account (see [8]) In literature several reactions have been studied showing a discrepancy in the measured U_e potential energy with respect to the theoretical value up to a factor 5.

Indirect methods, such as the Trojan Horse Method (THM) are valid approaches to face this problem [9, 10].

In order to overcome these challenging experimental problems, one possibility could be increase the signal to background ratio exploiting an underground accelerator facility.

1.1.2 The reaction rate and cross section

The key quantity in any model of stellar processes is the reaction rate r_{ab} , defined as the number of reactions per unit volume and unit time between two particles a and b .

The understanding of most of the critical stellar features, such as time scales, energy production, and nucleosynthesis of the element strongly hinges on its evaluation.

Defining with N_a , N_b the particle densities of the two particle species, the reaction rate is calculated as in equation 1.3

$$r_{ab} = N_a N_b \langle \sigma v \rangle_{ab} \quad (1.3)$$

where the brackets $\langle \rangle$ indicate the average over the velocity distribution of the particles and the reaction cross section, through the formula:

$$\langle \sigma v \rangle_{ab} = \sqrt{\frac{8}{\pi \mu}} \left(\frac{1}{k_B T} \right)^{3/2} \int_0^{+\infty} E \sigma(E) \exp \left(-\frac{E}{k_B T} \right) dE \quad (1.4)$$

where $\mu = \frac{m_a m_b}{m_a + m_b}$ is the reduct mass of the system projectile-target, T is the average stellar environmental temperature, k_B is the Boltzmann constant. Looking at Formula 1.4, it is clear that an as precise as possible knowledge of the cross section $\sigma(E)$ is crucial to derive the reaction rates and thus describe the dynamics of the nuclear processes in a star for a given astrophysical scenario; the exponential behaviour of the cross section demands a very precise determination of the energy, as well.

1.2 Relevance of the $^{13}\text{C}(\alpha, n)^{16}\text{O}$ reaction

In this section, I will show the evolution of a star through the so called Asymptotic Giant Branch (AGB) Phase, explaining why the $^{13}\text{C}(\alpha, n)^{16}\text{O}$ is so important in this star life path.

The main characteristics of the evolution of a star are determined by its mass; more massive is a star the higher is the internal temperature, the luminosity and the surface temperature. The stellar life can be seen as a sequence of nuclear burnings of heavier and heavier elements spaced out by gravitational contractions during which the internal temperatures increase. The main stellar observables are the luminosity, L , and the surface (effective) temperature, T_e , and thus their evolution is usually represented in a LogL-Log T_e plane, called Hertzsprung-Russel (HR) diagram, shown in Figure 1.4.

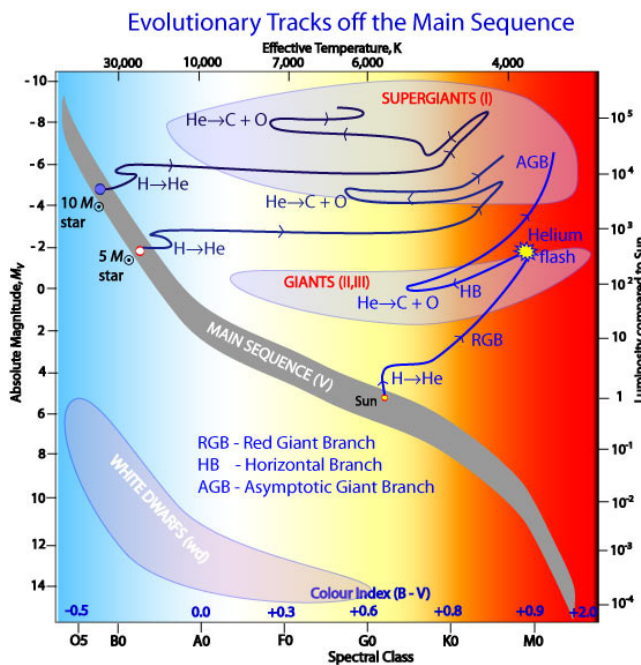


FIGURE 1.4: The HR diagram classifies stars according to their luminosity and temperature. Clusters can be identified as main sequence cutting with a diagonal area the diagram, white dwarfs in the down left corner and giants stars in the upper right corner.

I will not enter in the details of all the main steps of the life of a star, focusing the attention only to the AGB phase, which is the phase in which the $^{13}\text{C}(\alpha, n)^{16}\text{O}$ reaction is active.

All the stars lie in the so called main sequence (MS) region during hydrogen burning processes in the core and according to their mass evolve differently. In stars with mass $1.2 < M/M_{\odot}$, hydrogen fusion is a process passing with continuity from the nucleus to the H shell. The helium nucleus is small and has a low density, and is increased by the H burning through the pp chain that deposits He on the growing helium core. Stars with $1.2 < M/M_{\odot} < 4$ develop a convective nucleus during the MS phase. When the hydrogen is exhausted, a He nucleus bigger than the previous case is generated.

At the same time outer layers, the envelopes, start an expansion process caused by the energy provided by the hydrogen burning. Because the thermal energy is conserved, the outer part of the star becomes warmer, with an average surface temperature of 4000 K, moving to the right part of the HR diagram.

That is the moment when the star becomes a red giant (RG), following a track towards the upper-right hand corner of the HR diagram [11].

Once the temperature in the core has reached approximately $3 \cdot 10^8$ K, helium burning through the 3α -process begins. The beginning of helium burning in the core stops the star's cooling and increases its luminosity.

An analogous process occurs when the helium in the central core is exhausted leaving at the center a C/O core; in the star the fusion of helium in a shell is ignited and starts an expansion phase. At the same time, the outer hydrogen shell becomes cold and becomes inefficient (for low mass stars) or turns off (in big mass stars). The two shells are separated by an intershell region consisting mainly of helium produced during the previous H burning phases. This stage is referred to as the so called early asymptotic giant branch phase (E-AGB).

This puts the star onto the Asymptotic Giant Branch (AGB), a second red-giant phase, almost parallel to the previous one in the HR diagram. The fusion of He into C/O in shell increases the C/O core mass.

During the AGB phase the stellar structure is described by the cartoon in Figure 1.5 : from inner to outer layers we can find a C-O core, an He burning shell, an He-rich layer intershell in radiative equilibrium, a H burning shell and an extended convective envelope.

At the end of the AGB phase the star starts to alternatively ignite the H and He shells (the so called Thermal Pulsing Asymptotic Giant Branch, TP-AGB). In this phase the star experiences strong mass losses until the shells switch off. For low mass stars the residual is the previous C/O core surrounded by very thin layers of He and H (white dwarf star). Due to the expansion mentioned before, He shell moves towards colder and colder regions, and in the end turns off, reigniting the hydrogen shell. The beginning of the thermal pulse process results when the amount of He accumulated by the H burning in the outer shell is enough to compress and heat up again the He rich intershell.

This causes the He reignition and a consequent thermonuclear runaway He flash occurs because the thermodynamic time scale needed to locally expand the gas is much longer than the nuclear burning time scale of the 3α reactions [12].

The intense emission of nuclear energy heats up the He shell that increases its luminosity up to $10^9 L_{\odot}$. The energy released is only partially transmitted

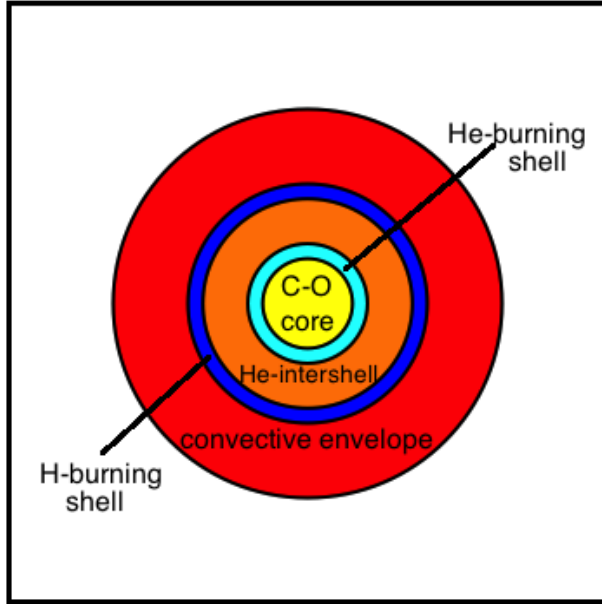


FIGURE 1.5: (Colour online) AGB star structure (not in scale): an C-O core is surrounded by a He burning shell. This is separated from an outer H burning shell by an He rich intershell region. The external convective envelope is at the surface.

in radiative process. Part of it arises convective motions for all the He rich intershell zone, mixing the carbon produced by 3α reactions in the intershell region. The mixing is limited to this region because convection cannot overcome a burning shell.

When the H shell turns off after the expansion of upper part of He shell, convection from the envelope can overcome the quiescent H shell, catching the matter in the intershell and bringing on surface the products of the He burning and the s process element. This is called the Third Dredge Up (TDU), a process that lasts around 200 years. It is clear that, since the thermal pulses are repeated periodically, the third dredge-up event can happen many times. Figure 1.6 from Straniero et al paper [13], shows the structure of a TP-AGB star over time, showing with thick black lines the base of the convective envelope, the H-burning shell, and the He-burning shell. The region between the H and He shells is the helium rich intershell.

The thermal pulses happen every 10^4 years for a C-O core mass of $0.6 < M/M_{\odot} < 0.8$, during which time the star is quiescent (interpulse phases) so the consequent TDU event can happen many times, mixing the star products.

At this point the knowledge of the AGB stars evolution meets another puzzle started when Merrill [14], in 1952, observed the unstable isotope ^{99}Tc ($\tau = 2 \cdot 10^5$ y) in spectra of peculiar S stars (characterized by $\text{C}/\text{O} = 0.7 - 0.9$), enriched in elements heavier than iron.

That could be a clear signal that nucleosynthesis of ^{99}Tc occurred in situ in their interior and that the products were afterwards mixed to the surface. Further works confirmed this observation, so that Sanders [15] proposed that TP-AGB phase was a reasonable place for the so called s process.

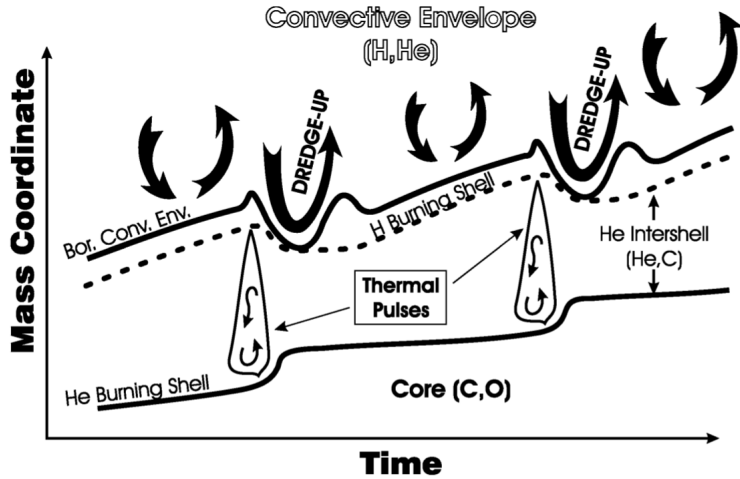


FIGURE 1.6: Positions of the inner border of the convective envelope, the H-burning shell and the He-burning shell, during the thermally pulsing AGB phase as a function of time. The convective regions generated by two subsequent thermal pulses are also shown [13]

These are neutron capture processes responsible of half of the elements heavier than iron, characterized by the fact that the neutron capture half life of the daughter nuclei is shorter than the beta decay half life.

So the astronomers community at that time had to combine the evolution of the stars in the AGB branch with two crucial questions: how s process takes place in AGB stars' core and how the nuclei resulting from s process could appear on stellar surface to be observed.

The solution is exactly the continuous cycle of thermal runaway and consequent Third Dredge Up mentioned above.

I will focus the explanation to low mass AGB stars. Since, in this stellar environment the $^{13}\text{C}(\alpha, n)^{16}\text{O}$ is the main neutron source for the s process mentioned before.

Later on the TDU, a following increasing of the temperature in the He rich intershell arises, and this starts the H burning building ^{13}C nuclides through the chain $^{12}\text{C}(p, \gamma)^{13}\text{N}(\beta^+\nu)^{13}\text{C}$, generating the so called ^{13}C pocket. Here after some time, the temperature reaches values of $\approx 10^8\text{K}$, high enough to generate neutrons by the $^{13}\text{C}(\alpha, n)^{16}\text{O}$ reaction, which triggers the s process.

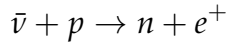
During the star evolution, a large number of He flash can happen according with the star mass so after that s-process material is formed, it is subsequently transported in the stellar envelope.

The stellar temperature of this process can be converted in the Gamow window energy between 140 and 230 keV. So it is crucial to know $^{13}\text{C}(\alpha, n)^{16}\text{O}$ absolute cross section in this energy range in order to improve astrophysical models and nuclides abundance precision.

1.2.1 Background signal in the spectroscopy of geoneutrinos

Geoneutrino researches have been carried out by Kamland [16] and Borexino [17].

These experiments have measured signals of electron antineutrinos produced in the decay chains of Thorium and Uranium in the Earth's crust and mantle. Basic principles of their detection is the interaction of antineutrinos with the protons in the liquid scintillator of the mentioned above experiments via the inverse β decay



The detection occurs with phototubes through the combination of two signals:

- a prompt signal from the slowing down and annihilation of the e^+
- a delayed signal provided by the 2.22 MeV γ -ray from the $p(n,\gamma)d$ neutron capture reaction, which occurs after the neutron has been thermalized.

The organic scintillators used in both neutrinos detector experiments contain around 10 tons of ^{13}C . Despite the big efforts to purify the liquid scintillator [18], impurities of ^{210}Pb are present in this kind of detector, coming from the ^{222}Rn in the Uranium chain. ^{210}Pb is radioactive with a half live of 22.2 y. Through the series $^{210}\text{Pb}(\beta-)^{210}\text{Bi}(\beta-)^{210}\text{Po}$, the granddaughter ^{210}Po is produced.

Also this nuclide is unstable and emits an alpha particle of 5.3 MeV, that interacts with ^{13}C inside the scintillator and the $^{13}\text{C}(\alpha,n)^{16}\text{O}$ reaction takes place. Due to light elements in the scintillator the neutron emitted is easily slowed down.

The $^{13}\text{C}(\alpha,n)^{16}\text{O}$ reaction creates an important background and gives a number of fake events which are comparable to those expected from geo-neutrinos. For detecting geoneutrinos it is mandatory to subtract the fake events in a reliable way, with an overall uncertainty at maximum of 10% in the cross section [19].

As I will explain in the state of the art, Harissolopoulos' results are debated due to a possible unprecise evaluation of the detector efficiency. This makes necessary to improve the $^{13}\text{C}(\alpha,n)^{16}\text{O}$ cross section data in order to constrain better the geoneutrino results.

1.3 The State of the art

A conspicuous number of measurements of the $^{13}\text{C}(\alpha,n)^{16}\text{O}$ cross section have been carried out over the past 45 years. Several investigations of the total cross section for $^{13}\text{C}(\alpha,n)^{16}\text{O}$ at low energies have been motivated by its importance as a stellar neutron source for the s process.

Moreover, further measurements are in progress or already scheduled. A new measurement has been performed in Oak Ridge Laboratory using liquid scintillators in the energy range $E = 0.3\text{--}4.97\text{ MeV}$ ¹. The work is still unpublished.

The n-TOF collaboration foresees to perform the cross section measurements

¹I refer in this work to the energy in the center -of -mass system, unless differently specified.

of the $^{13}\text{C}(\alpha, n)^{16}\text{O}$ reaction in inverse kinematics. Some details are reported in Cristallo et al [1].

Figure 1.7 shows the level scheme of ^{17}O together with the competing exit channel $^{17}\text{O} + \gamma$. In particular, the levels marked in red are interesting for AGB nucleosynthesis.

The Q-value of the reaction is 6.359 MeV [20]. A complication is immediately evident from the figure 1.7. It arises through the existence of a 6.356 MeV state ($J^\pi = 1/2^+$) in ^{17}O that presents a subthreshold resonance at an energy of just -3 keV.

The high-energy tail of this resonance needs to be taken into account for any extrapolation of the $^{13}\text{C}(\alpha, n)^{16}\text{O}$ cross section.

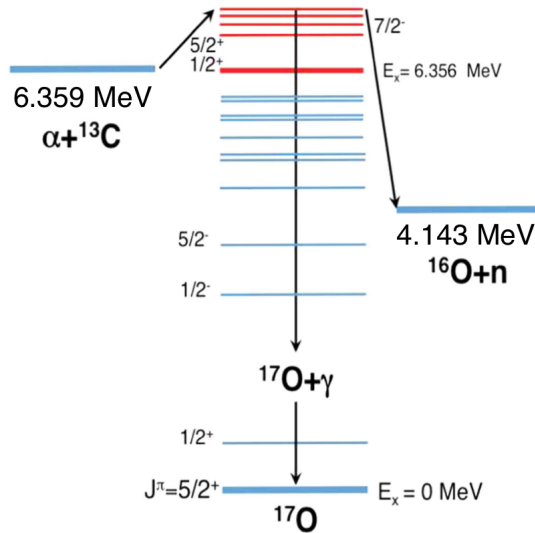


FIGURE 1.7: (Colour online) Schematic diagram of the $^{13}\text{C}(\alpha, n)^{16}\text{O}$ nuclear reaction process, together with the competing exit channel $^{17}\text{O} + \gamma$. The excited states of interest for AGB nucleosynthesis are highlighted in red

The level $E_x = 6356$ keV was measured with an indirect method as the Asymptotic Normalization Coefficient (ANC) method; however a recent work by Keeley et al. [21] found that the uncertainty of 8 keV [22] in its excitation energy causes a limit of a factor 4 in the determination of the $\langle ^{17}\text{O}(1/2^+) | ^{13}\text{C} + \alpha \rangle$ overlap. So they concluded that for near-threshold levels the uncertainty in the value of the excitation energy may have a significant impact on the ANC and this should be tested on a case-by-case basis. An overview of the available data is given in table 1.1.

The very low value of Johnson et al. has been attributed to the non-consideration of an experimental effect during their data analysis [26]. Most of the other measurements agree with the exception of a recent ANC determination by La Cognata et al. that deviates by two sigma from the other data. In 2017 a new analysis on their data by Trippella and La Cognata [27], was performed subsequently to the new results recommended in Faestermann et al. [28] for the $1/2^+$ state: $E_x = 6.3634 \pm 0.0031$ MeV and $\Gamma_n = 0.136 \pm 0.005$ MeV. This reanalysis allowed them to reproduce the ANC value by Avila. Moreover,

TABLE 1.1: Overview of the ANC parameter in literature for the $E_x=6356$ keV state of ^{17}O

Reference	ANC (fm^{-1})
Johnson et al.[23]	0.89 ± 0.23
Pellegriti et al.[24]	4.5 ± 2.2
Guo et al. [25]	4.0 ± 1.1
La Cognata et al.[4]	$7.7 \pm 0.3^{+1.6}_{-1.5}$
Avila et al. [26]	3.6 ± 0.7

Mukhamedzhanov et al. [29] performed a new R-matrix expressions for amplitudes and astrophysical factors of resonant reactions proceeding through subthreshold resonances, and they calculate the astrophysical S(E)-factor for the $^{13}C(\alpha, n)^{16}O$ reaction, finding an agreement with Trippella et al.'s data. One should also note the large uncertainties of the measured ANC of over 20%. It needs to be emphasized that an ANC measurement can only provide the strength of the resonance; it does not give any information if the interference between the subthreshold state and higher-energy ones is constructive or destructive. Constructive interference is normally assumed but destructive interference cannot on the basis of the presently available low-energy data be fully ruled out at the moment. A direct measurement approaching the Gamow Window could help to reduce uncertainty on absolute cross section and to help in understanding the contribution of this state.

All the literature works related to the direct measurements are summarized in Table 1.2.

TABLE 1.2: Direct measurements summary

Reference	Year	Energy range explored (E_{lab})
Sekharan [30]	1967	1.95-5.5 MeV
Davids [31]	1968	0.475 - 0.700 MeV
Biar [32]	1973	1.050-3.300 MeV
Drotleff [2]	1993	0.37-1.050 MeV
Brune [33]	1993	0.6-0.8 MeV
Harissopoulos [19]	2005	0.8-8 MeV
Heil [34]	2008	0.420-0.915 MeV

In the following, I will focus the attention on Drotleff et al. [2] measurements, since their data-set cover the lower energy at $E=280$ keV with an overall uncertainty of 50%, (all the S(E) data are corrected for the electron screening effect). They accelerated an He^+ beam on targets made of 99% enriched ^{13}C deposited on copper backings, with an average current of $\bar{I} = 100 \mu\text{A}$.

The neutrons were detected using ^3He proportional counters embedded in a moderating polyethylene matrix. The low energy points reveal a S(E)-factor enhancement, possibly due to a $1/2^+$ sub-threshold resonance at $E=2$ keV, as it was anticipated by Azjenberg-Selove [35].

Another measurement performed in 1993 by Brune et al [33], focused the attention on the measurement of the new resonances of the $^{13}C(\alpha, n)^{16}O$ reaction, at $E_\alpha = 656$ and 802 keV. These states have been observed for the first time

with their relative resonance strengths. They used a ${}^4He^+$ beam up to 50 μA were provided by the Caltech Pelletron accelerator, impinging ${}^{13}C$ (99.2% enriched) were made by electron-beam evaporation. The setup used was a polyethylene-moderated 4π detector with eleven 3He counters, with a detection efficiency fo 20% for a ${}^{252}Cf$ source.

Brune concluded that the resonance strengths for these two states are too weak, compared to the nonresonant contribution, to affect the stellar reaction rates. These resonance state (the subthreshold by Drotleff and the two new by Brune) were considered by Angulo et al. in the S(E)-factor extrapolation, as reported in the European Compilation of Reactions Rates for Astrophysics (NACRE) [36], leading to $S(0)=2.3 \cdot 10^7$ MeV b.

The S(E)-factors is shown in Figure 1.8.

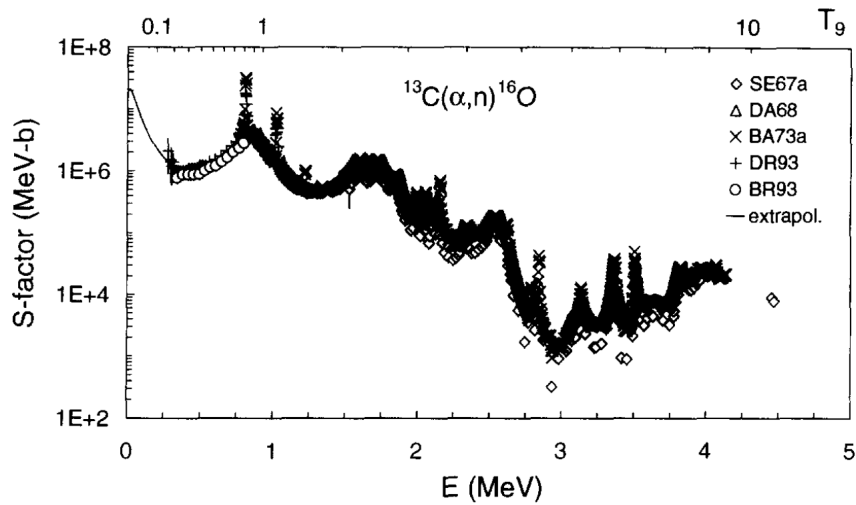


FIGURE 1.8: ${}^{13}C(\alpha, n){}^{16}O$ S(E)-factor extrapolation in the NACRE database [36]

In 2005, Harissopoulos et al. [19] measured the ${}^{13}C(\alpha, n){}^{16}O$ reaction absolute cross section in an energy range $E= 0.6 - 6$ MeV in steps of 8 keV (10 keV in the laboratory system) with a setup similar to Drotleff's one.

The main aim of the measurement was the geoneutrino background subtraction required by neutrino experiments such as Borexino and Kamland, [37]: in Harissopoulos' work an overall uncertainty of 4% was reached.

In 2013, Heil et al. [34] performed a new measurement of the ${}^{13}C(\alpha, n){}^{16}O$ cross section in the energy range $E = 320- 700$ keV.

Heil used a different approach, employing a $n-\gamma$ converter consisting of a Cd-doped paraffin sphere surrounded with 42 BaF_2 γ detectors. In the central hole a neutron converter was installed.

The efficiency of the setup was measured using the non resonant ${}^{51}V(p, n){}^{51}Cr$ reaction with a proton beam at 1700, 2500, and 3500 keV, corresponding to neutron energies of 135, 935, and 1935 keV, respectively.

A detailed uncertainties analysis is described in the paper. The authors considered as the main systematic source the change of target stoichiometry, due to the build up during the beam irradiation.

At higher energies, where systematic uncertainties dominate, overall uncertainties could be reduced to the level of 5%.

In the low energy part the errors are dominated by the low counting statistics.

In addition the double differential scattering cross section $^{13}\text{C}(\alpha, \alpha)^{13}\text{C}$ was measured in the energy range $E_{lab} = 2.6\text{-}6.2$ MeV for 28 angles and these data have been used to constrain possible contributions from background resonances for a reliable extrapolation with the multichannel R-matrix code SAMMY.

Heil's S(E)-factor data were in good agreement with the previous work of Davids, Bair and Haas, and Drotleff et al.

The comparison between Heil's work and previous direct measurements is shown in Figure 1.9. The solid red line and the dashed ones represent the R-matrix extrapolation with its error bars. The green line is the fit where the near threshold resonance is not taken into account.

The uncertainty range of the S(E)-factor curve is dominated by the uncertainty of the resonance parameters of the broad $3/2^+$ state at 7.248 MeV excitation energy as well as by the parameters of the threshold state at 6.379 MeV ($1/2^+$) and of the subthreshold states at 5.923 MeV ($1/2^-$) and 5.868 MeV ($3/2^+$), and by the associated interference pattern. To estimate the uncertainty of the low-energy S factor, the α partial widths of the $J^\pi = 1/2^+$ threshold level as well as of the two subthreshold resonances at $E_{\alpha,lab} = -567$ and -641 keV were varied by certain factors around the parameters of the best fit.

Furthermore, Heil et al. pointed out that in Harissopoulos' paper the assumption of 4% total uncertainty could be not appropriate since their efficiency is mainly based on simulation code; only one experimental measurement was performed with a non monoenergetic ^{252}Cf source even if their data explored a wide neutron energy range.

A recent measurement by Mohr [38] revised Harissopoulos et al.'s data. The correction refers to the energy-dependent efficiency of the neutron detector and appears only above the (α, n) threshold of the $^{13}\text{C}(\alpha, n)^{16}\text{O}$ reaction at about $E_\alpha = 5$ MeV. The corrected data are lower than the original data by almost a factor of 2. The correction method is verified using recent neutron spectroscopy data and data from the reverse $^{16}\text{O}(n, \alpha)^{13}\text{C}$ reaction.

The European Compilation of Reactions Rates for Astrophysics (NACRE) [36] has determined reaction rates using experimental cross sections of previous works [30, 31, 32, 2, 33] covering an energy range between 280 and 4200 keV.

One example of indirect measurement to study the $^{13}\text{C}(\alpha, n)^{16}\text{O}$ reaction is the Trojan Horse Method (THM).

La Cognata et al.[4] applied the THM to the $^{13}\text{C}(^6\text{Li}, n^{16}\text{O})d$ quasi-free reaction.

Figure 1.10 in the paper shows the overlap of the THM S(E)-factor of the $^{13}\text{C}(\alpha, n)^{16}\text{O}$ reaction and the direct data presented previously.

They used the Heil et al. (2008) R-matrix curve for normalization.

After the normalization, a good agreement is found between the THM R-matrix and the direct data.

As already mentioned, indirect measurements are complementary to direct

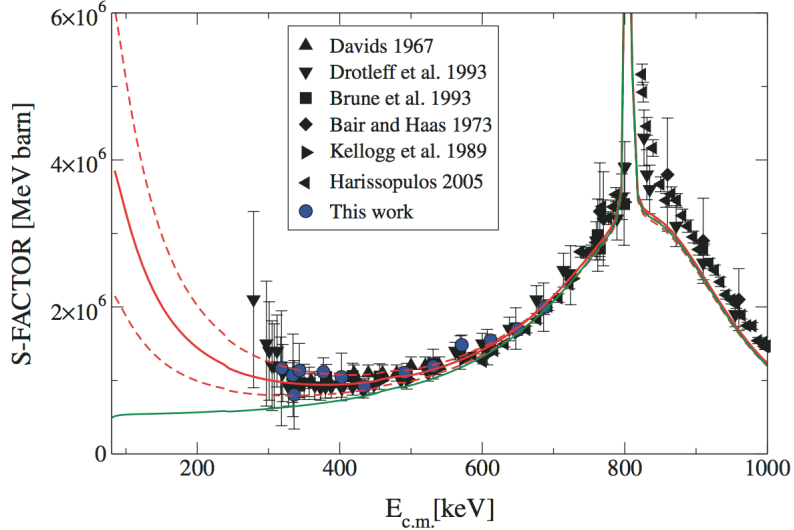


FIGURE 1.9: Extrapolation of the astrophysical $S(E)$ -factor for the $^{13}C(\alpha, n)^{16}O$ reaction down to the Gamow window overlapped to experimental data (This work is Heil [34]). The red solid and dashed lines represents the R-matrix fit with the error bars, respectively. The lower solid green line corresponds to the extrapolation in which the near-threshold resonance was omitted

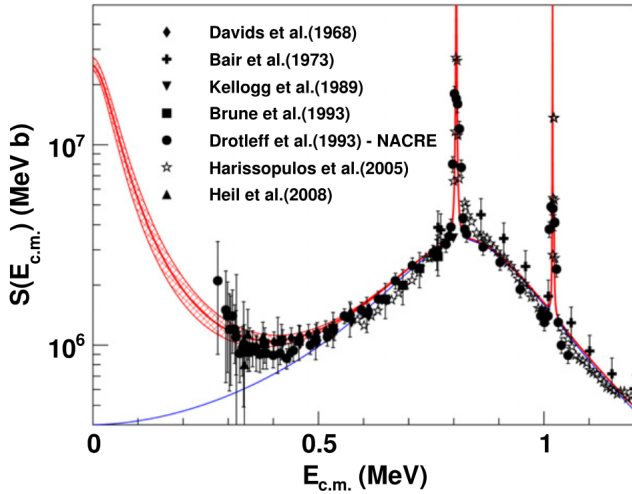


FIGURE 1.10: The $S(E)$ -factor from the R-matrix using the THM resonance parameters is represented by the red line, together with the error band (upper and lower solid red lines). The R-matrix $S(E)$ -factor not including the sub threshold resonance at -3 keV is indicated by the blue line. Different symbols indicates different datasets. The fit is normalized to Heil [34].

ones.

For a good results with indirect techniques, a normalization on direct data with low uncertainties is mandatory.

Coming to the $^{13}C(\alpha, n)^{16}O$ reaction, the rate from Drotleff [2] is about 50% lower than the rate recommended by NACRE in the temperature range of interest ($0.1 < T/GK < 0.3$). Recent $^{13}C(^6Li, d)^{17}O$ -transfer studies by Kubono

et al. [39] suggest a very small spectroscopic factor of $S_\alpha = 0.01$ for the sub-threshold state at 6.356 MeV. This indicates that the high energy tail for this state is negligible for the reaction rate in agreement with the present lower limit. However, a detailed re-analysis by Keeley et al. [21] of the transfer data leads to significantly different results for the spectroscopic factor of the sub-threshold state $S_\alpha = 0.2$ which is lower than the rate suggested by NACRE. A re-evaluation of the rate based on new experimental results, including elastic scattering data, has been performed by Heil [40] and a reaction rate of $(4.6 \pm 1.0) \cdot 10^{-14} \text{ cm}^3/\text{moles}$ at $kT = 8 \text{ keV}$ ($T = 0.1 \cdot 10^9 \text{ K}$) was determined. After the analysis by Trippella and LaCognata [27], the reaction rate was calculated again and compared with the Heil's one: the two rates are compatible almost everywhere, but the greater divergence is just located in the most interesting region for astrophysics, where Trippella calculated a lower reaction rate with a discrepancy at $T = 0.9 \cdot 10^8 \text{ K}$ of around 12%.

This situation requires further experimental study: my PhD work offers a chance to move forward thanks an advanced detector technology, high current and low background accelerator facility.

Chapter 2

The LUNA experiment

In this chapter I will introduce the LUNA, Laboratory for Underground Nuclear Astrophysics, experiment, putting emphasis on the reason why it is installed in an underground laboratory, Laboratori Nazionali del Gran Sasso (Section 2.1).

All the experiments involved in the branch of rare event physics (Dark Matter research, neutrino detection, low energy nuclear astrophysics) need to be shielded from the environmental background.

This can be divided in two main sources : cosmic rays and natural radioactivity.

Building laboratories in caves or mines is a natural solution to the up mentioned problem. For example, the Gran Sasso National Laboratory (LNGS), located in the Gran Sasso massif in Abruzzo (Italy), is escaved below 1400 meters of rocks (3500 m.w.e.).

This reduces the muon flux in the experimental halls by a factor 10^6 ($1 \mu/h/m^2$) and neutron flux by a factor 10^3 (Section 2.2).

As a pilot project for an underground accelerator facility, a home-made 50 kV accelerator was installed in the LNGS underground laboratory. This unique project, called LUNA I, was initiated in the year 1990 by G. Fiorentini and Claus Rolfs and started measurements in January 1994 [41].

I will shortly introduce the current working accelerator, the LUNA 400.

Another pioneering aspect of this measurement is that for the first time in its 25 years live, the LUNA collaboration has the goal to measure a reaction that produces neutrons, approaching the neutron detection techniques and facing the problem of underground neutron background.

In the last part of the Chapter I will show the feasibility tests performed in anticipation of the cross section measurements (Section 2.3).

The benefits for the measurement of the $^{13}\text{C}(\alpha, n)^{16}\text{O}$ reaction will be clear at the end of the chapter.

2.1 The LUNA setup

For more than 25 years, LUNA has provided the opportunity to study nuclear reactions underground at the Gran Sasso National Laboratory (LNGS), located in the Gran Sasso massif in Abruzzo, Italy. Initially using a 50 keV accelerator, in 2000 a new commercial electrostatic accelerator with a radiofrequency ion source was installed underground. The LUNA 400 accelerator can deliver protons and alpha particles with energies from 50 up to 400 keV, with a high accuracy and reproducibility of the beam energy, a beam energy

spread of 100 eV and excellent stability of the beam energy over time [5]. The achievable beam currents on target at LUNA typically are on the order of 100-400 μA . The LUNA facility has two beamlines for different experiments. One of them is currently dedicated for experiments with solid targets, whereas the other beamline hosts a windowless gas target system. Figure 2.1 shows the LUNA accelerator and the two beamlines: the gas target to the right, the solid target to the left.

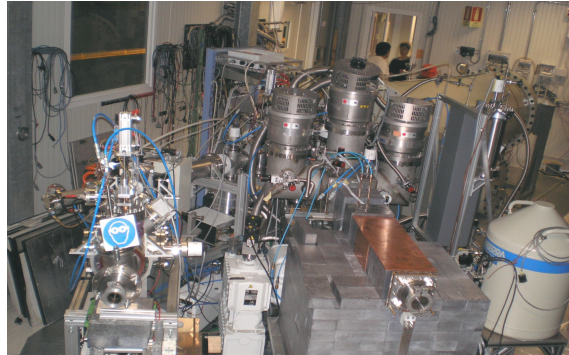


FIGURE 2.1: The LUNA accelerator and the two beamlines

For the $^{13}\text{C}(\alpha, n)^{16}\text{O}$ we used a solid target produced by mean of evaporation of 99% enriched ^{13}C powder on Tantalum Backings: the characterization of this type of target will be described in Chapter 4.

2.1.1 The solid target beam line

The delivery of the beam is possible thanks to the focalization system described in this section.

In Figure 2.2 a sketch of the solid beamline is shown.

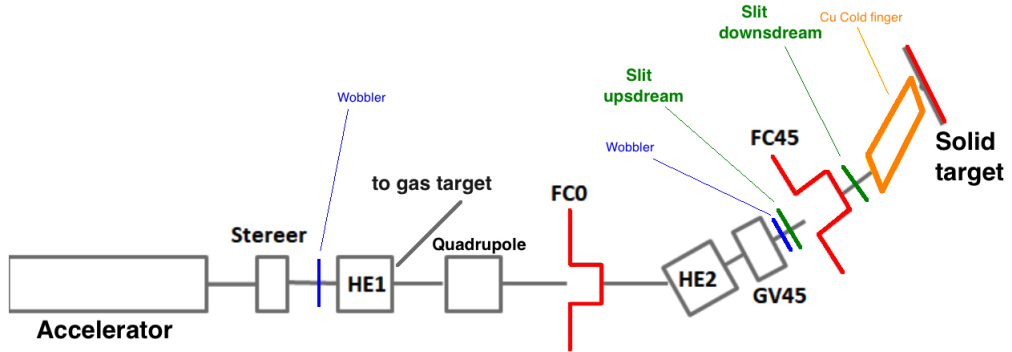


FIGURE 2.2: The LUNA solid beam line

Helium (or hydrogen) gas is ionised using a radio frequency (RF) oscillator in order to produce a source of plasma confined by an axial magnetic field. Once extracted from the source and accelerated, the proton beam is guided

and focused to the target station using a 45° dipole magnet and a vertical steerer. Insertable Faraday cups positioned before and after the 45° magnet allow monitoring of the beam current, which is essential in order to optimise the beam focussing. Two tantalum slits are mounted just before and after the FC45, to define the size and shape of the beam without hitting the target holder.

Immediately before entering in the target chamber, the beam passes through a liquid nitrogen (LN_2) cooled copper tube that serves to reduce beam-line contaminants and prevents the build-up of carbon on the target surface. A bias voltage of -300 V was applied to the copper tube to suppress secondary electrons emitted when protons strike the target.

Another important feature of the experimental apparatus is the cooling system: assuming the maximum delivered voltage and current, 400 kV and 400 μA respectively, the beam power can reach 100 W.

This power could heat up either the collimators, increasing the pressure inside the beamline, or the target, fastening the target degradation. To reduce this effect the two Ta slits and the target backing are directly water cooled by chilled deionized water at 5° C. The target holder at 0° with respect to the beam axis, where the ^{13}C targets (Chapter 4) used in this investigation have been mounted, was isolated from all other beam-line components and acted as a Faraday cup. This allowed to determine the total charge accumulated over the course of a measurement with uncertainties of 3%.

Two detector arrays were used in this PhD work: an High Purity Germanium (HPGe) detector and an array of 3He counters detectors, since γ -ray spectroscopy and neutron detection are involved in my project.

The High purity Germanium (HPGe) detector of relative efficiency 120% (compared with a NaI crystal 3" x 3") was placed at an angle of 55° with respect to the beam axis and a distance of 4 cm from the target surface. The 55° alignment was chosen in order to mitigate any angular distribution effects (as explained in Chapter 4). The detector was mounted on rails to provide access to the target chamber. The neutron detector array used for this experiment consists of 18 individual counters centred axially on the beam line at 0° with respect to the target chamber: a Geant4 rendering of the detection system and target chamber configuration used are described in section 4.

The counters have been embedded in a polyethylene matrix used as moderator. As it will be explained better in Chapter 3, the polyethylene shielding can be open in order to insert the HPGe in close geometry for the γ -ray measurements.

2.2 Measurement of background reduction

The main component of surface background are three:

S.1 muon background coming from cosmic rays

S.2 natural radioactivity

S.3 neutron background from cosmic rays and from fission reaction

For an overground laboratory measurement, the main background component comes from muons. They are generated from cosmic rays arriving on

Earth. The average muon flux at sea level is $200 \mu s^{-1} m^{-2}$.

The origin of cosmic rays is galactic or extragalactic and, they are composed by around 90% from protons and 10% of Helium.

When cosmic rays enter the Earth's atmosphere they collide with atoms and molecules, mainly oxygen and nitrogen. The interaction produces a cascade of lighter particles, a so-called air shower secondary radiation that includes γ -rays, muons, protons, alpha particles, pions, electrons, and neutrons.

In particular charged pions decay during the path, generating muons and neutrinos, that reach the Earth surface.

Being high energetic charged particles with higher mass with respect to electrons, cosmic muons are highly insightful. So they are detected on Earth surface in spite of thick and dense shielding installed outside particle detectors. Muons lose energy by ionization and by radiative processes, e.g. bremsstrahlung.

The muon energy loss is usually parametrized by the formula 2.1

$$-\frac{dE_\mu}{dx} = a(E) + b(E)E_\mu \quad (2.1)$$

where a is the ionization loss and b is the sum of fractional energy loss of the radiative processes [42]. Both parameters are energy dependent.

One crucial advantage for the underground measurements is the cosmic background reduction of many orders of magnitude.

In Figure 2.3 [43] the total muon flux measured for the various underground sites as a function of the equivalent vertical depth is shown.

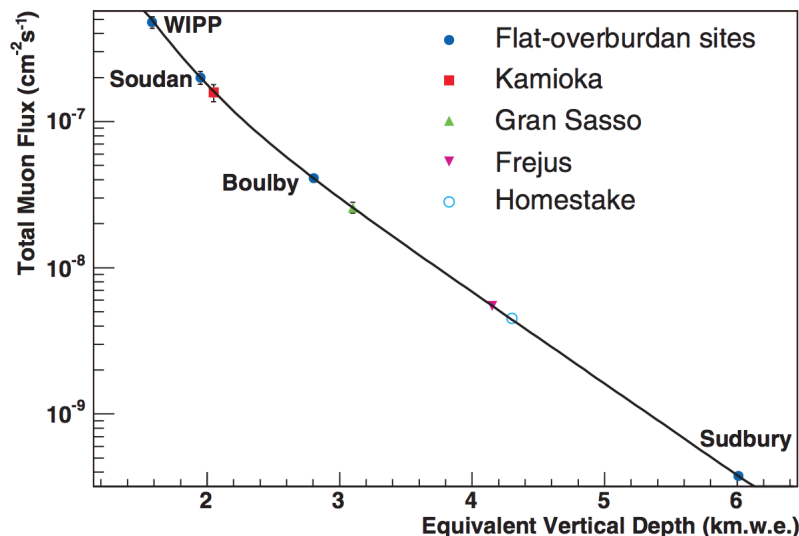


FIGURE 2.3: (Colour online) The total muon flux measured for the various underground sites as a function of the equivalent vertical depth [43]

Thanks to the 1400 m of rock, 3500 m.w.e¹, over Laboratori Nazionali del Gran Sasso, a strong suppression of the muonic and neutron background

¹meter water equivalent

components is reached.

In Table 2.1 the background reduction, defined as the ratio between LNGS flux and the one at Earth surface at sea level, for different background components is summarised.

TABLE 2.1: Background measurements in LNGS

Source	Energy (MeV)	Flux ($cm^{-2}s^{-1}$)	Reduction factor
Muons [44]	all spectrum	$2.52 \cdot 10^{-7}$	10^{-6}
Neutrons [45]	$< 5 \cdot 10^{-3}$	$(0.32 \pm 0.09 \pm 0.04)10^{-6}$	10^{-3}
Neutron [46]	< 1 MeV	$(0.70 \pm 0.14)10^{-6}$	10^{-3}
Gamma [47]	0-0.5	0.17	0.05
Gamma [47]	0.5-1	0.11	0.05
Gamma [47]	1-2.6	0.05	0.05

Figure 2.4 shows the comparison of background spectra acquired using an High Purity Germanium detector (HPGe) as in surface and in LNGS underground laboratory: it is possible to notice how components **S.1** and **S.2** are suppressed.

Up to 2.6 MeV the main contribution of the background comes from natural radioactivity. The highest energy γ -ray is at 2.614 MeV from the ^{208}Tl .

This component is reduced by a factor 20 because of the γ -radioactivity comes also from the rock [44] and can be further suppressed surrounding the detector with lead or copper active shielding.

Beyond the 2.6 MeV peak, only muons contribute to the γ -ray spectrum. This source of background is drastically suppressed of 6 orders of magnitude.

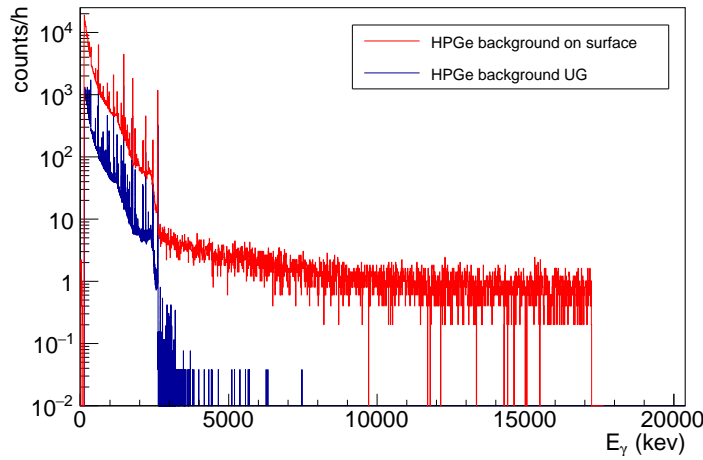


FIGURE 2.4: (Colour online) Comparison of γ -rays background measured with the same HPGe at LNGS in a surface laboratory (red spectrum) and in the LNGS underground (blue spectrum).

2.2.1 Neutron background measurement

Another important source of background is due to neutrons. This comes mainly from fission process in materials and from (α, n) reactions. Moreover, a neutron component is present in secondary cosmic rays.

The natural shielding for underground laboratories permits to reduce also the neutron background by many order of magnitudes, according to the laboratory depth and composition of rocks.

In Table 2.2 [45] low energy neutron background components measured in different underground laboratories all over the World are compared. The average neutron background on Earth surface is $\sim 1 \text{ n min}^{-1}\text{cm}^{-2}$ for the whole energy spectrum. The thermal neutron flux background is $\sim 1 \text{ n s}^{-1}\text{cm}^{-2}$ on the surface (depending on exact location) [48].

TABLE 2.2: Neutron background measured in different international Underground Laboratories [45].

Location	Neutron flux ($10^{-6}\text{cm}^{-2}\text{s}^{-1}$)
WIPP	< 0.06
Soudan	$0.7 \pm 0.08 \pm 0.08$
KURF	< 0.4
LNGS	$0.32 \pm 0.09 \pm 0.04$
SURF (Davis)	$1.7 \pm 0.1 \pm 0.2$

I have performed independent background measurements in order to validate performances of ^3He counters used by the LUNA collaboration. These measurements were mainly devoted to guarantee the neutron background suppression from Surface and Underground Laboratory and to evaluate the improvement of the alpha intrinsic background emitted by impurities in the material of the case (Uranium and Thorium mainly). These particles generate uniform background covering the area of the thermal neutron peak and extending up to 9 MeV.

This improvement should be guaranteed by the usage of cleaner materials in the case: in particular they have been constructed with a stainless steel case instead of the usual aluminium.

Regarding the surface measurement, only 12 hours of measurement have been necessary to get 3% statistics due to the neutron high flux on Earth Surface, measuring a thermal neutron background flux of $n_{surf} = (5.6 \pm 0.12)10^{-4}\text{n cm}^{-2}\text{s}^{-1}$ compatible with values in literature.

The 18 counters were installed in a surface LNGS laboratory, as shown in picture 2.5. The set up mounted will be described in Chapter 3.

In LNGS Underground Laboratory, measurements have been let run for a period of 20 days. Two energy regions of interest have been taken into account: between $191 < E < 764 \text{ keV}$ for the neutron background evaluation and $900 < E < 1100 \text{ keV}$ for the intrinsic alpha background.

The maximum level of intrinsic alpha background tolerated in a single counter was established of 300 counts/month in order to guarantee the low background condition of the setup.

Figure 2.6 shows the comparison between a spectrum acquired in the surface



FIGURE 2.5: Setup for the commissioning of the ${}^3\text{He}$ counters

laboratory (blue spectrum) and one acquired in LNGS underground laboratory (black spectrum); both spectra are normalized to time.

The neutron underground flux measured with this setup, $n_{UG} = (7.07 \pm 0.23)10^{-7}\text{n cm}^{-2}\text{s}^{-1}$, is consistent with previous measurements [45, 49], confirming the neutron flux reduction by three orders of magnitude with respect to surface laboratories stated in literature.

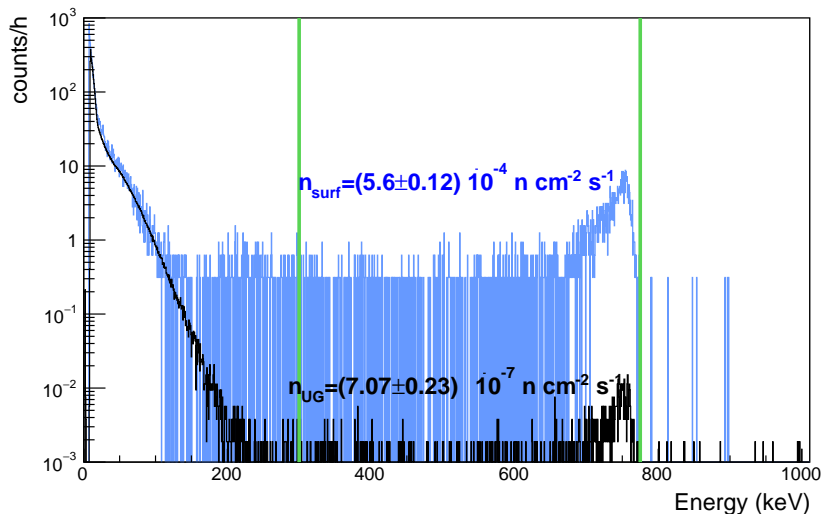


FIGURE 2.6: Comparison of neutron background measured in a surface lab (blue spectrum) and in the LNGS Underground (black spectrum). The flux was measured using 18 unshielded ${}^3\text{He}$ counters.

The analysis of α intrinsic background of the ${}^3\text{He}$ counters was estimated integrating the region between the two blue bars in Figure 2.7; results are summarized in Table 2.3.

As one can see, the number of counts/month is well below the set limit.

The average counting rate of alphas is (1.5 ± 0.04) counts/h and the average flux of alphas is $N_\alpha = (8.21 \pm 0.22)10^{-8} \alpha \text{ cm}^{-2}\text{s}^{-1}$.

In order to confirm the high level of purity of the stainless steel counters, I performed a measurements with two aluminium ${}^3\text{He}$ counters.

Figure 2.8 shows red and blue spectra acquired with counters case made of aluminum and stainless steel, respectively.

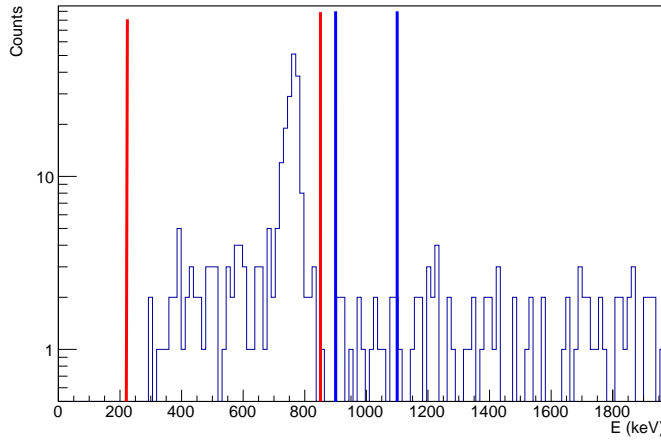


FIGURE 2.7: Particular of an ${}^3\text{He}$ background spectrum acquired in the underground lab of LNGS. The red bars and the blue ones indicates the neutron peak and the integration region for the alpha intrinsic background, respectively.

TABLE 2.3: Counts per month in the region of interest of neutron spectra between $900 < E < 1100$ keV. The maximum limit is 300 counts/months for the validation of each counter

channel	counts/months ($900 < E < 1100$ keV)
0	42
1	56
2	81
3	48
4	74
5	117
6	75
7	77
8	81
9	93
10	54
11	47
12	80
13	57
14	51
15	65
16	49
17	30

A normalization in their geometry dimensions has been applied.

In correspondence of the neutron peak at channel 700, corresponding to an energy $E=764$ keV, the counting rate of the two spectra is comparable, but between channels 800 and 1000, the stainless steel counters have a counting rate one order of magnitude lower. This is due to the reduction of alpha intrinsic background as consequence of a higher level of purity in the material used.

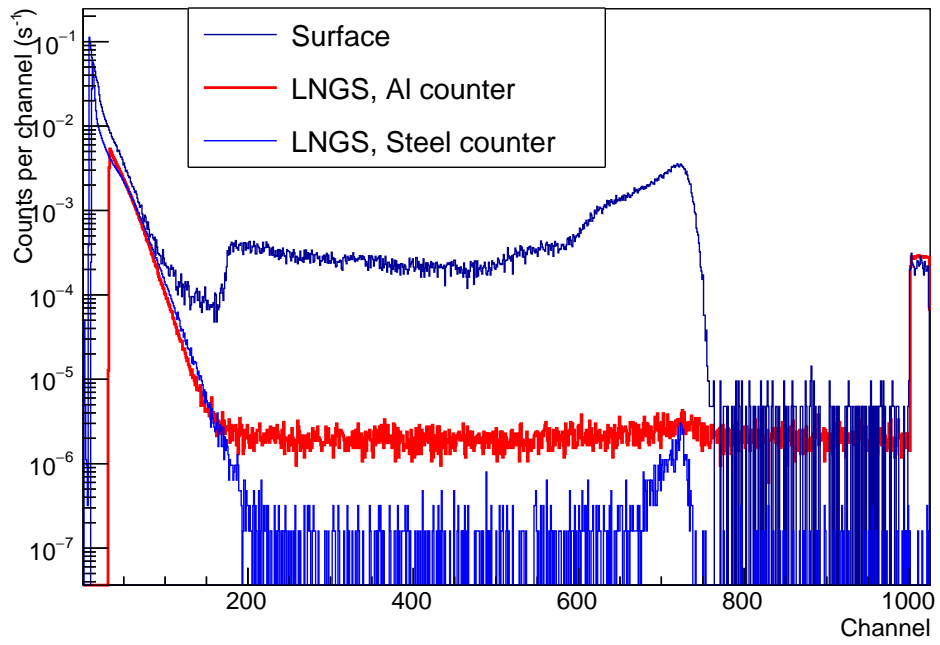


FIGURE 2.8: Comparison of LNGS neutron background measured with two different 3He counters. Blue spectrum refers to the stainless steel, while the red spectrum to aluminum.

2.3 A feasibility study for $^{13}\text{C}(\alpha, n)^{16}\text{O}$ reaction at LUNA 400

From the above discussion the need for precise cross section data inside the Gamow peak is evident. In this section I have approached a feasibility study of the reaction. The number of particles detected, N_d , after the emission from the target can be calculated starting from the thick target Yield formula 2.2:

$$N_d(E_\alpha, t) = \langle I \rangle t \eta \int_{E_\alpha - \Delta E}^{E_\alpha} \frac{\sigma(E)}{\epsilon(E)} dE \quad (2.2)$$

where $\sigma(E)$ is the reaction cross section, $\epsilon(E)$ is the stopping power of alpha particles in Carbon, $\langle I \rangle$ is the average beam current, t is the time of measurement, η is the detection efficiency, ΔE is the target thickness in keV and E_α is the beam energy.

The stopping power is extracted from the database SRIM2008 [50], the reference cross section curve is the extrapolation from Heil's paper [34].

Table 2.4 shows the expected number of reactions per day as a function of beam energy for typical conditions in low energy nuclear astrophysics: an alpha beam current of $100 \mu\text{A}$ and a target thickness of $10^{18} \text{ atoms cm}^{-2}$, with 30% of efficiency.

The particle detected based on formula 2.2 go at the level of few dozens per day with decreasing alpha energy.

In addition, another numerical simulation has been performed to highlight

TABLE 2.4: $^{13}\text{C}(\alpha, n)^{16}\text{O}$ reaction rate as a function of alpha energy.
Calculation are based on quantities specified in the text and on cross section by Heil.

$E_{\alpha,lab}(\text{keV})$	$E(\text{keV})$	Rate (d^{-1})
320	245	19
340	260	64
360	275	190
380	291	519
400	306	1322

as the environmental background reduction of a deep underground laboratory could improve the $^{13}\text{C}(\alpha, n)^{16}\text{O}$ cross section measurement at lower energies.

For the lowest energy point we have evaluated an upper limit using the Rucker condition [51], which applied his study to radioactive source starting from Currie's theory of Method Detection Limits (MDLs).

The minimum number of counts L_d that can be detected and distinguished at 95% of confidence level from background with a standard deviation σ_b , is given by the Formula

$$L_d = 2.71 + 4.65\sigma_b \quad (2.3)$$

Due to the low rate at lower beam energies, I assumed a time of measurement of 10 days. The number of events coming from background in a time t has been parametrized by the Formula

$$N_b = (N_n S(1 - rej) + N_\alpha A)t \quad (2.4)$$

where, N_n is neutron background flux that enters in a neutron shielding of overall surface S and a rejection power rej .

The rejection power rej is the ratio between neutron coming from outside detected divided by neutron entered in the detector, N_α is the intrinsic alpha flux coming from impurities inside the ^3He counters cases and A is the overall surface of all the ^3He counters.

The setup was assumed composed by $n=18$ tubes with an active length of $L=50$ cm with $d=2.54$ cm diameter embedded in a PE shielding with the dimensions $44 \times 44 \times 64 \text{ cm}^3$, so $A = \pi L d n = 7180 \text{ cm}^2$ and $S = 15136 \text{ cm}^2$.

Combining formulas 2.2, 2.3 and 2.4 for a 10 days long measurement and neutron and alpha fluxes estimated above, the detection limit is $L_d = 115$ counts, corresponding to an upper limit at $E_{\alpha,lab}=310 \text{ keV}$ ($E=235 \text{ keV}$).

For a surface measurements, with the neutron background 3 orders of magnitude higher, the limit is set at $E_{\alpha,lab}=350 \text{ keV}$ ($E=267 \text{ keV}$).

Figure 2.9 summarizes the situation: red curve is the detection rate after 10 days of measurement. The blue and green lines indicate the detection limit due to the neutron underground and surface background, respectively. Due to the exponential behaviour of the cross section, a background reduction of 3 orders of magnitude, does not correspond to 3 orders of magnitude in the detection limit.

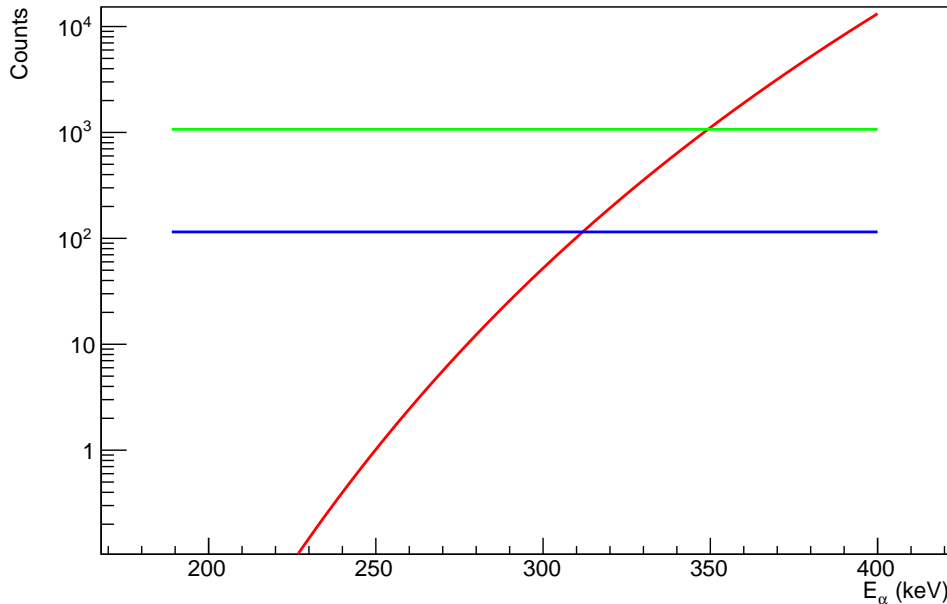


FIGURE 2.9: (Colour online) Detection limit according to Rucker's Formula: the green and the blue line indicate the Detection Limit L_d for a measurement in LNGS underground measurement and in a surface Laboratory, respectively

A further calculation has been performed to understand the contribution of the screening effect in our energy region of interest.

The electron screening potential U_e was evaluated with a phenomenological approach by Rolfs [52], assuming a reduction of the Coulomb potential due to the electron cloud around the nucleus. He approximated the turning point

of a projectile on a nucleus with Z electrons as $R_a = R_H/Z$, where R_H is the Bohr radius and Z is the charge of the nuclide, obtaining $U_e = \frac{Z_1 Z_2 e^2}{4\pi\epsilon_0 R_a} = 2.07$ keV.

This value should be compared with the one assumed in La Cognata et al. [4], where in adiabatic approximation they obtained a lower value: $U_e = 0.97$ keV. The enhancement factor f_{enh} to correct the cross section taking into account the screening effect can be calculated using the Formula 2.5:

$$f_{enh} = e^{\pi\eta \frac{U_e}{E_{cm}}} \quad (2.5)$$

where η is the Sommerfeld parameter and U_e is the screening potential.

From the comparison of the two curves in Figure 2.10, it comes out that the correction due to the screening effect in the energy range of the present work $E_{\alpha,lab}=360-400$ keV is always less than 10%.

Blue and red points have been calculated with the Rolfs model and with adiabatic limit, respectively.

This feasibility study confirms the advantage to perform the measurement

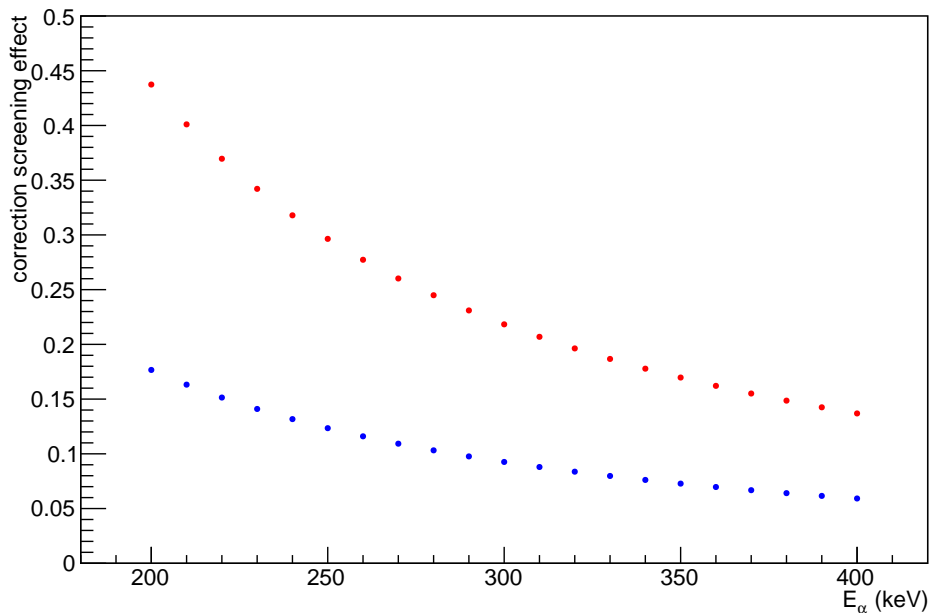


FIGURE 2.10: (Colour online) The corrective factor due to the electron screening effect calculated with and adiabatic approximation

in a deep underground Laboratory where neutron background is strongly suppressed.

With the benefits of the environmental background reduction we can aspire to measure cross section down to $E_{\alpha,lab}=360$ keV ($E= 270$ keV). The goal would be to reach an overall uncertainty of 10% for the high energy part ($360 < E_{\alpha,lab} < 400$ keV).

Moreover the correction to be applied to take into account the electron screening is at the level of 10%, with a non critical effect on systematic uncertainties.

Chapter 3

The setup characterization

In this chapter I will describe the main phases of the development of the Geant4 simulation code adopted for the maximization of the efficiency of the setup devoted to the study of the $^{13}\text{C}(\alpha, n)^{16}\text{O}$ reaction. The measurements of low rate events, implies the need to build a detector with the highest possible efficiency and a high environmental background rejection.

This of course taking in consideration the feasibility of the machining, the easiness to handle it and the necessity to change targets in an easy way.

Comparing the two main methods of neutron detection adopted nowadays, ^3He counters or scintillators, the method that guarantees the above listed features is the construction of a detector based on ^3He counters technology (Section 3.1).

Many variables can influence the efficiency: the number of counters, their disposition (e.g the distance from the target and the relative position respect to it), the quantity of moderator material to slow down the neutrons produced in the reaction, the reduction of the background coming from the external environment. A series of simulations based on the Monte Carlo code Geant4 (GEometry AND Tracking) [53] have been performed (Section 3.2).

Actually, two different setups (see section 3.3) have been developed with two different aims. The first one is so called Multi Target (MT) setup, where three targets can be mounted in the same chamber; it has been used for the ^{13}C targets characterisation, since during this procedure the reproducibility of the measurement is crucial in order to characterize targets. The other setup, the so called Single Target (ST) Setup has an higher efficiency and it was designed in order to go lower in energy and approach the Gamow Window collecting as much statistics as possible: in this case only one target can be mounted in order to increase the amount of moderator that eases to slow down neutrons. In the last part of the chapter 3.4 simulation efficiencies are compared with experimental efficiency measured at MTA ATOMKI by beam the $^{51}\text{V}(p, n)^{51}\text{Cr}$ reaction and with an AmBe source at LNGS.

3.1 Neutron detectors

Nowadays there are two most developed neutron detection techniques: either slow neutron detection via gas proportional counters, mainly He3 filled counters, or fast detection techniques using scintillators [54].

The two approaches are extremely different and here I will describes potentiality of both of them. ^3He counters exploit the fact that cross section of $^3\text{He}(n, p)^3\text{H}$ ($Q= 764$ keV) neutron capture reaction is 5330 barn at thermal

energies and is proportional to $1/\sqrt{E_n}$, where E_n is the neutron energy. The charged particles produced, a proton and a tritium, ionize the gas inside the detector and generate electrons that are drifted toward the anode by an electric field. The charge collected generates a signal proportional to the energy released from the reaction that is at maximum the Q value of the reaction.

Thanks to this, the intrinsic efficiency of this kind of detector is larger than 90% for thermal neutrons, but becomes lower and lower with increasing neutron energy.

For neutrons of few MeV it is mandatory to surround 3He counters with thermalizing light materials, like water, paraffine or polyethylene that contains Hydrogen.

The main consequence is the loss of the detected neutron energy information: this could be a problem for the discrimination of neutrons coming from sources different than the reaction under study, e.g. environmental or beam induced background.

Environmental background is mostly due to spontaneous fission of ^{238}U in the cavity walls and (α, n) reactions induced by α -particles from the natural radioactivity.

Beam induced background comes from light element impurities that, due to the low Coulomb barrier, can easily open (α, n) reactions: I will give further details on beam induced background sources in Chapter 4.

The 3He counters sensitivity to gamma rays is negligible, so γ -ray background is not an issue. A problematic source of background can be due to the alpha particles emitted from the radioactive impurities (e.g. Uranium and Thorium) in the detector case: these release energy inside the gas and generate an uniform background from the neutron peak region (191-764 keV) up to 10 MeV.

A selection of case material can help to reduce impurities.

Moreover Pulse Shape Discrimination (PSD) techniques to distinguish neutron signals from alpha signals have been developed to overcome this problem [55, 56].

On the other hand, scintillators take advantage from the neutron elastic scattering on light nuclei (e.g Hydrogen, Carbon): in this case there is no necessity to thermalize neutrons and it is possible to maintain the neutron energy information to select neutrons coming from the $^{13}C(\alpha, n)^{16}O$ reaction.

The intrinsic efficiency of a scintillator is much lower than a 3He counter [57] and it is difficult to guarantee a low level of impurities inside the scintillator. Even if scintillators are sensitive to gammas (Compton interaction with light elements), that generate an important source of background inside the detector, PSD procedures [58] are well known and largely used to select neutrons signals and reject gamma ones: however the result is dependent on the threshold used.

After all these considerations and some tests on both technologies, the LUNA collaboration decided to invest on the 3He counters.

Higher intrinsic efficiency and lower intrinsic background, due to the usage of stainless steel case instead of the usual aluminum, are ideal conditions for low event rate measurements.

^3He counters taken in consideration are provided by *GE oil & gas Digital solutions* with the specification shown in Table 3.1

TABLE 3.1: Main specification of ^3He counters by GE

Case material	Stainless Steel
Diameter	2.54 cm
Active length	40 or 25 cm
Gas pressure	10 atm

This was the starting point for the setup design.

3.2 Detector design

In my PhD work, an extensive effort was devoted to the development of a robust Monte Carlo simulation based on the Geant4 platform.

Several major considerations are necessary in order to optimize the design of the neutron detector.

First of all, here I will illustrate the three main user classes necessary as input in the code and the assumption to model the detector:

- the **Primary Particles generator**: here the main features of the simulated source are specified (type of particle emitted, energy and momentum). A pointlike source in the center of the polyethylene shielding is considered. A generation of 10000 neutrons per run emitted isotropically in the center of mass system with an energy according to the kinematics of the reaction is performed.
Due to the Q value of the $^{13}\text{C}(\alpha, n)^{16}\text{O}$ reaction (2.216 MeV) and the alpha energy range between 50 and 400 keV, the average neutron energy produced by the reaction is 2.5 MeV
- the **Physics List**, that includes all the libraries for the particle interactions and possible decays: in particular NeutronHP library [59] has been implemented in order to have the best cross sections for the reproductions of neutron transportation up to 20 MeV
- the **Detector Geometry**: this class includes the physical layout of the experiment, including detectors, absorbers etc: the counters will be embedded in a polyethylene ($(\text{C}_2\text{H}_4)_n$) matrix for the thermalization of the emitted neutrons

3.2.1 1 ring configuration

In this section, I will illustrate the main steps done in order to finalise the detector design, in terms of number of counters to use and their arrangement inside the polyethylene matrix.

Further details on the simulation regarding the polyethylene size are in Sub-section 3.2.3.

The easiest configuration is the arrangement of the counters in a circular array with the target in the center. An example is shown in Figure 3.1. The central hole that simulates the target chamber has been assumed with a minimum radius of 3 cm.

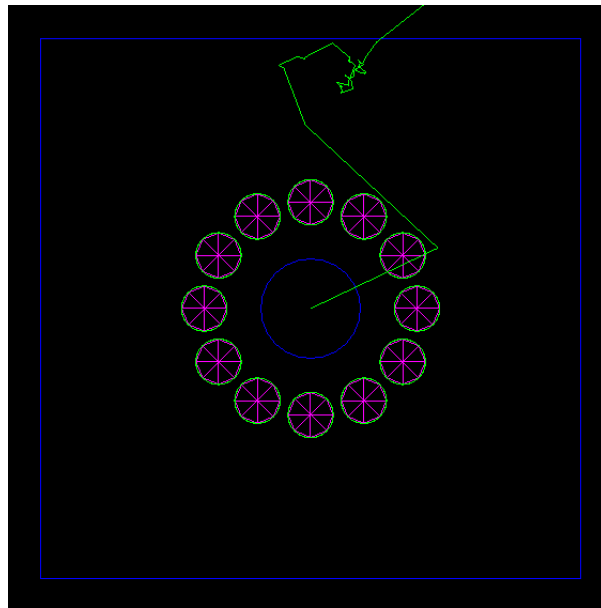


FIGURE 3.1: Example of an arrangement of 12 counters with an active length of 40 cm in one ring. Detectors are embedded in the polyethylene block. The central hole mimics the target chamber.

The major constrain is due to the limited number of counters allocated to maintain a reasonable distance between them and the target: the greater is the number of counters in the ring, the longer should be the diameter of the ring itself.

The setup efficiency curve is simulated with 12, 16 and 18 counters with active length of 40 cm arranged in a single ring as a function of its radius assuming a monoenergetic source emitting 2.5 MeV neutrons at the center of the setup.

Results are shown in Figure 3.2, where blue dot-dashed line, red line and dashed green line indicate setup efficiency with 12, 16 and 18 counters, respectively. For the three cases the overall setup efficiency is maximized when counter are 8 cm far from the target. It is around 32% without any improvement with the increase of counters' number and it decreases fastly with increasing distance from the target: at 12 cm it is reduced by 30% relatively to the maximum found.

So the placement of all the counters in one ring it is not efficient because does not enhance the usage of a higher number of counters.

3.2.2 2 rings configuration

Another possibility consists in placing counters in multiple concentric rings respect with the target.

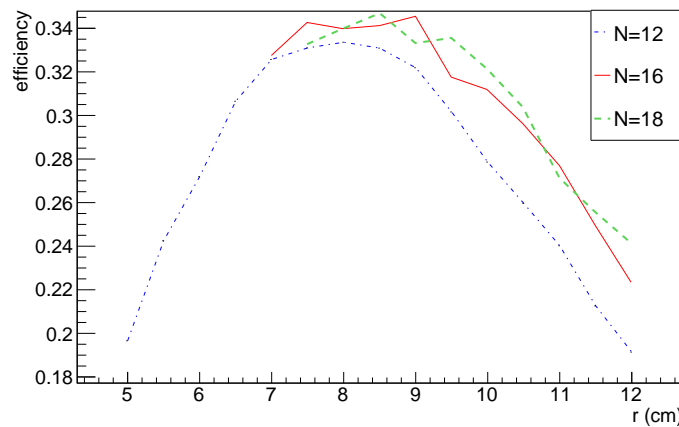


FIGURE 3.2: (Colours online) Overall setup efficiency as a function of the distance of the counters from the target. The simulation was carried out with 12, 16 and 18 counters (dot dashed blue, continuous red, dashed green lines, respectively). Increasing the number of counters the minimum distance necessary to allocate all the counters becomes larger

An example of the disposition is shown in Figure 3.3.

An advantage of this configuration is that the trend of the overall setup efficiency as a function of neutron energy is flatter in a wider energy range, as shown in many works in literature [60, 61].

I will use the notation N_i , r_i and L_i to refer to number of counters, the radius and the active length of the counters in the i -th ring, respectively.

For this geometry, the first step is to define the length and the number of counters.

Fixing $N_{1,2}$ and $r_{1,2}$, the efficiency as a function of the neutron energy for

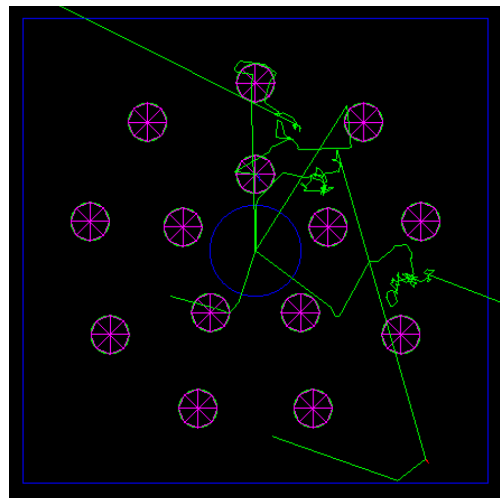


FIGURE 3.3: Example of arrangement of He3 counters in two concentric rings: in this case $N_1 = 5, N_2 = 9$

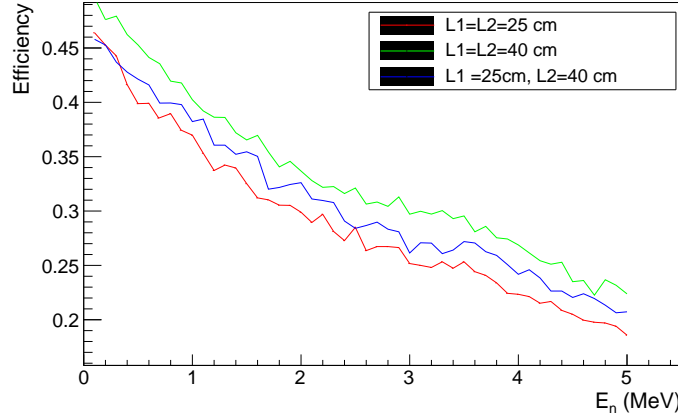
three different length configurations was evaluated:

L.1 all the counters with active length 25 cm

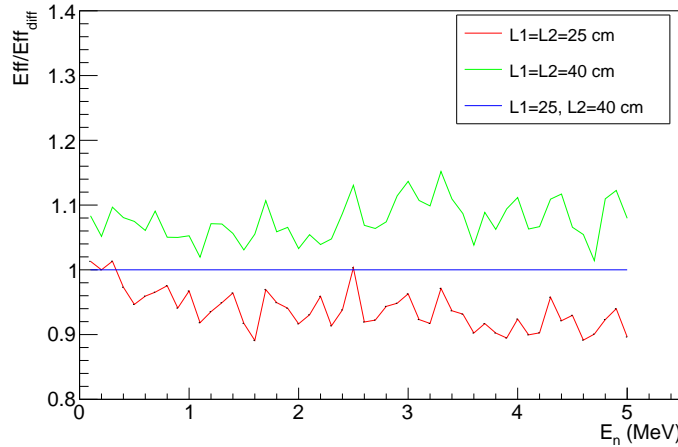
L.2 all the counters with active length 40 cm

L.3 the inner counters with an active length of 25 cm and the outer ones with a 40 cm: in this way, being r_1 smaller, the solid angle covered by the two rings is in any case comparable

The plot in Figure 3.4A shows the simulated efficiency curve as a function of neutron energy for the three cases listed above under these hypotheses: the number of counter in the rings are $N_1 = 5, N_2 = 9$ placed at distance $r_1 = 5$ cm and $r_2 = 15$ cm from the target, respectively.



(A) (Colour online) Efficiency as a function of neutron energy for different lengths configurations



(B) (Colour online) Efficiency normalized with respect to configuration L.3

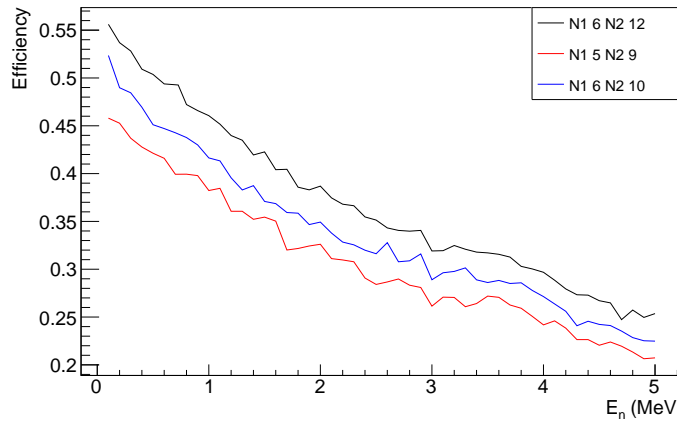
FIGURE 3.4

In Figure 3.4B efficiencies are normalized to the case L.3: the usage of different counters lengths in the rings has the consequence to lose the 10% relative efficiency respect to the configuration where all the counters are 40 cm long. The second step was to define the total number of He3 counters. Starting from $N_1 = 5$ and $N_2 = 9$, the number of counters was increased in steps of two.

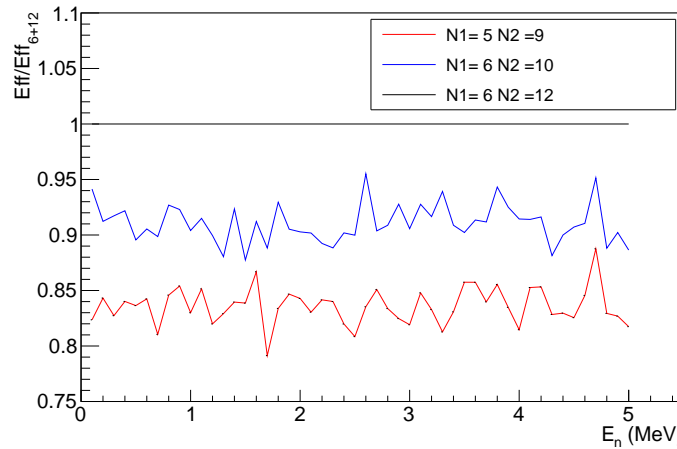
Figure 3.5A shows a comparison of efficiency curves for different simulations with an increasing number of counters.

Unlike the single ring configuration described in Section 3.2.1, adding two counters increases the efficiency of a relative 10%: this is evident in Figure 3.5B, where all the curves are normalized to the case of $N_1 = 6$ and $N_2 = 12$ counters.

Finally we concluded that 18 counters represent the best compromise between the mechanical limitations in design and construction (e.g setup dimensions, and its maneuverability, easiness in machining components, possibility to handle a large number of channels) and the available budget provided by INFN.



(A) (Colour online) Efficiency as a function of neutron energy for different number of counters configurations



(B) Efficiency normalized respect to configuration $N_1 = 6, N_2 = 12$

FIGURE 3.5

In the next step I performed simulations where r_1 and r_2 have been changed in order to tune efficiency as a function of counter layout inside the polyethylene matrix.

Figure 3.6 shows the efficiency of the 3He detector array as a function of r_1 and r_2 , let to vary from 5 up to 15 cm. The white bins are cases where the detectors overlapped or where $r_1 > r_2$.

The highest setup efficiency occurs when the counters rings are 6 cm and 11 cm, respectively; in this configuration the efficiency value is around 40%.

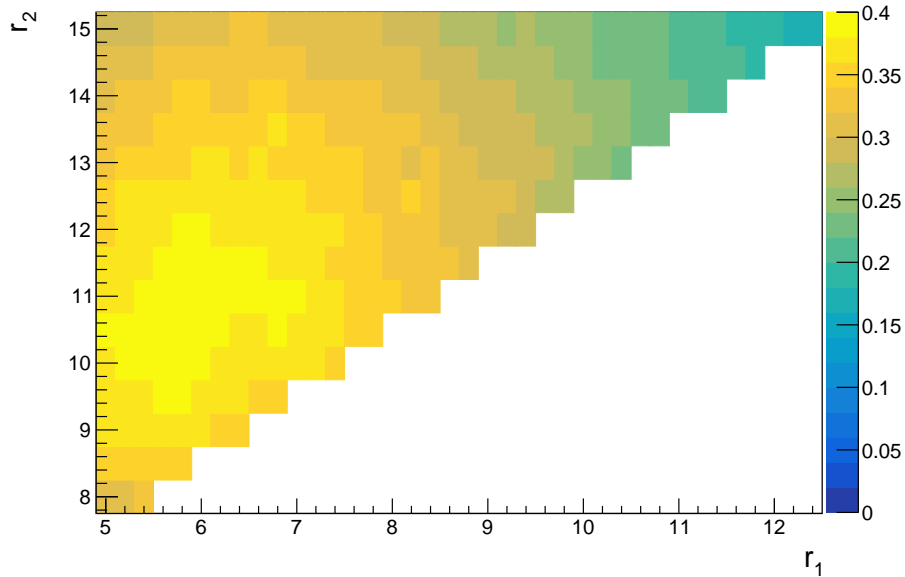


FIGURE 3.6: (Colour online) The efficiency of ^3He detector array as a function of r_1 and r_2 , simulated with an isotropic source emitting 2.5 MeV neutrons. The values have been obtained keeping the number of counters in each ring at $N_1 = 6$, $N_2 = 12$, with active lengths $L_1 = 25$ cm, $L_2 = 40$ cm, respectively. The internal radius is 30 mm.

The distance from the target has a crucial effect on the efficiency: going further from this position, the efficiency decreases: for example increasing both radii lengths of 1 cm, it becomes 10% relative lower.

Another important parameter is the size of the internal hole for the target chamber: a larger hole, has two main consequences:

- less moderator material between the target and the counters
- more distance between the beam spot and the detectors

For this reason I tried to quantify the effect of increasing the inner hole radius on the setup efficiency of 0.5 cm, for a total length of 3.5 cm radius.

I repeated the mapping of the efficiency as a function of the two radii, r_1 and r_2 , finding the arrangement that maximize the efficiency for the target target chamber.

Results are shown in Figure 3.7: the maximum was found for $r_1 = 6.5$ cm and $r_2 = 11$ cm.

The two conditions are summarized in Table 3.2 and in Figure 3.8A the comparison of the efficiencies curves for the two different target chambers is shown.

In particular, in Figure 3.8B, the efficiency is plotted as a function of neutron energy normalized to the configuration with 3cm of inner radius : an increase of 0.5 cm of the hole of the chamber reduces efficiency of 8% relative in the energy range that the LUNA accelerator can cover, between 2 and

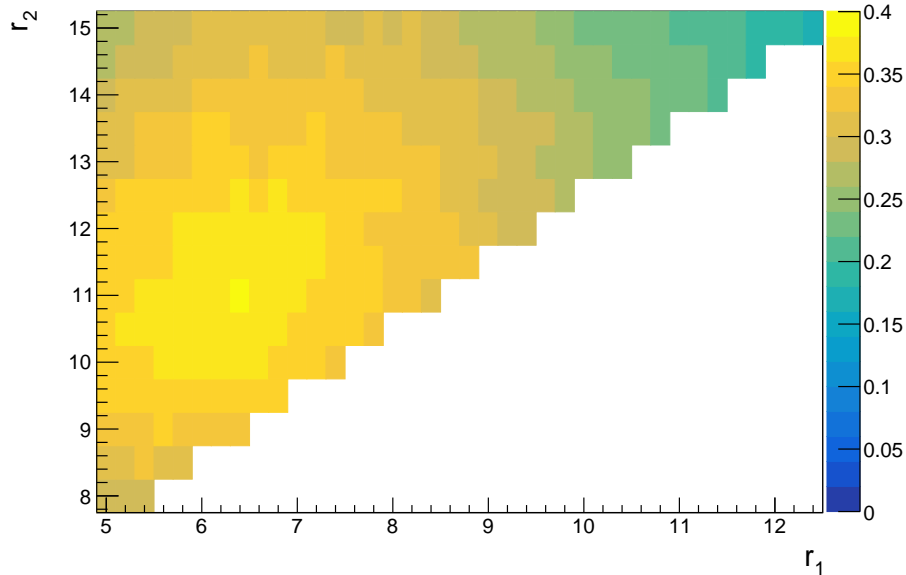
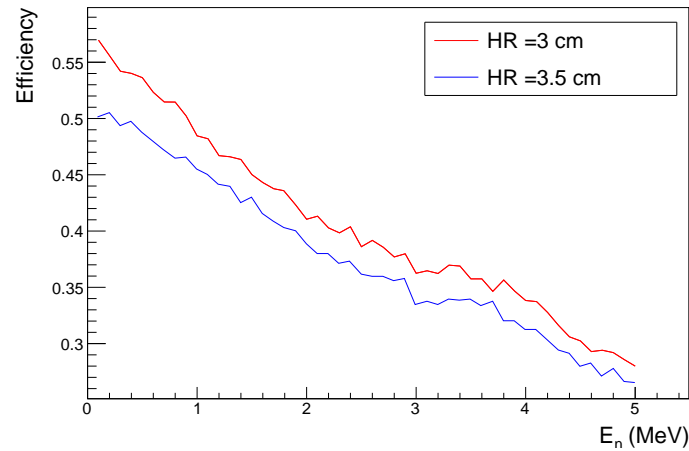


FIGURE 3.7: (Colour online) The efficiency of 3He detector array as a function of r_1 and r_2 , simulated with an isotropic source emitting 2.5 MeV neutrons. The values have been obtained keeping the number of counters in each ring at $N_1 = 6$, $N_2 = 12$, with active lengths $L_1 = 25$ cm, $L_2 = 40$ cm, respectively. HR is The internal radius is 35 mm.

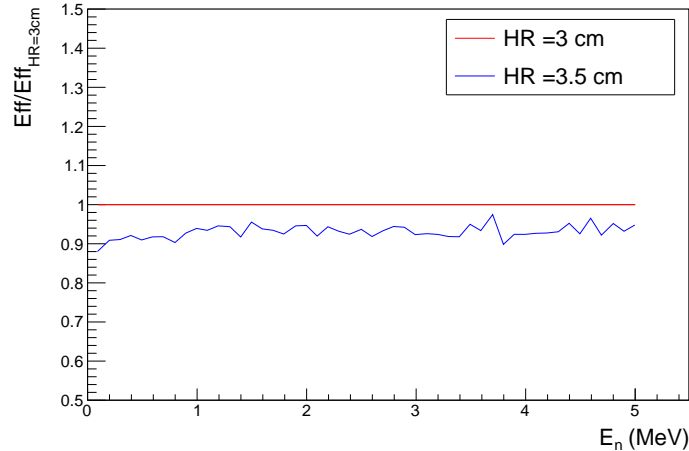
TABLE 3.2: Radii of the two rings that maximise the setup efficiency for two different target chambers target chamber Radii

HR (cm)	r_1 (cm)	r_2 (cm)
3	6	11
3.5	6.5	11

3 MeV. Concluding, the target chamber must be very compact in order to avoid reduction in the moderation material and consequently in the overall efficiency.



(A) (Colour online) Efficiency as a function of neutron energy for two setup with different target chamber radii.



(B) (Colour online) The efficiency curves normalized to configuration with target chamber radius 3 cm long.

FIGURE 3.8

3.2.3 The moderator design

The compactness of the setup is another parameter to consider: in this work I have investigated as the polyethylene matrix dimension could effect the detection efficiency, e.g if neutrons are reflected by larger amount polyethylene.

Figure 3.9 displays the simulated efficiency as a function of the polyethylene size varying in a wide range in x and y dimensions and fixing the z dimension, parallel to the counters orientation at 50 cm. The efficiency is constant within 2%.

So it is possible to conclude that the moderator dimension does not influence the overall setup efficiency and that it is possible to build a more compact setup easy to machine and handle: the final dimensions chosen are $40 \times 40 \times 50 \text{ cm}^3$.

The dimensions of the moderator has also impact on neutron coming from

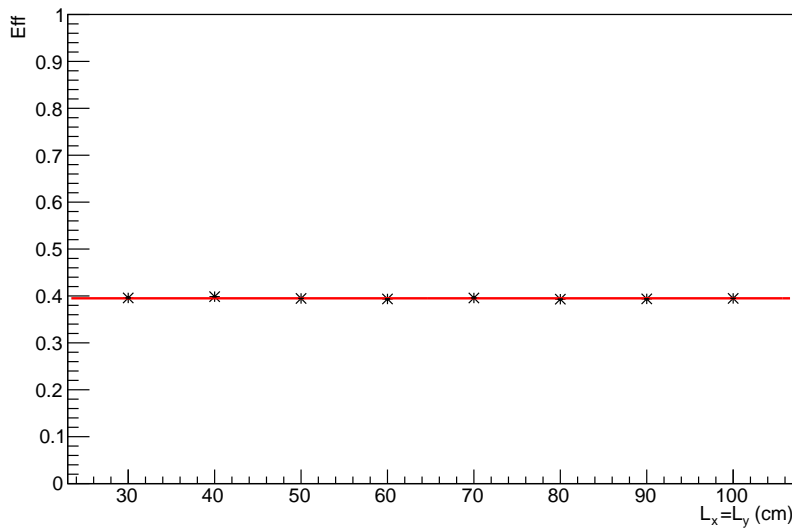


FIGURE 3.9: Efficiency as a function of polyethylene size.
The L_z , the dimension parallel to the counter direction, is fixed at 50 cm. Even with an increase of the L_x and L_y the efficiency fluctuates within relative 2%

the rocks.

In spite of the neutron background reduction by three orders of magnitude compared with the surface one, neutrons with a compatible rate with respect to the reaction rate expected for the LUNA measurement are emitted by (α, n) or fission reactions in the Laboratory rock.

During the years several measurements of LNGS neutron background have been performed [49, 46, 45]: due to a variation in the background depending on the location in the laboratory and due to unknown systematic uncertainties and statistical uncertainties at the level of 50%, it is very difficult to reconstruct a final LNGS neutron background energy spectrum.

An assumption that can be done is that slow neutron component ($E_n < 1$ MeV) is 1 order of magnitude higher than the fast one.

To take into account the slow neutron component of the LNGS background, I implemented in the Detector Geometry an external layer of neutron absorber, 5% doped Borated Polyethylene, to be mounted outside the polyethylene moderator.

In order to see the effect of this shielding, I simulated 10^7 monoenergetic neutrons emitted randomly on the surface of a sphere of a radius 2 meters long, with the direction emission towards the detector.

Figure 3.10 shows an example of event generated for this simulation.

The simulation was repeated for different neutron energies in order to cover all the possible neutron components of the spectrum.

The rejection factor $Rej(E_n)$ of the setup is defined as in Formula 3.1

$$Rej(E_n) = 1 - \frac{N_{det}}{N_{enter}} \quad (3.1)$$

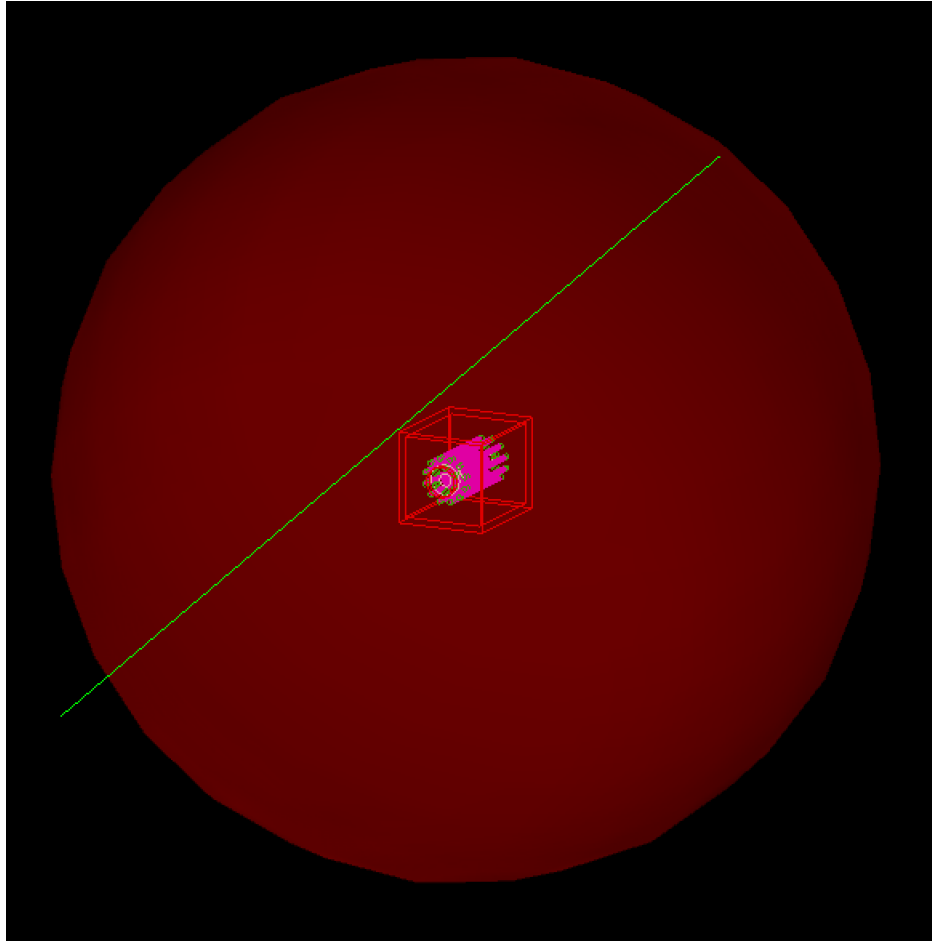


FIGURE 3.10: Geometry for the environmental background. Neutrons are generated on the surface of a 2 m radius sphere, in transparent red in Figure, with the direction toward the polyethylene.

where N_{det} is the number of neutrons detected and N_{enter} is the number of neutron generated that actually enter in the polyethylene shielding.

In table 3.3 the results of this investigation are summarized: the rejection factor at different neutron energies is evaluated.

Results of these simulations make me confident that the polyethylene shield-

TABLE 3.3: Rejection factor of the setup for different neutron energies

E (keV)	Rej(E)
2.5E-6	9.996E-01
1	9.971E-01
1000	9.792E-01

ing surrounded by a 2.54 cm Borated Polyethylene layer can be further reduced by a factor larger than 95%.

3.2.4 Study on systematic uncertainties in simulations

In this section I will summarise the test performed for the evaluation of possible systematic uncertainties due to the machining of the polyethylene and the fact that the source is not pointlike.

In order to take into account the dimension of the beam spot and evaluate possible systematic errors coming from the simulation, the Primary Particles generator was modified in two different ways:

- the beamspot is parametrized with a 2D gaussian centred exactly in the center of target, which is positioned at the center of the polyethylene block.
- the beamspot is parametrized with a 2D gaussian not centred respect the target, but is moved 0.5 cm up to the center: in this case the counters do not have the same distance from the neutron source.

The sigma of the gaussian is assumed 0.5 cm, taking in consideration that the LUNA400 accelerator beamspot is few cm diameter.

In Figure 3.11 the plot the efficiency normalized to the pointlike source is shown as a function of the neutron energy from 0.1 up to 3 MeV: the efficiency is constant within 1%, so it is possible to conclude that no systematic effect can be related to the extended beamspot.

Other possibile systematic uncertainties could come from a mis disposition

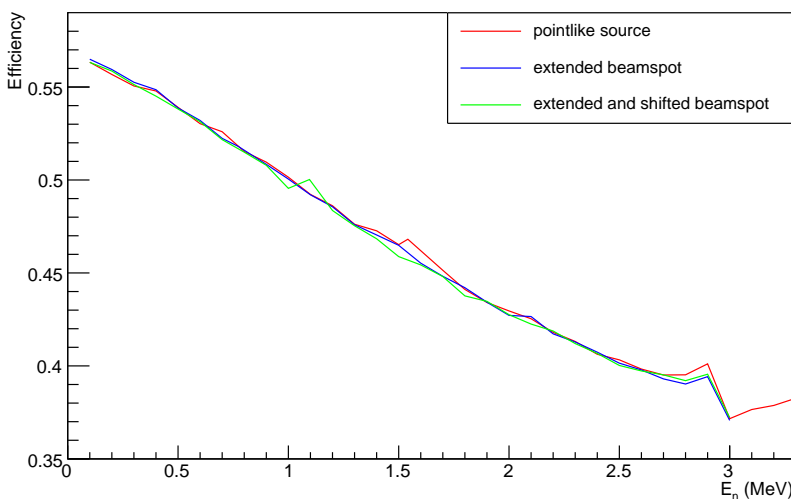


FIGURE 3.11: Efficiency as a function of neutron energy for the setup in case of a pointlike beamspot (red curve), a centered extended 2D gaussian beamspot (blue curve) and a not centered extended 2D gaussian beamspot. The efficiency is always the same within relative 1%

of counters inside the ring: this can be a consequence either of human mistakes in inserting counters in the polyethylene shielding or due to a wrong machining of holes. A misalignment of the counters along the beam axis was simulated with modification of the position of all the counters of 5 mm: in this case the target is not centered in the Polyethylene matrix. Another modification performed was the random variation of the counters in the x-y plane,

that simulates wrong positioning of holes.

The last simulation performed included an asymmetry in the machining of the shielding. All these simulation have been normalized to the efficiency curve calculated with a symmetric configuration. Results are shown in Figure 3.12: the violet curve, the light blue curve and the green curve are the efficiency curve of a mis disposition of counters along the z axis, in the x-y plane and with an asymmetric polyethylene shielding, respectively. For all different modifications in the counters arrangements, the efficiency curve does not change within 2.5% All these studies demonstrated that simulations

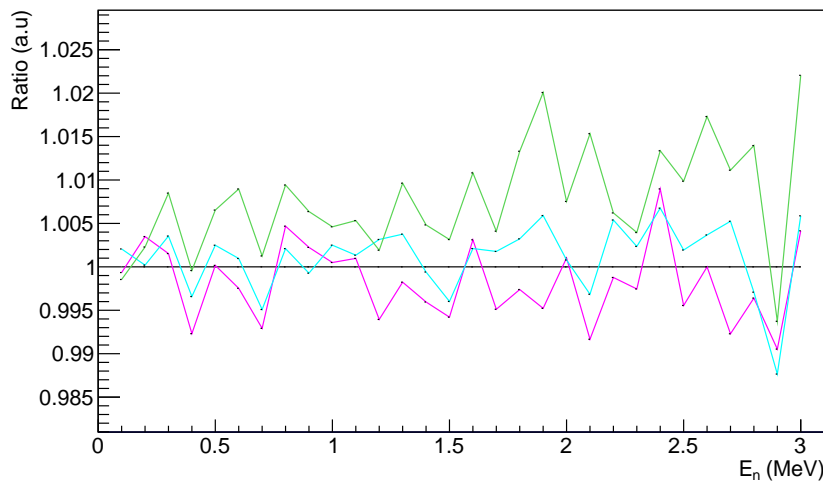


FIGURE 3.12: The study of systematic uncertainties due to mis disposition of ^3He counters in the polyethylene matrix: green, light blue and violet solid lines represents the efficiency curves with a mis disposition of counters along the z axis, in the x-y plane and with an asymmetric polyethylene shileding, respectively They are normalized to the correct position of counters (black lines)

performed are not affected by systematic uncertainties within 3%.

3.3 The experimental LUNA setups

The work performed and described in previous sections has been preparatory for the design of the experimental setup, from the point of view of neutron moderation and detection. Simulations are not a stand-alone method for the knowledge of absolute efficiency. We thought it is necessary to validate them by means of experimental measurements, and eventually scale the simulated efficiency curve. In next sections I will describe the setups (ST and MT) used for the measurement of the $^{13}\text{C}(\alpha, n)^{16}\text{O}$ cross section and the experimental measurements performed to evaluate the experimental efficiency.

3.3.1 The Single Target (ST) setup

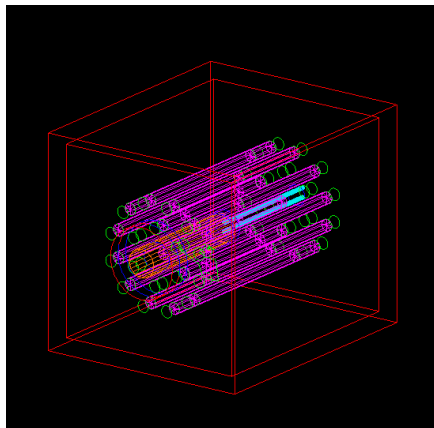
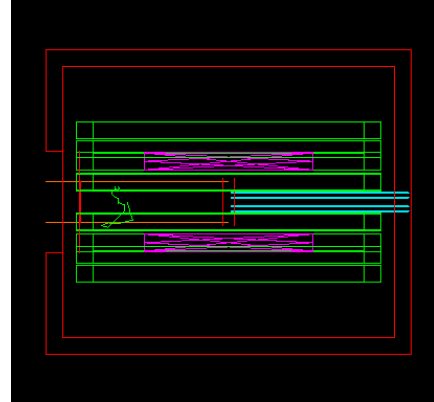
The high efficiency setup has the features summarised in Table 3.4.

The target chamber built was 5.5 cm diameter, so it was possible limitate the

TABLE 3.4: Features of the Single Target Chamber

number of rings	2
N1	6
N2	12
L1	25 cm
L2	40 cm
r1	6 cm
r2	11 cm
HR	3 cm
Polyethylene size without BPE	$40 \times 36 \times 50 \text{ cm}^3$
Borated Polyethylene Layer	2.54 cm

hole for the beamline in the central part at 3 cm radius.
The final setup is shown in Figure 3.16A

(A) ST setup, with the horizontal arrangement of the ${}^3\text{He}$ counters

(B) Section of the ST setup: the orange tube is the beamline chamber; the two light blue tubes are the inlet and outlet for the cooling

FIGURE 3.13

The efficiency as a function of neutron energy for this setup is displayed in Figure 3.14.

In this plot I also show the partial efficiency of the two radii separately: in

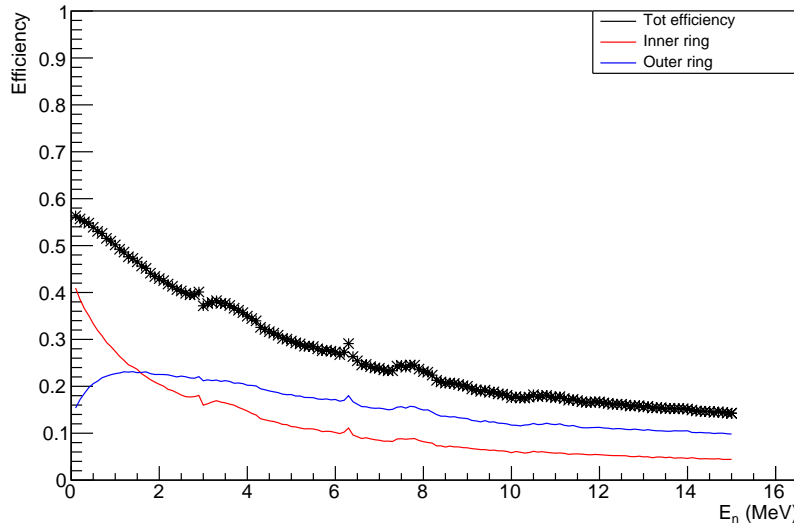


FIGURE 3.14: (Colour online) Single target setup efficiency as a function of neutron energy: black stars are the overall efficiency, the blue and the red lines are respectively the partial efficiency related to the outer and inner rings of the detector

the energy range of the LUNA measurement, the two rings contribute approximately in the same way, but the higher is the neutron energy, more the contribute of the outer radius is dominant with respect to the inner one.

The bumps in the efficiency are related with resonances in the $^{12}\text{C}(n, n)^{12}\text{C}$ reaction elastic cross section [62, 63]: the increase of probability of the first interaction with carbon (the most abundant material inside the moderator) eases the neutron slowdown and consequently increases the interaction with hydrogen(n-p elastic scattering reaction is exponential in the MeV energy region). In this way neutrons emitted are fastly thermalized and can be captured by ^3He counters with higher probability, increasing the detector efficiency.

3.3.2 The Multi Target (MT) setup

Even if the setup described previously is considered the optimal from the efficiency point of view, a second setup with a multiple target chamber was designed and realized.

This choice is related to the whole setup commissioning and to the target characterization phase where a beam spot reproducibility is crucial.

Moreover we had the possibility to mount simultaneously different typology of targets, (e.g. MgO target for beam focusing, Ta backing for beam induced background measurements).

We could change the target to be irradiated without breaking the vacuum in

the chamber thanks to a linear shift mechanisms.

The LUNA collaboration already had a target holder that could host three different targets (Figure 3.15): its dimensions are $4.2 \times 13.5 \times 1.74 \text{ cm}^3$. The so called Multi Target (MT) chamber was designed around the existing piece.



FIGURE 3.15: The MT holder, where three targets can be inserted in the chamber and can be changed without breaking the vacuum, preserving the measurement conditions

In order to maximise also in this case the moderation power of the setup, the most comfortable option was the arrangement of the counters in a vertical position, perpendicular to the beamline, as shown in Figure 3.16A. This needed two excavations inside the Polyethylene: the horizontal one for the beamline and the vertical one for the target chamber, with the radii HR and TcR, respectively.

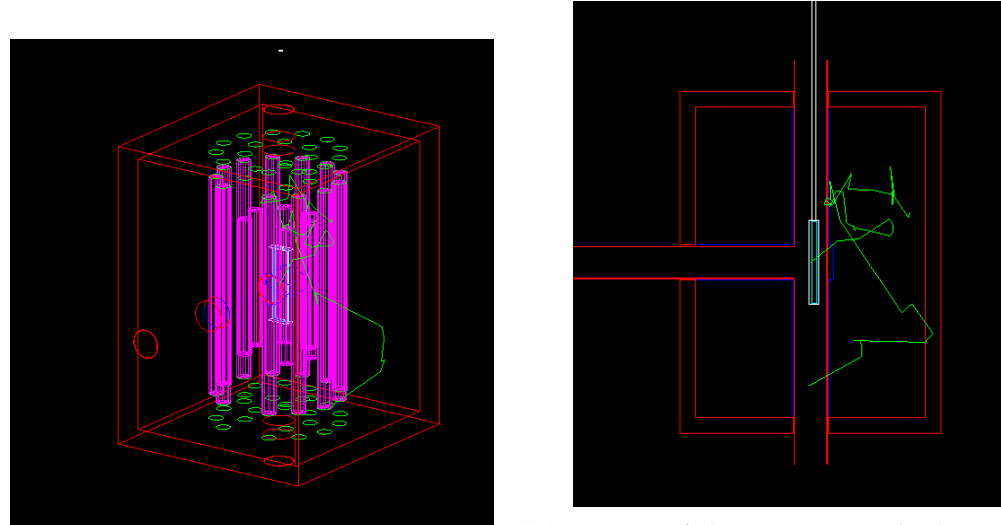
In Table the parameters of the design of the MT chamber are summarized. This configuration has the consequence that both the solid angle covered by

TABLE 3.5: Features of the Multi Target Chamber

number of rings	2
N1	6
N2	12
L1	25 cm
L2	40 cm
r1	6 cm
r2	11 cm
HR	2.8 cm
TcR	2.8 cm
Polyethylene size without BPE	$40 \times 50 \times 40 \text{ cm}^3$
Borated Polyethylene Layer	2.54 cm

the counters and the moderator material amount are reduced compared with the ST setup.

The efficiency as a function of neutron energy has been estimated and shown



(A) MT setup, with the vertical arrangement of the ${}^3\text{He}$ counters

(B) Section of the MT setup: the horizontal hole is for the beamline, the vertical one is of the target holder (upper part) and for the connection to an additional turbopump (downer)

FIGURE 3.16

in Figure 3.17. its trend is similar to the ST setup both for the overall efficiency, indicated by the black stars, and for the partial ones (red and blue lines indicates inner and outer ring, respectively). Bumps in the efficiency curve are evident also in this setup: due to the elastic scattering ${}^{12}\text{C}(n, n){}^{12}\text{C}$.

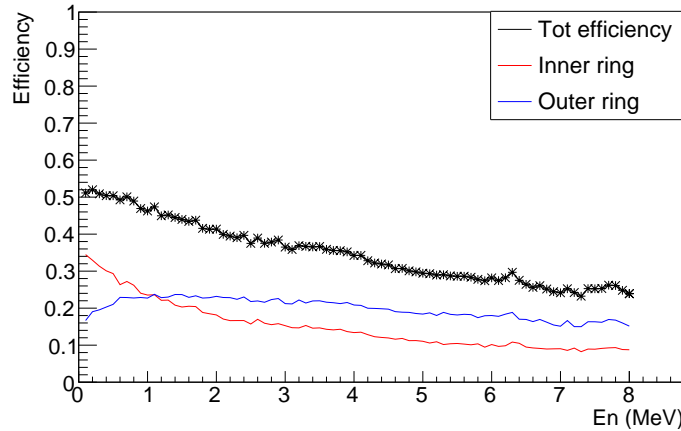
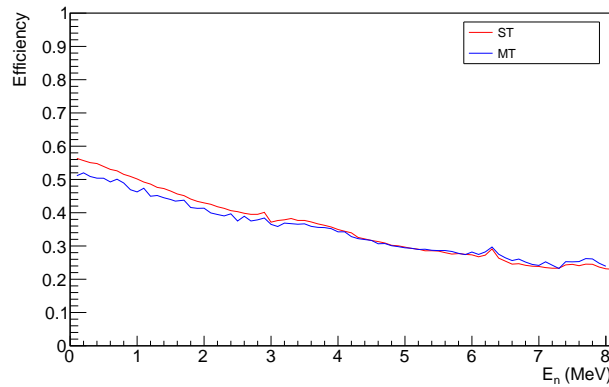
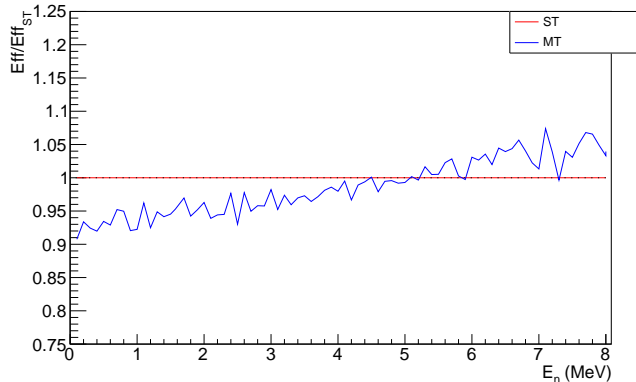


FIGURE 3.17: (Colour online) Efficiency as a function of neutron energy for the Multi Target chamber setup: black stars are the overall efficiency, the blue and the red lines are respectively the partial efficiency related to the outer and inner rings of the detector

The comparison of the efficiency as a function of the neutron energy is shown in Figure 3.18A: in particular, looking at Figure 3.18B it is possible compare the efficiency of the two setups normalized respect with the ST setup efficiency curve. In the neutron energy range covered LUNA400, with



(A) (Colour online) Comparison of the efficiency curves for the two setups as a function of the neutron energy : blue and red curves indicate the MT and the ST, respectively.



(B) Efficiency of the two setup normalized respect to the ST setup efficiency: in the neutron energy range covered by LUNA400 the efficiency of the ST is 10% higher in relative

FIGURE 3.18

$2 \text{ MeV} < E_n < 3 \text{ MeV}$, the efficiency of the ST setup is 10% relative higher than the MT setup. Increasing the neutron energy, the ratio has an inversion at $E_n = 5 \text{ MeV}$.

After this comparison the LUNA collaboration decided to split the campaign measurement in two parts using the two different setups.

In the first phase of the measurement, the MT chamber has been used in order to guarantee a high reproducibility of the beam irradiation on target and reduce systematics during the target characterization. During this phase the higher energy points, in the alpha energy range between 400 down to 360 keV, have been measured.

The second campaign will be devoted in going down in energy as near as

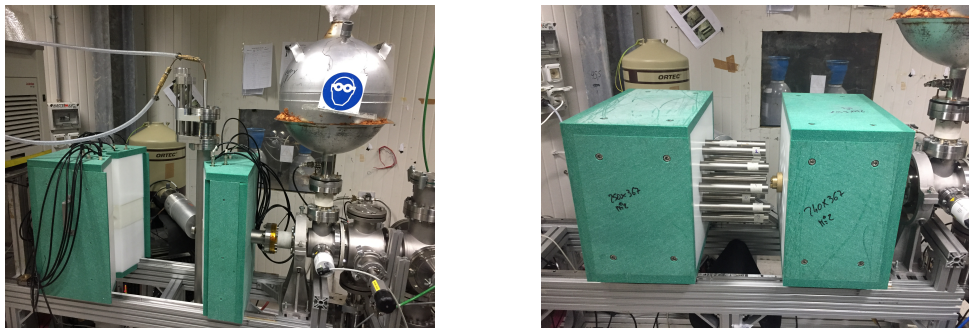
possible to the Gamow Window: because the cross section decrease exponentially with the decreasing of energy in the center of mass, an higher efficiency is mandatory. So during this phase the ST chamber will be mounted.

Some cross section points will be measured with both setups in order to have an overlap in the energy dependence between data tacking campaigns.

One important common feature of these experimental setups is the possibility to open the moderator in two parts moving one half along the beamline direction.

This requirement has been implemented in order to perform complementary measurement with an HPGe detector. As better illustrated in Chapter 4, the HPGe is mounted near the target in close geometry at 55° for the detection of prompt γ -rays emitted from the decay of the $^{13}\text{C}(p, \gamma)^{14}\text{N}$ reaction. The γ -ray spectrum acquired will be analysed to check the stability of the ^{13}C target.

In Figure 3.19A and 3.19B the picture of the mounted setups: the MT and the ST, respectively.



(A) Picture of the Multi Target setup, used for detector commissioning and the target characterization

(B) Picture of the high efficiency Single Target setup, used for the low energy cross section measurement

FIGURE 3.19

In Figure 3.20, a cartoon not in scale shows how the Multi Target setup works: for the $^{13}\text{C}(\alpha, n)^{16}\text{O}$ cross section measurement the moderator (green) is closed and the HPGe (red) is outside. For the target monitoring by means of the $^{13}\text{C}(p, \gamma)^{14}\text{N}$ reaction the moderator is opened and the HPGe is inserted in close geometry.

3.3.3 Environmental Background Measurement

The background inside the detector was measured to check the effectiveness of the Polyethylene shielding plus the external layer of Borated Polyethylene. This has two main components: the environmental neutron background of the rocks plus the alpha particles emitted by the He3 counters' walls.

During the measurement the moderator was let closed and the cooling system on: this to guarantee the same conditions that we had during the cross section measurements.

More than 10 days of measurement have been accumulated: the sum spectrum acquired was overlapped with the spectrum acquired with the AmBe

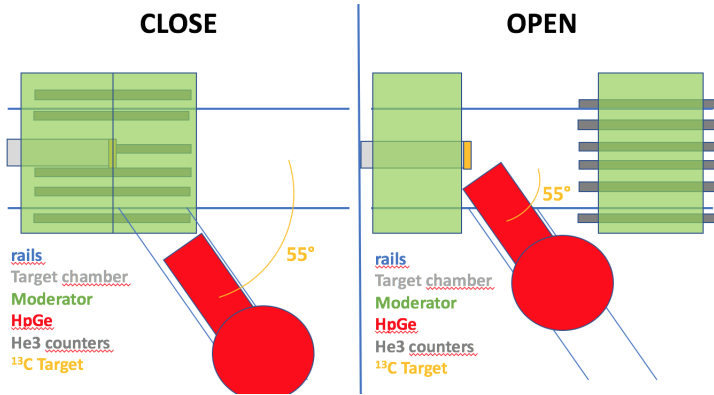


FIGURE 3.20: (Colour online) Cartoon of the ST setup (not in scale) from the top: when the moderator is closed, the $^{13}\text{C}(\alpha, n)^{16}\text{O}$ reaction cross section measurement is performed. For the target monitoring through the $^{13}\text{C}(p, \gamma)^{14}\text{N}$ reaction, the moderator was opened and the HpGe at 55° was moved in close geometry.

source, in order to identify the region of interest where the background contribute must be quantified.

Figure 3.21 shows the comparison of the environmental background spectrum and the AmBe one normalized by time. Without any beam source, we

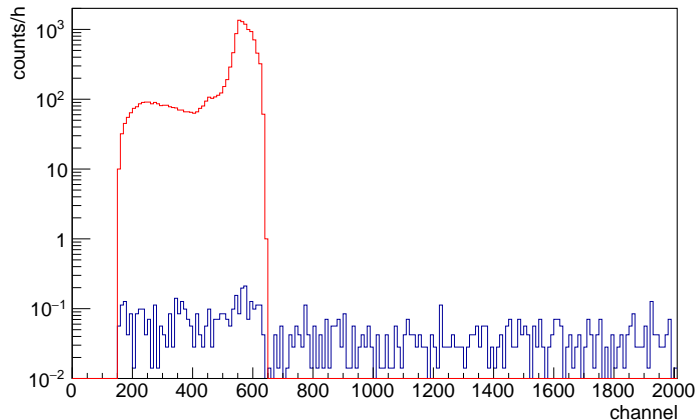


FIGURE 3.21: (Colour online) Comparison between environmental background and the AmBe spectrum.

counted 891 ± 30 counts in the region of interest corresponding to neutron peak.

This is equivalent to a background rate of 3.34 ± 0.11 events/h from the background.

3.4 Experimental efficiency measurements

To validate the efficiency from Geant4 simulations, an experimental efficiency campaign was scheduled. A neutron source was used; this makes difficult to build an absolute efficiency curve because the source is not monoenergetic but has a wide energy spectrum from slow neutrons up to few MeV.

For this reason the calibration campaign was divided in two parts: the first part has been performed at LNGS with an AmBe source and the second one at MTA ATOMKI using the $^{51}V(p,n)^{51}Cr$ reaction.

In this section I will describe in details the measurements performed and I will show some comparison between Geant4 simulations and real data.

3.4.1 The Data Acquisition System

In this section I will describe the Data Acquisition System used for the acquisition of the neutron spectra.

The High Voltage of the $^{18}^3He$ counters was provided by the Caen SY5527 Power Supply module. All the channels were supplied with a HV = +1200 V. This value has been chosen based on the declaration of GE that guaranteed that the gain is constant in the neighbourhood of this HV.

Signals from counters are shaped in the CAEN low noise and fast raise charge sensitive preamplifiers A1422 with a gain of 90 mV/MeV. Each module has 8 channels plus a common test input, for a total of 3 modules used (we used from channel 1 to channel 6 of each module).

Output signals from the preamplifiers were fed to 3 CAEN 8 Channel 14 bit 100 MS/s Digitizers V1724.

The usage of digitizers permitted to acquire and save waveforms for an offline analysis of signals.

The output of each preamplifier have been connected to input channels 1-6 of each module.

A V1718 controller module permitted the communication between VME modules and the PC where waveforms have been recorded and analysed offline. A software based on Labview [64] libraries has been developed on purpose. Figure 3.22 shows the Data Acquisition Chain for the saving of waveform from 3He counters.

3.4.2 Efficiency calibration with the AmBe neutron source

As first step, we performed an efficiency calibration in situ at LNGS with a neutron source.

It is possible to build a neutron source mixing an energetic alpha emitting isotope with a suitable target material. The maximum yield is obtained when beryllium is chosen as target: in this case neutrons are produced via the reaction $^9Be(\alpha, n)^{12}C$ ($Q = 5.71$ MeV). Among the alpha emitters, Actinide elements usually, two are the most common in this kind of source: Plutonium and Americium. The source used for the efficiency measurement at LNGS is an AmBe source with an emission activity of 10 n/s.

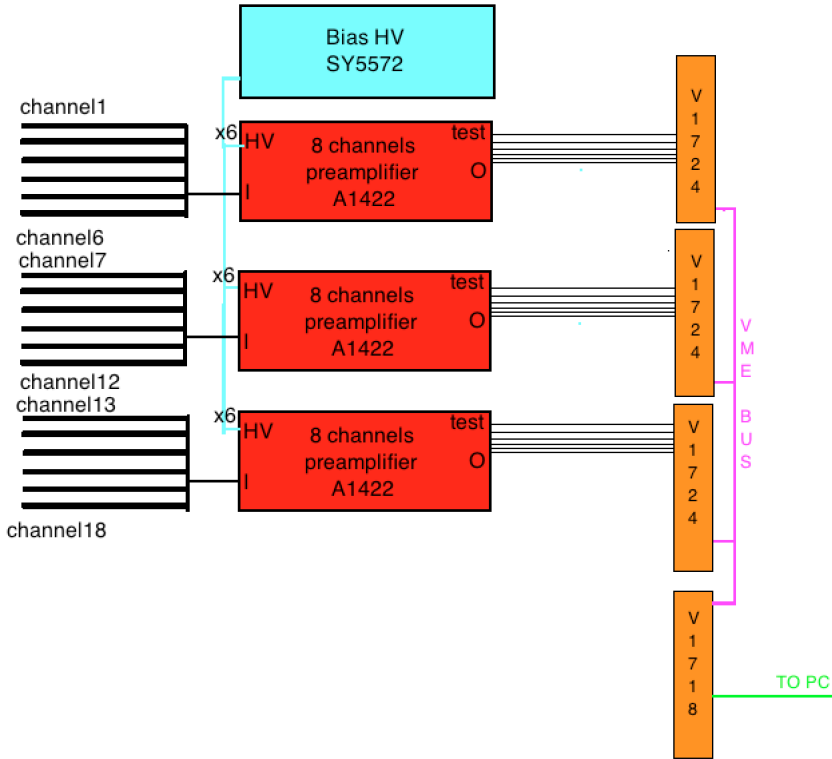


FIGURE 3.22: Scheme of the neutron detection electronics chain

We could not find any official certification that attested the activity calibration of the source, so we assumed uncertainties of 20% to be conservative. The spectrum of AmBe is shown in Figure 3.23 [65]: it has many peaks and valleys that are related to excitation states in which ^{12}C product nucleus is left. The advantage of this source is that the half life time is very long, 433 y, so the source emission rate modification is negligible.

The safety sheet is shown in Figure 3.24.

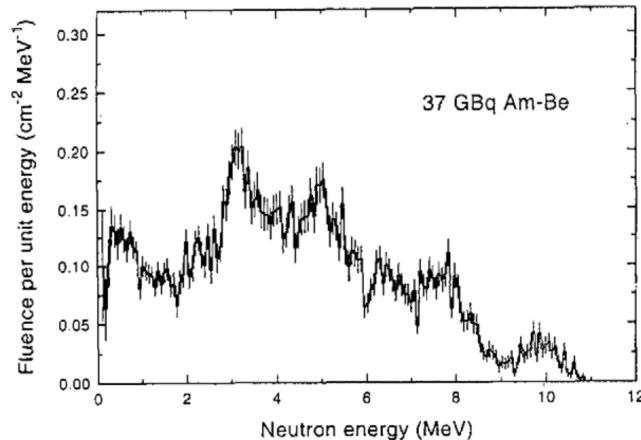


FIGURE 3.23: The Americium Berilium spectrum measured by Marsh [65] using an 3He sandwich spectrometer incorporating two semiconductor detectors and a proportional counter region

The measurement was performed for both the setups, the Single Target and

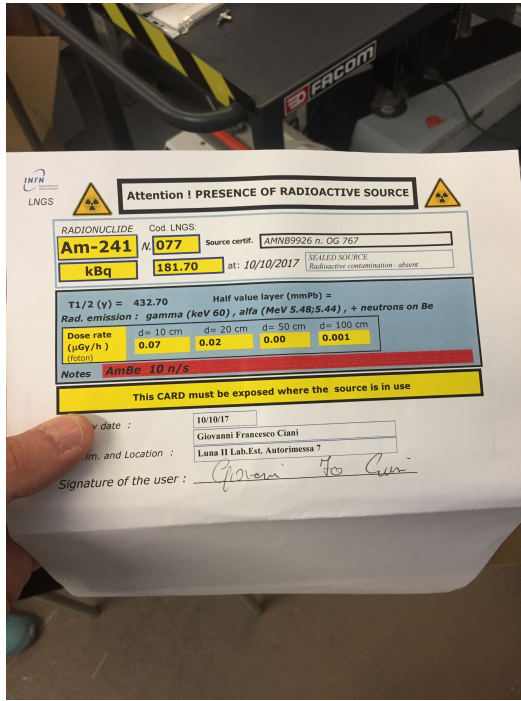


FIGURE 3.24: Safety Sheet of the 10 n/s AmBe source available at LNGS

the MultiTarget.

The source was mounted in the position of the target: in Figures 3.25A and 3.25B is shown the of the AmBe source mounted in Single target chamber and in the Multi Target chamber, respectively.

In order to guarantee the comparability with the $^{13}\text{C}(\alpha, n)^{16}\text{O}$ measurement, the water cooling system has been let on during the calibration measurements and vacuum inside the target chamber has been pumped.

The efficiency η can be estimated using the formula:



FIGURE 3.25: The source mounted in the two setup: in (A) and (B) are shown the ST target holder and the MT target holder, respectively

$$\eta = \frac{N_n}{AT} \quad (3.2)$$

where N_n is the number of detected neutrons in the all the channels, T is the of the acquisition time and A is the activity of the source.

In Table 3.6 the main quantity required for the efficiency calculation are summarized: overall acquisition time and neutrons detected in each detector ring.

TABLE 3.6: Time and neutrons detected in the two rings during the calibration measurements with the 10 n/s AmBe source for ST and MT setup. efficiency is calculated using Formula 3.2.

	time (s)	counts in the ROI (200-700 keV)		Efficiency calculated	
				partial	total
Single target setup	13544	Internal ring	21587	15.9%	36.1%
		External ring	27403	20.2%	
Multi Target setup	80744	Internal Ring	116192	14.39%	34.5%
		External ring	161001	19.54%	

The spectra from each counter have been summed and the sum spectrum was fitted in order to get the energy resolution of the setup.

The function used to parametrize the typical shape of a spectrum from a He3 counter is:

$$f(x) = \begin{cases} C * e^{-0.5(\frac{x-E_p}{\sigma})^2}, & \text{if } x > E_p. \\ C * \frac{(\frac{\Gamma}{2})^2}{(x-E_p)^2+(\frac{\Gamma}{4})^2} + c, & \text{if } x < E_p. \end{cases} \quad (3.3)$$

C is a normalization constant, E_p is the position of the neutron peak: at higher energies the peak can be fitted with a gaussian with the sigma of the resolution σ ; at lower energies the wall effect makes the decrease of the peak smoother, so the edge can be parametrized with a Lorentzian function centred in E_p with the scale parameter $\Gamma/2$ plus a constant c .

The fit of the total neutron spectrum is shown in Figure 3.26 and value of the parameter from the Fit are listed in Table 3.7

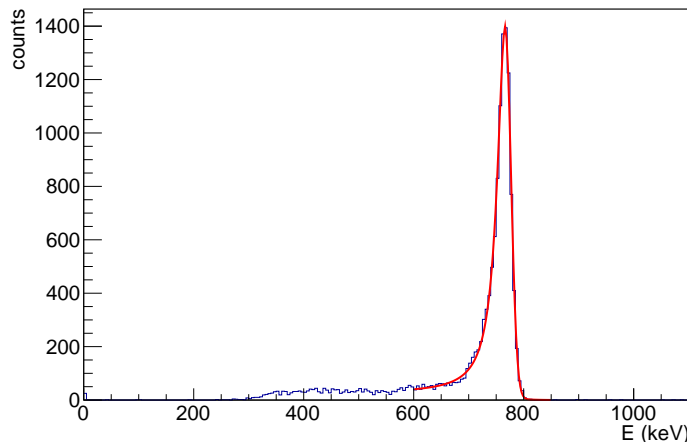


FIGURE 3.26: Example of spectrum acquired with the AmBe source mounted inside the LUNA detector. The peak is fitted with the Function 3.3 (red line)

The Full Width Half Maximum of the neutron peak can be extracted from

TABLE 3.7: Results from the fit of the sum spectrum of the Ambe source acquired with the Single Target Setup

par	value	error
C	1.37e+03	2.05e+01
E_p	7.66e+02	3.59e-01
σ	1.04e+01	2.42e-01
Γ	3.52e+01	9.03e-01
c	1.82e+01	3.01e+00

the parameters fitted as

$$FWHM = \frac{\Gamma + 2.355 * \sigma}{2} = (29.8 \pm 0.98)keV. \quad (3.4)$$

that corresponds to an energy resolution of 3.9% at the 764 keV.

This value was used in a Geant4 simulation, where the Ambe spectrum was

implemented inside the Primary Particle Generator. Figure 3.27 shows the simulated AmBe spectrum in blue, compared with the red points from the Geant4 forum (<http://hypernews.slac.stanford.edu>.).

100000 neutron have been generated and the results of the simulation are

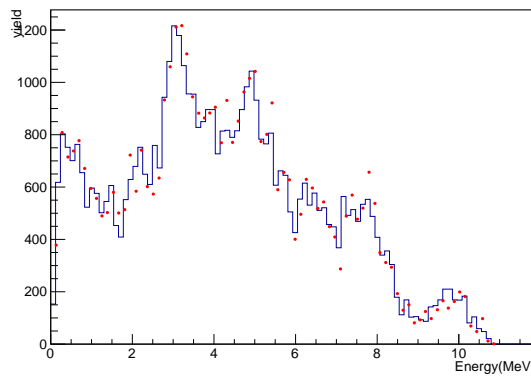


FIGURE 3.27: AmBe simulated spectrum implemented in the primary generator Geant4 code: red dots are the reference value from /hypernews.slac.stanford.edu

summarized in Table 3.8

TABLE 3.8: Geant4 simulations results with the AmBe source simulated

	Neutron generated	neutron detected		efficiency
Single target setup	100000	Internal ring	16151	16.15%
		External ring	19033	19.03%
Multi Target setup	100000	Internal Ring	15244	15.24%
		External ring	19630	19.63%

The comparison between the efficiency measured in Table 3.6 and the simulated one in Table 3.8 is in agreement for both the setups, both for the overall efficiency and for the single radii as well. This is already a strong argument on the reliability of values of efficiency obtained from the simulation.

In order to make more robust the efficiency validation, the collaboration decided to face a calibration campaign at MTA Atomki (Debrecen, Hungary), where we could generate a reaction that emitted neutrons at a energy well known from the reaction kinematics.

3.4.3 Calibration with the $^{51}V(p,n)^{51}Cr$ reaction

In order to strengthen the evaluation of the neutron detection efficiency of the LUNA neutron array in both moderator arrangements (vertical and horizontal), the collaboration performed measurements of non-resonant $^{51}V(p,n)^{51}Cr$ reaction ($Q=-1534.794$ keV).

This reaction is widely used in literature for the calibration of neutron detector setups [66, 34, 67] and guarantees an high stability of the ^{51}V target that allows to maintain low the systematic uncertainties.

Being a threshold reaction ($E_{th} = 1565$ keV), the measurement was performed at the 30° beamline by the 5MV Van de Graaff accelerator of MTA Atomki, (Debrecen, Hungary). The energy analysing device of the accelerator consists of a 90-degree homogeneous field analyzing magnet with adjustable energy defining slits at the object and image positions.

The magnetic field of the magnet is measured by a nuclear magnetic resonance (NMR) fluxmeter.

The beam goes through series of tantalum collimators hitting targets with a 5mm diameter beamspot.

The accumulated beam charge on target was measured with an ORTEC 439 Digital Current Integrator connected to the target chamber used as Faraday Cup.

In order to compensate the effect of secondary emitted electrons from the target, a -300 V potential was applied on the last tantalum collimator as electrons suppressor.

The DAQ system used was the same described in Section 3.4.1, with two differences.

Due to the high $^{51}\text{V}(p, n)^{51}\text{Cr}$ reaction and the consequent neutron rate production, a pulser signal was supplied to each DAQ channel through the test input of each preamplifier and at the same time in an empty digitizer channel. The ratio between pulser counts in each He3 channel and those in the empty channel allowed to estimate the dead time and correct spectra.

Moreover the software *MC2 Analyzer* by CAEN was used for the acquisition and spectra are saved without saving waveforms.

The measurement was performed at $E_p = 1700, 2000, 2300$ keV, that corresponds to average neutron energies of $E_n = 148, 454$ and 757 keV, respectively. Due to the presence of a second neutron channel above $E_p = 2335$ keV, corresponding to a ^{51}Cr level at about $E_x = 750$ keV, it is not possible to go higher in energy, since, above this energy, two groups of neutron energies are mixed and the reaction cannot be considered monoenergetic anymore.

The measurement is based on the activation technique: the $^{51}\text{V}(p, n)^{51}\text{Cr}$ reaction emits neutrons ad produces an equivalent number of ^{51}Cr nuclei, radioactive nuclides.

These decay with an electron capture process with a half-life of $T_{1/2} = 27.7025(24)$ day to an excited state of ^{51}V nuclide. So the emission of γ -ray lines follows: in particular we focused the attention on the 320 keV line with a 9.91(1)% branching ratio.

The irradiated targets were then moved in the low-level laboratory of MTA Atomki and the γ -rays emitted by the ^{51}V decay were detected using a lead-shielded setup with a 150% HPGe detector, shown in Figure 3.28.

The efficiency of the HPGe detector is $13.4 \pm 0.4\%$ at $E_\gamma = 320$ keV (private communication).

A typical HPGe spectrum acquired is shown in Figure 3.29: the red line in correspondence of the 320 keV peak is the linear background fitted in the neighbourhood of peak, that will be subtracted for the net counting rate evaluation.

The neutron detector efficiency can be calculated by the ratio between the neutrons detected N_n divided by $N_{^{51}\text{Cr}}$, the number of ^{51}Cr nuclei produced



FIGURE 3.28: Setup used for the activation measurement: the ^{51}V target irradiated with proton is inserted in the blue container, shielded by external environmental background

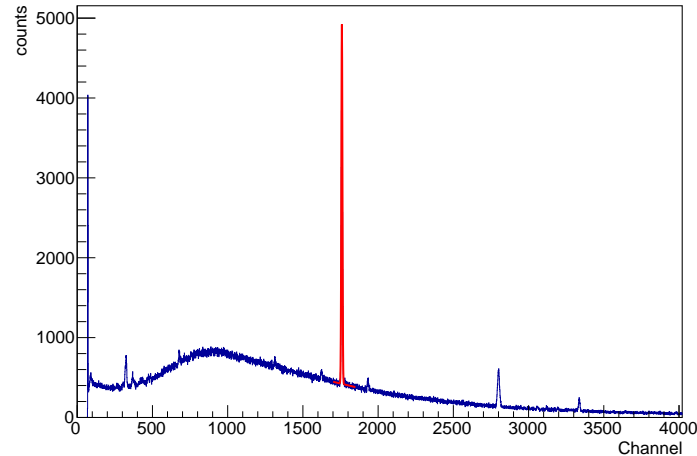


FIGURE 3.29: An example of γ -ray spectrum from the ^{51}V decay. The 320 keV peak is fitted with a Gaussian curve plus a linear background.

during the target proton irradiation, in ratio 1:1 with the neutron emitted from the target.

The number of neutrons detected was corrected by the dead time in each channel using the ratio between the pulser counts in the ^3He counter's channels and the pulser count in the free channel.

A neutron spectrum acquired is shown in Figure 3.30.

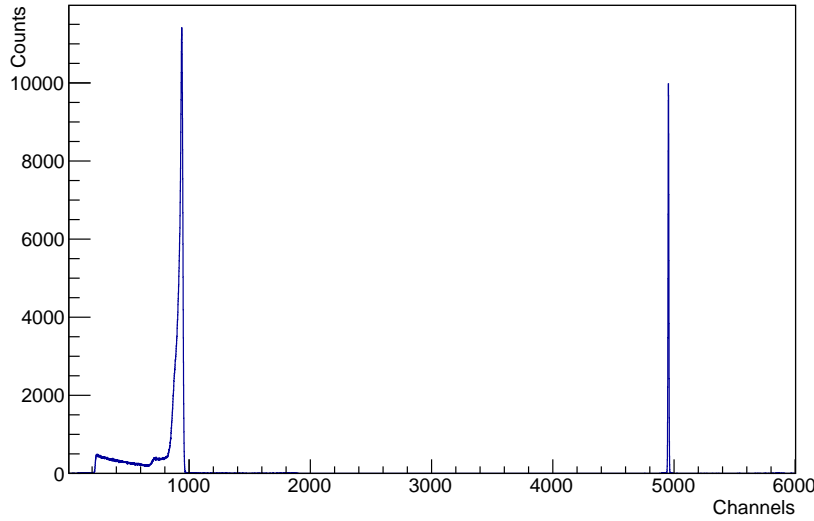


FIGURE 3.30: A neutron spectrum acquired during the efficiency campaign with the $^{51}V(p,n)^{51}Cr$ reaction: the neutron peak is evident and the pulser peak is at higher energies

$N_{^{51}Cr}$ can be calculated by means of the activation measurement detecting the γ -ray spectrum with the HPGe detector.

The timing of the activation measurement is schematized in Figure 3.31: assuming that at T_0 the proton irradiation is stopped, after a cooling time $T_1 - T_0$, we started the HPGe measurement at T_1 : a corrective factor must be applied in order to take into account the ^{51}Cr decay in this cooling time.

Being precise, a correction should be applied also considering that ^{51}Cr decays also during the proton irradiation time on the vanadium target, but due to the fact that the irradiation time is much shorter than the half life time of ^{51}Cr , we can neglect this contribution.

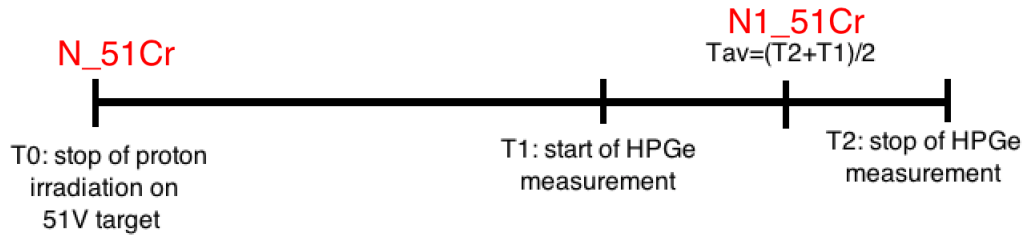


FIGURE 3.31: Scheme of the activation measurement. At T_0 a number of $N_{^{51}Cr}$ are produced after the proton irradiation of ^{51}V . The activation measurement starts after a time transient in T_1 . At half of the irradiation measurement the Number of ^{51}Cr nuclides is $N_{^{51}Cr51} = N_{^{51}Cr} e^{-\lambda(T_{av} - T_0)}$.

In the time window $\Delta t_a = T_2 - T_1$ we can assume that the activity of the source A is constant, due to the fact that the activation measurement time is

much shorter than the ^{51}Cr decay time.
Considering the well known decay law:

$$A_{51\text{Cr}} = -\frac{dN}{dt} = \lambda N_{51\text{Cr}} \quad (3.5)$$

where λ is the decay constant of the radioactive source and $N_{51\text{Cr}}$ is the total number of radioactive nuclides during the Germanium measurement. This is linked with the $N_{51\text{Cr}}$ through integration of the decay law: $N_{51\text{Cr}} = N_{51\text{Cr}} e^{-\lambda \Delta T}$, where $\Delta T = (t_{av} - t_0)$ is the elapsed time between the end of the proton irradiation and the half of the activation measurement.

The activity, i.e. the number of decays per unit of time, can be estimated from the net counts of γ -rays in the 320 keV peak opportunely corrected considering the dead time, the HPGe efficiency at 320 keV $\eta_{\gamma 320}$ and the Branching Ratio to the 320 keV B , divided by the time measurement $\Delta t_a = t_2 - t_1$.

Resuming, the neutron detector efficiency can be calculated with the equation 3.6

$$\eta_n = \frac{N_n}{N_{\gamma(320\text{keV})}} \eta_{\gamma 320} B e^{-\lambda(\Delta T)} * \Delta t_a * \lambda \quad (3.6)$$

In Table 3.9 are summarised the main quantities necessary for the calculation. Here I will illustrate results for both setups.

TABLE 3.9: Parameters used in Formula 3.6 for the efficiency evaluation with the $^{51}\text{V}(p, \gamma)^{51}\text{Cr}$ reaction.

Parameter	Value
$T_{1/2}$ (days)	27.703 ± 0.003
B (%)	9.91 ± 0.1
$\eta_{\gamma 320}$ (%)	13.4 ± 0.4

In Table 3.10 the proton energy of the run E_p , proton irradiation time T_{irr} , cooling time ΔT , activation measurement time Δt_a , number of gamma detected after the linear background subtraction $N_{\gamma(320\text{keV})}$ and efficiency calculated according Formula 3.6 are reported.

Efficiency overall uncertainty, estimated after error propagation, is of the order of 5%.

TABLE 3.10: Single target setup efficiency measurements

Targets	E_p (keV)	T_{irr} (s)	N_n	ΔT (s)	Δt_a (s)	$N_{\gamma(320\text{keV})}$		Efficiency	
						Value	error	Value	error
S-V5	1700	5100	22364512	93612	241133	40906	3365	0.4665	0.023
S-V6	2000	6000	39581320	347335	154757	44872	5202	0.4544	0.0227
S-V4	2300	4800	20010543	4643	107970	18189	4934	0.4396	0.0216

The data and the simulated efficiencies are shown in Figure 3.32, represented by the blue points and the red curve, respectively.

The efficiency curve from the Geant4 simulation code has to be scaled by a factor 0.82 to match experimental data. An overestimation of the simulated efficiency has been observed for similar setups in the past [67, 60]. The reason for deviations between measurements and simulations is unknown, but most likely the differences have to be attributed to a combination of factors. These

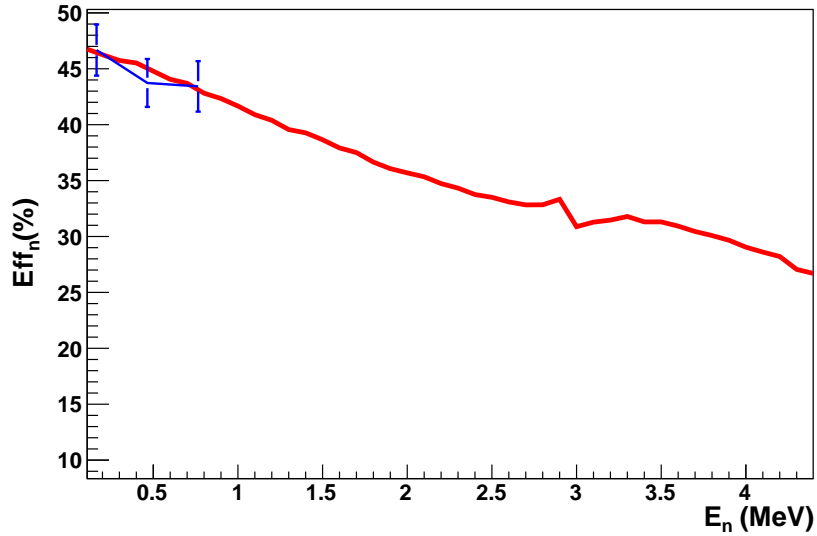


FIGURE 3.32: Comparison between efficiency experimental blue points calculated with the $^{51}V(p,n)^{51}Cr$ reaction and the MC Geant4 efficiency red curve scaled of a factor 0.82 to overlap data.

include experimental uncertainties in the neutron scattering cross-sections used in the simulations, especially in the modelling of molecular effects during the moderation of the neutrons in the polyethylene. Also, slight deviations between the physical density of the moderator and the value used in the calculations has an effect on the efficiency of the actual setup. Figure 3.33 shows the comparison between the ratio of the efficiencies of the two radii, outer divided by inner, with the experimental data. The agreement and the overlap between the experimental dataset and the simulation data, the blue points and the red curve, respectively, indicated that also the simulation is under control also from this point of view. The efficiency for the Single Target chamber can be parametrized with the function

$$\eta_{ST}(E_n) = 47.49 - 6.48E_n + 0.5E_n^2 - 0.02E_n^3, E_n \text{ in MeV} \quad (3.7)$$

The same data analysis was performed for the Multi Target setup. In this case we acquired measured efficiency in correspondence of the three energy points listed at the beginning of the Section and we added one more point at $E_p=2600$ keV, corresponding to a neutron energy of 1 MeV where literature [68] predicted a negligible contribution of the n_1 neutron group to the total flux.

In Table 3.11 the results of the Multi Target efficiency campaign are shown.

TABLE 3.11: Multi target setup efficiency measurements

Targets	E_p (keV)	T_{irr} (s)	N_n	ΔT (s)	Δt_a (s)	$N_{\gamma(320keV)}$		Efficiency	
						Value	error	Value	error
V3	1700	7394	10911544	103968,5	82777	7914	119	0.4281	0.0202
V2	2000	2657	13696816	85980	68381	8559	117	0.4126	0.0221
V6	2300	3577	12081008	123960	71980	8027	70	0.4040	0.0242
V5	2600	7273	8976250	248580	172752	14468.2	167.9	0.3855	0.020754

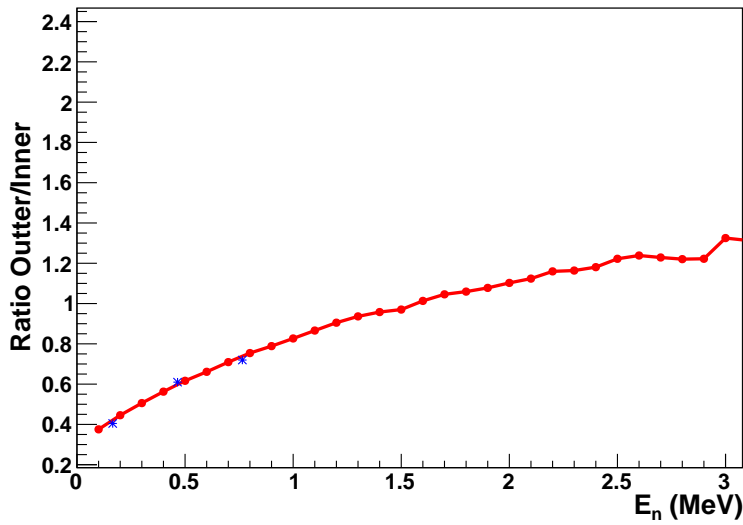


FIGURE 3.33: Comparison between efficiency experimental acquired with the Multi Target setup. The blue points are calculated with the $^{51}V(p, n)^{51}Cr$ reaction and the MC Geant4 efficiency red curve is scaled down of a factor 0.82 to overlap data.

Also in this case the efficiency curve extracted from Geant4 simulations must be scaled by a factor 0.8 to overlap experimental Data. The comparison after the scaling is shown in Figure 3.34 The efficiency for the Single Target

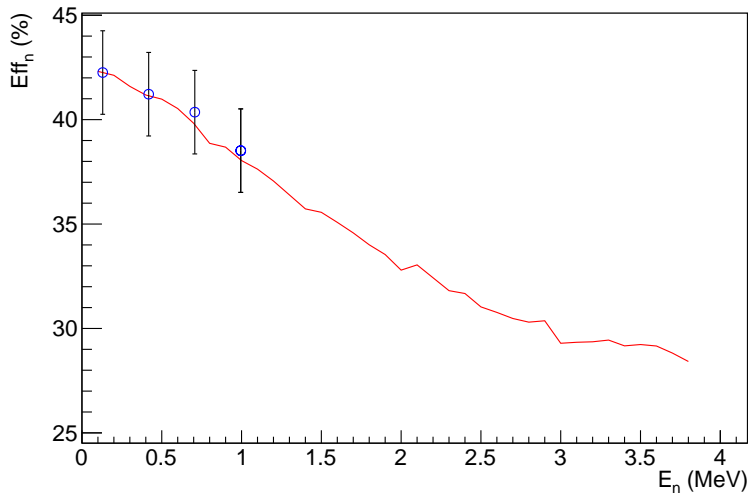


FIGURE 3.34: Comparison between efficiency experimental acquired with the Multi Target setup. The blue points are calculated with the $^{51}V(p, n)^{51}Cr$ reaction and the MC Geant4 efficiency red curve is scaled down of a factor 0.82 to overlap data.

chamber can be parametrized with the function

$$\eta_{MT}(E_n) = 42.74 - 2.91E_n - 2.52E_n^2 + E_n^3 - 0.1E_n^4, E_n \text{ in MeV} \quad (3.8)$$

The discrepancy of 10%, predicted by Geant4 simulation (Figure 3.18B) in the low energy part of the curve is confirmed by experimental measurements.

Chapter 4

The target characterization

In this chapter, I will describe all the procedures that permitted to keep under control the target modification during the measurements.

I will start from the description of the evaporation process used for the target preparation (Section 4.1).

As already mentioned in previous chapters, one of the most important sources of systematic uncertainties comes from the target modification due to the degradation, change of stoichiometry, possible blistering effect, the appearance of bubbles on target surface due to alpha bombardments.

A crucial aspect in absolute cross section measurements with solid targets is the monitoring of the target itself.

It is of paramount importance that targets and backings contain minimum contaminations.

Indeed, trace contaminants may be present in targets, and if their cross section can be higher than the one to be measured, they would dominate the spectrum under study.

Using the purest materials alone does not eliminate pollutant impurities, since these can occur in next steps, like production, handling of targets and target irradiation.

Methods of cleaning backing materials, quality of products used for target preparation, the target preparation procedure and analysis on the target stability are described in next sections.

After the introduction of useful experimental concepts needed for the analysis (Section 4.2), I will describe the target characterisation performed to verify the conditions described (Sections 4.3 and 4.4).

4.1 Target preparation

In most of the past work in literature [19, 34], ^{13}C solid targets are produced evaporating ^{13}C enriched powder on backings.

Another possibility could be the ion implantation, performed shooting accelerated ^{13}C ions on a backing. This procedure would be very expensive.

After some tests performed, the collaboration concluded that a reliable and feasible solution was the evaporation procedure, described in more details in next sections.

Before the production of the ^{13}C target, it is necessary to prepare backings for the deposition of the target material. The backings are usually made of a heavy material (e.g. Tantalum, Gold, Copper): for these elements the Coulomb barrier is so high that is very unlikely to generate reactions with the beam projectiles. In this measurements Tantalum backings have been

used, because cheaper and easy to machine.

A cleaning procedure is important in order to remove from Ta surface traces of light elements (e.g. Hydrogen, Oxigen, Flourine, Boron). All these possible contaminants could easily generate beam induced background.

The etching procedure for Ta is well established [69].

Ta backings are washed with isopropyl alcohol and with a 2% solution of detergent (e.g u90 Aldrich) in a ultrasonic bath in order to remove impurities on surface.

After the drying, targets are washed again with a solution of three acids (150 ml H₂SO₄ conc.+60 ml HNO₃ conc. +72 ml HF conc. (40%)). This solution removes impurities of light elements inside the backing, but on the other side it can increase the level of beam induced background due to the presence of Fluorine.

For this reason LUNA collaboration developed an alternative cleaning method, where backings are let for few hours in a solution with citric acid at 5-10% + 1% H₂O₂ in ultrasonic bath.

This procedure was used in the case of Ta backing used as support for the ¹³C.

After cleaning procedure, the deposition process follows: during my phD work I personally took care of the production of evaporated targets.

They were fabricated using MTA ATOMKI *Leybold UNIVEX 350 vacuum evaporator*, showed in Figure 4.1.

Powder used for the evaporation was produced by Sigma Aldrich, that guarantees a 99% enriched powder with 99% purity (<https://www.sigmaaldrich.com/catalog/product/aldrich/277207?lang=it®ion=IT>).

Before the evaporation phase, one needs to press ¹³C powder in more solid pellets using an hydraulic press: this allowed to the material to be more resistant and more localized in the melting pot in the vacuum chamber.

Basically the technique consists in heating up the material to evaporate in a vacuum chamber.

Due to the high melting point of Carbon (3600°C), the electron gun evaporation technique is the only possible solution, because the heated resistive boat cannot reach those high temperatures.

The vacuum chamber is shown in Figure 4.2.

Electrons are emitted by thermoionic effect and guided in the melting pot by means of an electric and a magnetic field.

The beam controller is shown in Figure 4.3. In Table 4.1 the beam parameters considered optimal and fixed during all the evaporation campaigns in order to guarantee the reproducibility of the procedure.

An oscillator quartz mounted inside the vacuum chamber at a fixed distance far from the melting pot (16 cm) was used to monitor the evaporation: the key concept behind this is that the ¹³C powder evaporates isotropically and is deposited also on the quartz. The oscillation frequency will drop as the crystal's mass is increased by the material being deposited on it. To complete the measurement system, an electronic instrument continuously reads the frequency and performs appropriate mathematical functions to convert that frequency data to thickness data, both instantaneous rate and cumulated thickness [70]. The value of the thickness (in kÅ) was not assumed as an absolute value, but as a reference point: fixing all the other setup parameters



FIGURE 4.1: The evaporation setup: on the left the vacuum chamber and on the right the control panel for the beam, the vacuum system and the monitoring of the quartz. All these parts will be described in next sections.



FIGURE 4.2: The vacuum chamber and all the main components: in white the hole where the electron beam comes from, in red the melting pot of the material, in green the nipper where the backing is hold, in light blue the quartz used to monitor the evaporation process.

(beam parameters, distance of the backing from the melting pot) if the material deposited on the quartz is fixed, it is reasonable to assume that also the material evaporated on the Ta backing is the same.

An example of evaporated target is shown in Figure 4.4.



FIGURE 4.3: Beam controller

parameter	Value
Pellet position	
distance between backing and melting pot	8.3 cm
distance between melting pot and quartz	16 cm
Beam setting	
latitudinal freq	3.0
latitudinal ampl	0.4
longitudinal freq	4.7
longitudinal amplitude	0.9
mod amplitude	0.9
Target properties for quartz	
density	2.25
acoustic impedance	2.71

TABLE 4.1: Setting of the evaporator parameters



FIGURE 4.4: Enriched ^{13}C target evaporated: It is visible on the top the lighter zone where the target was hold during the evaporation procedure

For all the campaigns of the $^{13}\text{C}(\alpha, n)^{16}\text{O}$ reaction cross section measurements, I evaporated more than 100 targets, using an overall amount of enriched powder of 7 grams.

4.2 Experimental quantities

Before to go ahead with the description of the characterization, I will introduce few useful experimental quantities that will be used for the spectra analysis in this and in the next Chapter.

The yield Y is defined as the number of reaction products emitted (γ -rays or

particles) N_e per incident particle N_p on target:

$$Y = \frac{N_e}{N_p} \quad (4.1)$$

Another related quantity is the experimental Yield Y_{exp} , that is the number of particles or γ -rays detected N_d per particle incident on the target. The experimental Yield is related to reaction Yield through the relation:

$$Y_{exp} = \eta Y \quad (4.2)$$

where η is the detector efficiency.

The curve that describes the Yield of a reaction channel as a function of the bombarding projectile energy is defined excitation function.

Another quantity that will be used in this work is the stopping power $\epsilon(E)$, the energy loss of the particle inside a given material divided by the material density ρ .

$$\epsilon(E) = -\frac{1}{\rho} \frac{dE}{dx} \quad (4.3)$$

Values of stopping power are tabulated with a given uncertainty in the SRIM (Stopping and Range of Ions in Matter) database [50] as a function of the energy of projectile in laboratory system. In particular data from the 2008 will be used for my analysis.

In general the target used in the reaction can be prepared using a compound where there are active nuclei A and inactive ones I . The latter are spectator of the reaction under study, but of course interact with projectiles.

Assuming a given compound with the stoichiometry $A_a I_i$, the effective stopping power ϵ_{eff} can be estimate by means of the Formula [6]:

$$\epsilon_{eff}(E) = \epsilon_a(E) + \sum_i \frac{n_i}{n_a} \epsilon_i(E) \quad (4.4)$$

Suppose that a beam of energy E_0 hits the target. Projectiles pass trough the target losing energy.

We can assume that the target can be divided in slices of infinitesimal thickness dx_i , such that the energy lost by the beam in each slice, dE_i , is small. In this thickness also the cross section σ_i is constant over dx_i .

In each layer the infinitesimal Yield dY_i can be defined as:

$$dY_i = \sigma_i n_i dx_i \quad (4.5)$$

where n_i is the active nuclei number density.

The total yield inside the entire target with a thickness $\Delta E = \sum_i dE_i$, is given by the integration of partial yield in each layer:

$$Y(E_0) = \int \sigma(x) n(x) dx = \int_{E_0 - \Delta E}^{E_0} \frac{\sigma(E)}{\epsilon(E)} dE \quad (4.6)$$

For a narrow resonance with at energy E_R and gamma width Γ , ($\Gamma \ll E_R$), the energy dependence of the cross section is parametrized with the Breit-Wigner

formula:

$$\sigma_{BW}(E, E_R) = \pi \lambda^2 \omega \frac{\Gamma_a \Gamma_b}{(E - E_R)^2 + (\Gamma/2)^2} \quad (4.7)$$

where $\omega = \frac{2J+1}{(2J_p+1)(2J_t+1)}$ is the statistical factor that considers the spins of target nucleus J_t , projectile J_p and compound nucleus J , λ is the reduced wavelength of the projectile, Γ_a and Γ_b , such as $\Gamma_a + \Gamma_b = \Gamma$, are the partial width for the formation and decay of the compound.

In the case of thick target, we are in the condition $\Delta E \gg \Gamma$. Assuming that all the other quantities are constant over the energy range of the target, the yield is given by

$$Y(E_{p,lab}) = \frac{\lambda^2}{2\pi} \omega \gamma \frac{M+m}{M} \frac{1}{\epsilon} \left[\arctan\left(\frac{E_{p,lab} - E_R}{\Gamma/2}\right) - \arctan\left(\frac{E_{p,lab} - E_R - \Delta E}{\Gamma/2}\right) \right] \quad (4.8)$$

The excitation function for a thick target yield curve has the typical double arctangent shape, and the plateau height is proportional to the strength of the resonance and independent on the target thickness.

In case of non resonant mechanism, Formula 4.6 is used, sometime estimated with some approximations.

In case the target thickness is much smaller than the beam energy ($\Delta E \ll E_0$), the stopping power $\epsilon(E)$ can be assumed constant over the energy interval in the target and this can be taken out from the integral:

$$Y(E_0) = \frac{1}{\epsilon(E_0)} \int_{E_0 - \Delta E}^{E_0} \sigma(E) dE \quad (4.9)$$

If also the cross section is energy-independent or slightly energy dependent over this interval, one can use the linear approximation and the cross section can be extracted from the yield using the inverse formula

$$\sigma(E_{eff}) = Y(E_0) \epsilon(E_0) / \Delta E \quad (4.10)$$

In the equation 4.10 it has been necessary introduce the so called effective cross section $\sigma_{eff} = \sigma(E_{eff})$ defined as the averaged value of the cross-section over the target interaction energies.

One may note that in this case the cross section determination is dependent on the target thickness and, as we will see in next chapter, very sensitive to the target degradation [71]. The estimation of effective energy, assumed as the real energy where the reaction occurred, must be very precise due to the passage from the cross section to the S(E)-factor, begin the energy in a exponential term.

Furthermore, these approximations are not valid anymore if the cross section strongly depends on energy.

I will show that this condition is valid for the $^{13}C(\alpha, n)^{16}O$ reaction, so in next chapter, devoted to the cross section evaluation, it will be necessary an alternative approximation. In this chapter we will use the thick target approach for the characterization of enriched ^{13}C targets at MTA Atomki. Furthermore in the second part of the characterization performed with the LUNA accelerator we will calculate the reaction yeld with the definition in Formula 4.1.

4.3 Target characterization at 2 MV Tandetron at MTA ATOMKI

In order to verify the evaporation reproducibility and uniformity, a target characterization was performed by me together with the Hungarian group through the $^{13}\text{C}(p, \gamma)^{14}\text{N}$ reaction ($Q = 7550.56$ keV) using the 2 MV Tandetron installed at MTA Atomki (Hungarian Academy of Sciences).

The setup used was quite similar to the LUNA's one and is described here. A gate valve was used to insulate the accelerator from the rest of the beamline. The target chamber was electrically insulated and the target was used as Faraday Cup in order to collect the charge, connecting it to a digital current integrator ORTEC 439.

An HPGe of 100% relative efficiency at 0° was installed at around 3 cm from the target in order to detect prompt γ -rays emitted by the $^{13}\text{C}(p, \gamma)^{14}\text{N}$ reaction.

Signals were shaped using a preamplifier and then spectra were acquired using the NIM ASPEC Multi Channel Analyzer and a PC with the Maestro software installed.

The position between target and HPGe is shown in Figure 4.5.

Targets were irradiated with a proton beam with an average current as low

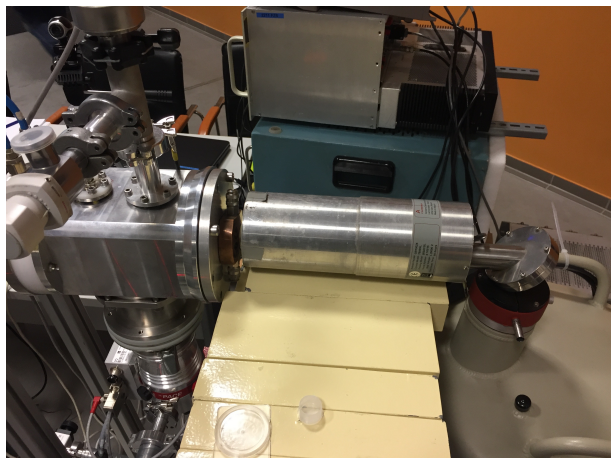


FIGURE 4.5: The setup used at MTA Atomki for the measurement of the $^{13}\text{C}(p, \gamma)^{14}\text{N}$ reaction; the HPGe is at 0° respect to the beamline direction

as 500 nA .

This has a double advantage:

- the beam power on target is 10 times lower than at LUNA, so its degradation is negligible
- neither cooling system nor clod trap are necessary in the setup

In particular targets were scanned by means of the narrow resonance $E_{R,lab} = 1748\text{keV}$ ($\Gamma = 122\text{ eV}$) [72]: when the beam energy is higher than the resonance energy, particles lose energy inside the target and the resonance level

is populated inside the target itself; once the energy is high enough the resonance is not populated anymore and the yield decreases to zero.

The experimental Yield defined as in Formula 4.1 was estimated in the region of interest integrated included the full, first escape and second escape peaks of the transition $E_{R,lab} \rightarrow GS$.

Figure 4.6 shows an example of spectrum acquired with ORTEC MAESTRO Data Acquisition System. The red part is the ROI used for the evaluation of the experimental yield.

The γ -ray energy emitted E_γ is related to the captured proton energy, apart

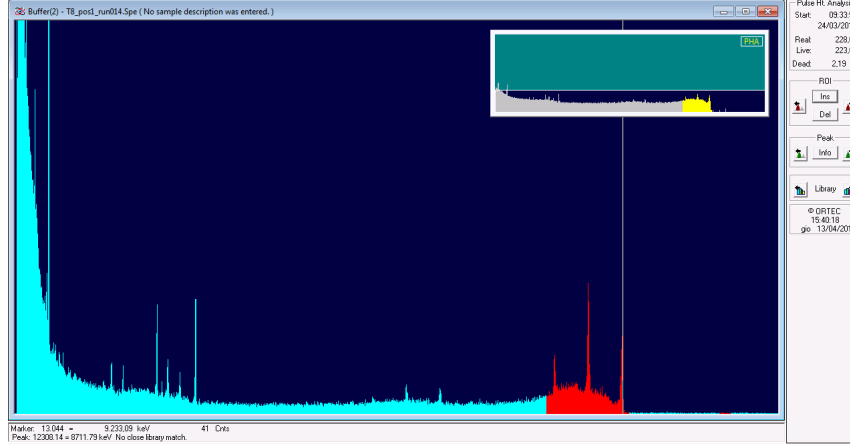


FIGURE 4.6: Example of spectrum acquired, the red part is the ROI used for the analysis.

from Doppler and recoil corrections, by the relation $E_\gamma = Q + E_{p,lab} \frac{M_t}{M_p + M_t}$ where Q , M_t , and M_p are the Q-value of the reaction, and the target and projectiles masses, respectively.

Therefore the capture to the ground state is expected at $E_\gamma = 9175$ keV. Moreover the large cross section at resonance $E_R = 1748$ keV permits to get a statistical uncertainty lower than 1% in less than 3 minutes.

In these conditions it is possible to consider the environmental background negligible respect to the signal from the reaction, as shown in Figure 4.7: spectrum of $^{13}C(p, \gamma)^{14}N$ and environmental background one are normalized to time.

In the region of interest the background counting rate is more than five orders of magnitude lower then $^{13}C(p, \gamma)^{14}N$ one.

Being in the condition of thick target (i.e. target thickness $\gg \Gamma$) the γ -ray reaction yield as a function of proton energy near the resonance has a double arctangent, described in Equation 4.8 [6], as it shown in Figure 4.8.

The front leading edge is determined by the convolution of the beam resolution and the natural width of the resonance; this is followed by a constant plateau where the height is proportional to the inverse of the compound stopping power. The falling edge at higher proton energy is larger then the leading one because of the contribution of the straggling effect.

The fit profile is shown in Figure 4.8 (red line).

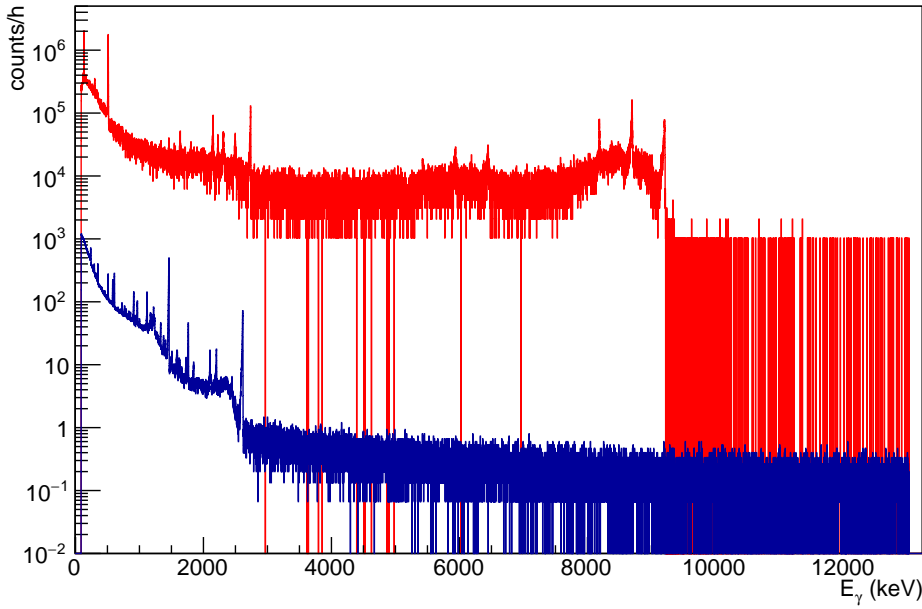


FIGURE 4.7: (Colour online) Comparison between the spectrum acquired during the $^{13}\text{C}(p, \gamma)^{14}\text{N}$ measurement and a background, in red and in blue respectively. Spectra are normalized to time. In the region of interest the background is negligible.

$$Y(E_{p,lab}) = k * (\text{ATan}(\frac{E_{p,lab} - E_R}{\Gamma_1/2}) - \text{ATan}(\frac{E_{p,lab} - E_R - \Delta E}{\Gamma_2/2})) + bckg; \quad (4.11)$$

k is a normalization constant, E_R is the energy of the resonance, corresponding to the abscissa of the point at half of the raising edge of the profile, Γ_1 and Γ_2 are the steepness of the leading and falling edge respectively and $bckg$ is the background component.

The FWHM of the Yield profile represents the target thickness in unit of energy [73].

Considering that the beamspot radius is few mm and using a dedicated set

TABLE 4.2: Parameters extracted from the fit of the excitation function in Figure 4.8

NAME	VALUE	ERROR
k	1.963e+00	2.8e-02
E_R	1.749e+03	6.7e-03
ΔE	2.313e+00	1.4e-02
Γ_1	3.272e-01	1.86e-02
Γ_2	1.58e+00	3.8e-02
$bckg$	1.44e-01	2.56e-02

up that permitted to rotate an off axis target holder, we could hit targets in different points and test the uniformity of the evaporation.

Figure 4.9B shows the results of the irradiation in three different points, P1,P2

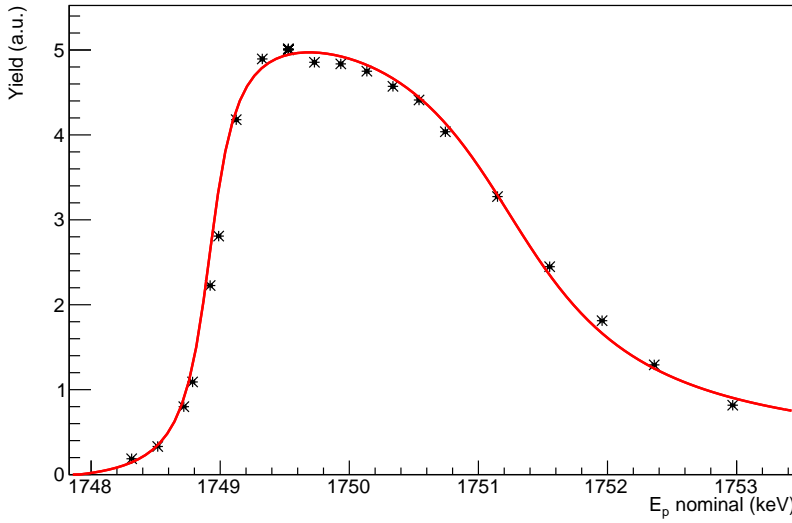


FIGURE 4.8: The excitation function of the $^{13}\text{C}(p, \gamma)^{14}\text{N}$ reaction at $E_R = 1748$ keV. Parameters of the fit are listed in Table 4.2

and P3, qualitatively indicated by red circles in Figure 4.9A.

In Table 4.3 the fit parameters of the thick target yields obtained in P1,P2 and P3 using the Formula 4.11 are listed.

The thickness parameter ΔE , highlighted in the light blue row, shows a maximum discrepancy of 3%: so it is reasonable to claim that the deposition uniformity is guaranteed at level of 3%.

There are discrepancies at the level of few percent for the parameters k , E_R

TABLE 4.3: Fit parameters from the resonance scan in P1,P2,P3

parameter	pos1	pos2	pos3
k (a.u)	1.780(9)	1.748(22)	1.657(30)
E_R (keV)	1748.741(6)	1748.876(8)	1748.914(6)
ΔE (keV)	4.587(13)	4.589(18)	4.407(23)
Γ_1 (keV)	0.258(11)	0.245(13)	0.269(11)
Γ_2 (keV)	2.130(26)	2.319(37)	2.425(84)

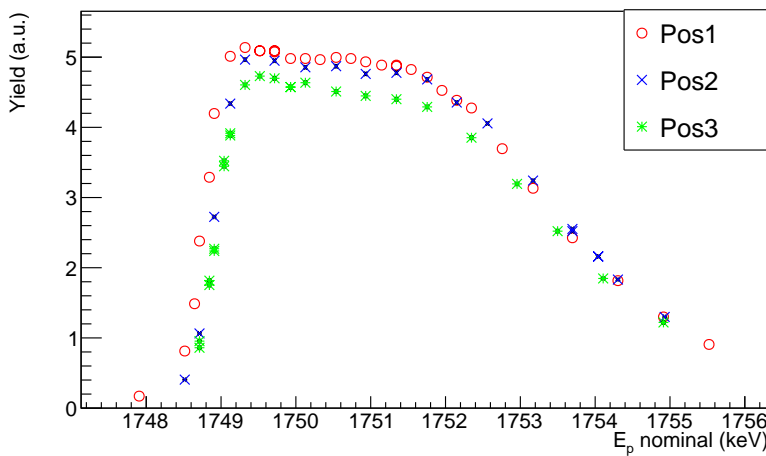
and Γ_2 . The discrepancy for k is due the fact that the relative position between the target and the HPGe detector changes with the rotation of the target holder. E_R is due to instabilities in the motor generator of the accelerator: during the transient time for the warm up of the machine, its parameters, e.g the extraction voltage, can be influenced by temperature changes and reach the stability after certain time Γ_2 is mainly related to the roughness of the Ta backings.

The uniformity of the evaporation was checked in few targets : for the rest the excitation function at $E_R = 1748$ keV was measured in a single point.

In Table 4.4 the targets produced in November 17 are listed; I report in the



(A) An example of evaporated target:
the red circles qualitatively indicate
different irradiation points
for the uniformity evaporation
test.



(B) (Colour online) The three resonance profiles in different target points:
the difference in the plateau height is due to the different relative position
between beamspot and HpGe that changes the efficiency of the measure-
ment; the shift in the raising edge was due to instabilities in the motor
generator of the accelerator

FIGURE 4.9

Table also the quartz parameter that indicates the quantity of material deposited on the backing during the evaporation procedure and the thickness ΔE (keV) measured with the thick target yield approach.

In Figure 4.10 the thickness parameter extracted from the fit profile ΔE is plotted as a function of the quartz thickness ΔE_q : the Pearson correlation coefficient [74] of the points of the cluster of targets evaporated in November is 0.674, revealing a moderate correlation between the two quantities. Looking at table of critical values for Pearson's R, the probability that this value is accidentally produced by uncorrelated variables is 1.4%; so at the confidence level of 99% we can say that the two variables are linearly correlated. This means that, fixing parameters in table 4.1, it is possible to take the quartz indicator as reference point to produce targets with a thickness between 3 and 5 keV for a proton energy of $E_R = 1748$ keV.

Another test performed during the target characterization campaign at MTA

TABLE 4.4: Summary of the parameters of the evaporated targets produced in November 2017

target	ΔE_q (kÅ)	ΔE (keV)	$\delta \Delta E$ (keV)
MT1	0.33	3.258	0.012
MT2	0.35	2.576	0.02
MT3	0.39	3.428	0.015
MT4	0.4	4.322	0.02
MT5	0.35	3.234	0.019
MT6	0.4	3.489	0.02
MT7	0.42	3.644	0.02
MT8	0.44	4.488	0.021
MT9	0.45	3.698	0.02
T18	0.44	4.634	0.019
T19	0.48	4.581	0.019
T20	0.5	4.216	0.018
MT10	0.5	4.886	0.02
T21	0.55	4.466	0.02
MT11	0.5	3.6789	0.022

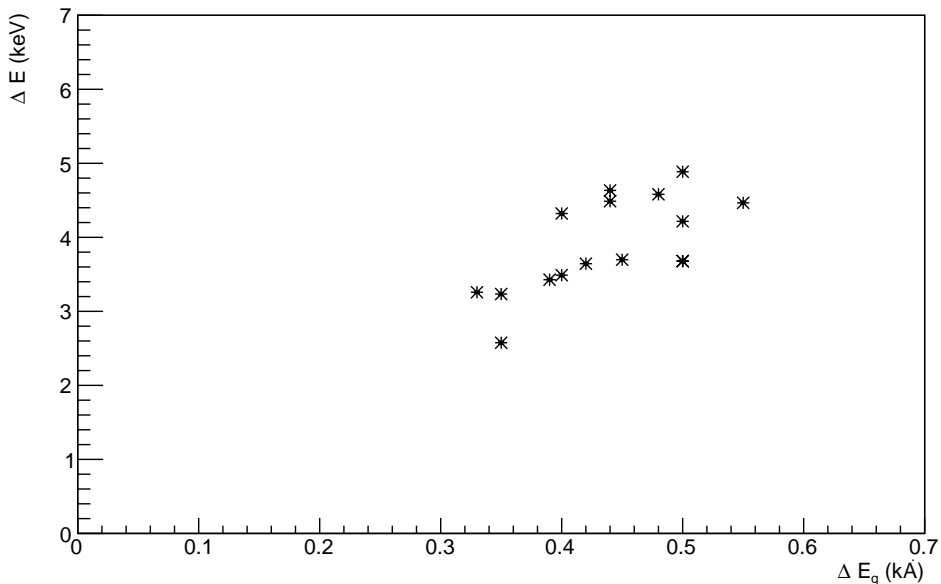


FIGURE 4.10: Plot of the thickness of the target measured with the resonance scan and the thickness monitored online with the evaporator: the Pearson correlation coefficient shows a moderate correlation

ATOMKI regarded the double check on the purity of the powder provided by Sigma Aldrich.

A natural carbon target, with the well known ^{13}C abundance of 1.1%, was evaporated following the same procedure described for the Section and the $^{13}\text{C}(p, \gamma)^{14}\text{N}$ excitation function was measured integrating counts in the usual region of interest of the peaks relative to the $E_R \rightarrow GS$ transition.

Figure 4.11 shows the comparison of the natural carbon excitation function

and the 99% ^{13}C enriched one, indicated by blue squares and red circles, respectively. Uncertainties are at the level of percent and are not visible.

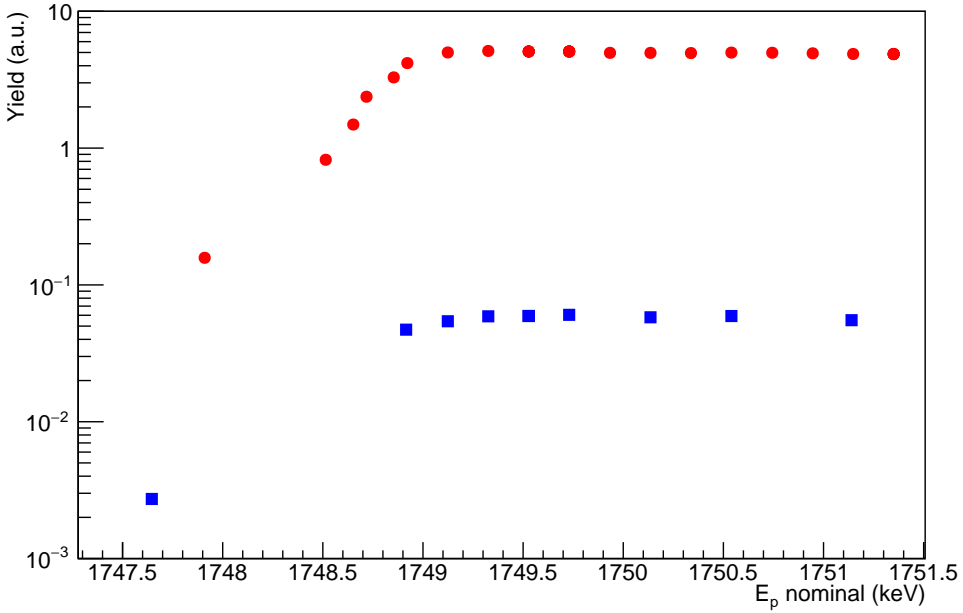


FIGURE 4.11: Comparison of the $^{13}\text{C}(p, \gamma)^{14}\text{N}$ excitation function of a natural carbon and an enriched one (blue squares and red points, respectively). Uncertainties are at the level of 3%.

Because all the experimental conditions (e.g relative distance between HPGe and target) were fixed, the plateaux's height is directly proportional to the abundance of the ^{13}C in the target and to the target active stopping power.

For both profiles the average Yield in the plateau was calculated, obtaining $Y_{\text{nat}} = 0.0576 \pm 0.0016$ in front of $Y_{^{13}\text{C}} = 5.094 \pm 0.077$. Assuming x the abundance of ^{13}C in the Sigma Aldrich powder, this can be calculated with a proportion with the stopping powers:

$$\frac{Y_{^{13}\text{C}}}{Y_{\text{nat}}} = \frac{(1 + \frac{1.1}{98.9})\epsilon_C}{(1 + \frac{1-x}{x})\epsilon_C} = 90.8x \quad (4.12)$$

where ϵ_C is the stopping power of protons in Carbon and the effective stopping power is calculating using the formula of stopping power for compounds with a mixture of active and inactive nuclides [6]:

$$\epsilon(E) = \epsilon_a(E) + \sum \frac{N_i}{N_a} \epsilon_i(E) \quad (4.13)$$

The ^{13}C abundance estimated in the powder is $(97.1 \pm 2.3)\%$, compatible with the 99% claimed by the company.

Concluding all these tests indicated that:

- the evaporation is uniform

- the evaporation is reproducible and under control
- all the evaporated enriched targets have the same composition compatible with the value provided by Sigma Aldrich

4.4 Target characterization at LUNA accelerator

The second part of the target characterization took place at LNGS, with the LUNA 400 accelerator. Here it was possible to verify the target resistance when irradiated with an higher intensity beam.

During these tests an average current of $120 \mu\text{A}$ was delivered on target.

Here the collaboration had to take into account that in the LUNA energy range, from 50 up to 400 kV, it is not possible to populate levels neither with the $^{13}\text{C}(\alpha, n)^{16}\text{O}$ nor in the $^{13}\text{C}(p, \gamma)^{14}\text{N}$ reactions.

For this reason the target degradation cannot be checked by means of the thick target Yield approach.

Looking the ^{14}N compound nucleus leve scheme in Figure 4.12, beyond the energy range that LUNA can exploit, coloured in cyan, there are resonances that could contribute with their tails in a lower energy window.

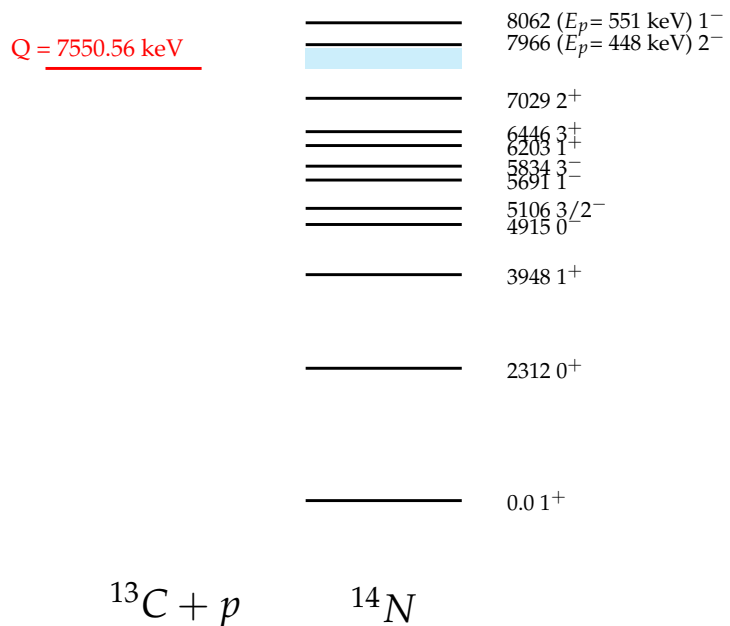


FIGURE 4.12: Level scheme of the ^{14}N compound nucleus. The cyan area indicates the energy window that could be exploited by the LUNA accelerator. In brackets the proton energy needed to populate a level beyond the Q value. No resonant states can be populated with the LUNA machine

The $E_R = 448 \text{ keV}$ is a narrow resonance ($\Gamma = 2.5 \text{ eV}$), so its contribution in the LUNA energy region is negligible.

We tested the possibility to face out this problem using an alternative method taking into account the contribution of the tail of the broad resonance at $E_p = 551 \text{ keV}$ ($\Gamma = 34.5 \text{ keV}$): this was calculated based on the the resonance parameters evaluated by Genard et al [75], summarized in Table 4.5.

These parameters have been used of the calculation of the contribution of the resonance at lower energies using the Breit Wigner Formula

$$\sigma(E_p)_{res} = (2l + 1)\omega \frac{\pi}{k^2} \frac{\Gamma_e \Gamma_r}{(E - E_R)^2 + (\Gamma_{tot}^2/4)} \quad (4.14)$$

TABLE 4.5: Parameters of the resonance at $E_R = 551\text{keV}$, evaluated by Genard et al [75]

$E_{R,cm}$ (keV)	Γ (keV)	$\omega\gamma$ (eV)
511.3(5)	34.5(1.1)	6.2(2)

All the terms are explained in the Iliadis' book [76].

The Direct component to the ground state is from King's paper [77] and is parametrized by the function

$$S_{DC}(E_p) = C^2 S (2.04 - 1.6 \cdot 10^{-3} E_p + 4.15 \cdot 10^{-7} E_p^2) \text{keV} \cdot b \quad (4.15)$$

where $C^2 S$ is the spectroscopic factor, that I calculated from the extrapolation to zero $S(0)=5.25$ keVb.

The plot of the comparison of the contributions of the two components as a function of the beam energy is shown in Figure 4.13.

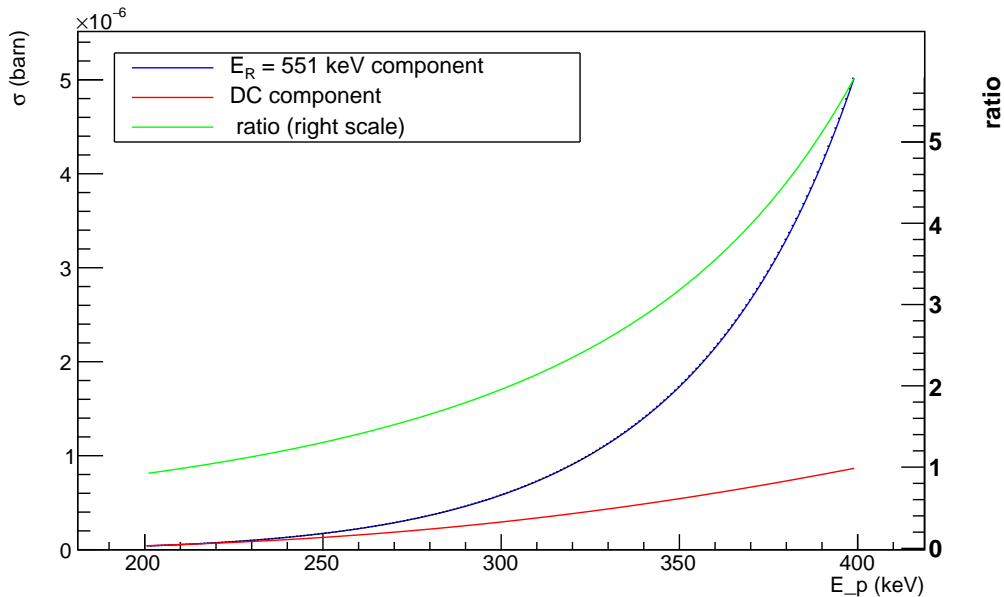


FIGURE 4.13: (Color online) The tail of the $E_r = 551$ keV resonance and the direct capture component are plotted as a function of energy separately. The ratio between the two is on right Y axis.

The blue and the red curves are the $E_R = 551$ keV cross section and the DC cross section component, respectively, as a function of the projectile energy. The green line, with the scale on the right of the plot, shows the ratio of the two components: the wide resonance has still a predominant component in the higher part of the energy range covered by the LUNA-400 accelerator. This means that the total cross section is still affected by the resonance tail as supposed.

The total cross section is evaluated as the incoherent sum of the resonance and DC components.

This property will be fundamental in the analysis for the $^{13}\text{C}(\alpha, n)^{16}\text{O}$ cross

section measurement described in the next chapter. In this part of the work, we can in any case take advantage from the increase of the cross section that permits to increase the Yield with better statistics.

For these measurements, an HPGe at 55°with a relative efficiency of 120% at a fixed distance of 5 mm from the target has been used for the detection of prompt gamma rays emitted by the $^{13}\text{C}(p, \gamma)^{14}\text{N}$ reaction.

In order to dissipate the beam power on target, a cooling system was connected and cooled down the target by mean of a continuous flushing of water on its back part.

A picture of the setup used for this measurement is show in Figure 4.14: the target chamber is insulated from the rest of the beam line and used as Faraday Cup for the measurement of the current on target. Then a current integrator converts the current in charge on target.

The HPGE is in close geometry in order to maximixe the efficiency. Moreover it is installed at 55°to minimize the effect of angular distribution, due to the fact that the Legendre polynomial $P_2(55^\circ)=0$.

The water flows through the two vertical tubes plugged into the target holder.

In order to test the target stability, we alternated long irradiations at differ-

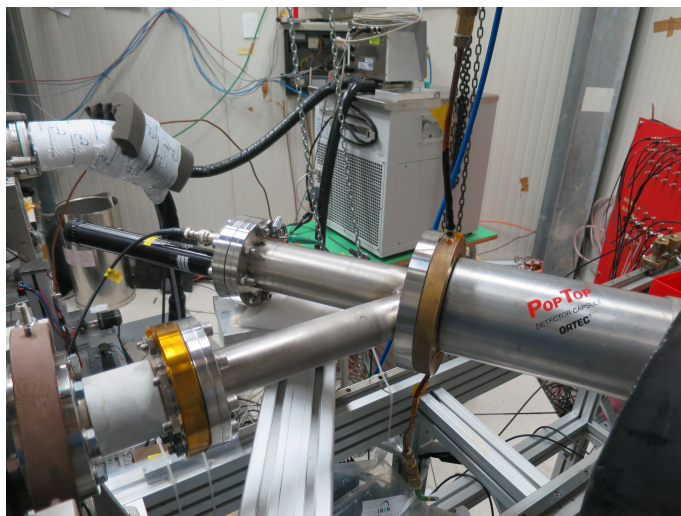


FIGURE 4.14: The set up used for the ^{13}C target characterization, described in the text.

ent energies with short irradiations always at the same energy $E_p = 310$ keV used as reference points.

From the relationship between the projectile energy E_p and the gamma energy emitted E_γ ,

$$E_\gamma = E_p \frac{M_T}{M_T + M_p} + Q - E_x + \Delta E \quad (4.16)$$

where M_T and M_p are the target and projectile masses respectively, Q is the Q-value of the reaction, E_x is the final level of the transition (in this case it is the ground state, so $E_x = 0$) and ΔE is the correction due to the Doppler and the recoil, considered negligible in this analysis.

For this reason the full energy peak that we want to monitor, from the DC to the ground state transition, is at $E_\gamma = 7843$ keV.

The reduction of the Yield as a function of the charge accumulated on target

was evaluated in the Region of interest highlighted in Figure 4.15. Measuring always at the same proton energy, permits to consider always the same ROI, so the detector efficiency is always the same and can be simplified.

The number of gamma emitted is, therefore, directly proportional to the number of active nuclei inside the target.

Therefore, plotting the Yield measured during the reference runs allows to have an idea of the modification of the targets during beam irradiation.

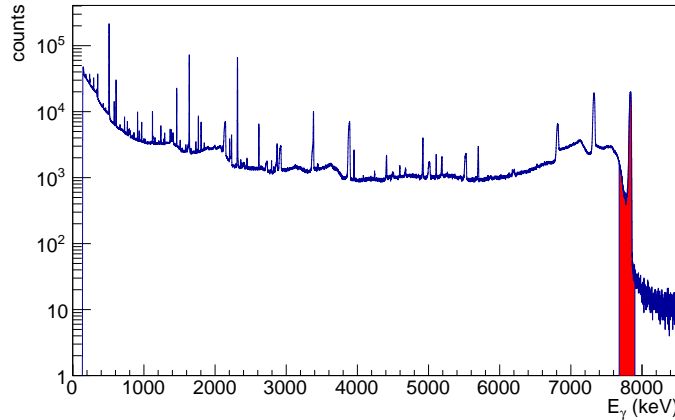


FIGURE 4.15: Spectrum emitted from the $^{13}\text{C}(p, \gamma)^{14}\text{N}$ with a proton energy $E_p = 1748$ keV. The red zone indicates the integration Region of interest for the Yield evaluation.

From the integration the raw area was obtained, and then, after a linear background subtraction, the net number of counts.

In Table 4.6 is summarized the list of reference measurements performed on one enriched ^{13}C target.

A total charge of 33.7 C of proton was accumulated on target. The plot of the

TABLE 4.6: Measurement performed with the LUNA400 accelerator for the characterization of one ^{13}C target

E_p [keV]	$\langle I \rangle$ (uA)	Q (uC)	cumulative Q (uC)
309.69	102	204611	204611
309.69	100	169779	6133250
309.69	136	146950	6942305
309.69	130	100239	8204004
309.69	132	185802	16015240
309.69	133	151171	17831062
309.69	137	156535	25058910
309.69	137	99866	27224378
309.68	145	120681	33811051

Yield in the reference points as a function of the cumulate charge is show in Figure 4.16. Error bars in the plot represent statistical uncertainties plus 3% of systematic associated to the reading of the charge on the target.

A linear fit was performed on the data, concluding that the yield reduction after 33 C of proton irradiation is less then 20%. This results implies that the

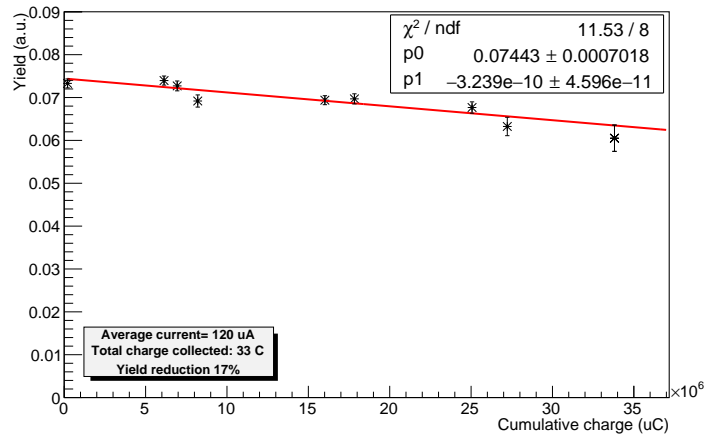


FIGURE 4.16: Yield in the ROI of the peak DC→ GS as a function of the cumulative charge: error bars include statistical uncertainties and a 3% of systematic uncertainty due to the reading of the charge: the degradation estimated is 17% after 33 C of protons.

^{13}C target degradation under a proton beam is negligible for short proton runs.

4.4.1 Beam induced background

After the analysis on the reference runs, a deep investigation was devoted to check possible contaminant nuclei inside the targets. In case of presence of pollutants that can open an (α, n) channel with a higher cross section than the $^{13}C(\alpha, n)^{16}O$ reaction, the beam induced background would be dominant and the measurement would be affected by larger uncertainties.

Main candidates are the two isotopes of Boron, ^{10}B and ^{11}B , that have a natural abundance of 20% and 80%, respectively.

The $^{10}B(\alpha, n)^{13}N$ ($Q = 1058$ keV) and $^{11}B(\alpha, n)^{14}N$ ($Q = 157$ keV) cross sections are many orders of magnitude higher than the carbon cross section.

Thanks to the gamma reduction background in the LNGS underground and to the high resolution provided by the HPGe, it is possible to identify and distinguish gamma rays emitted with low probability due to the low branching ratio of reactions with contaminant elements.

A spectrum acquired during a long measurement at $E_p = 310$ keV was evaluated and is shown in Figure 4.17.

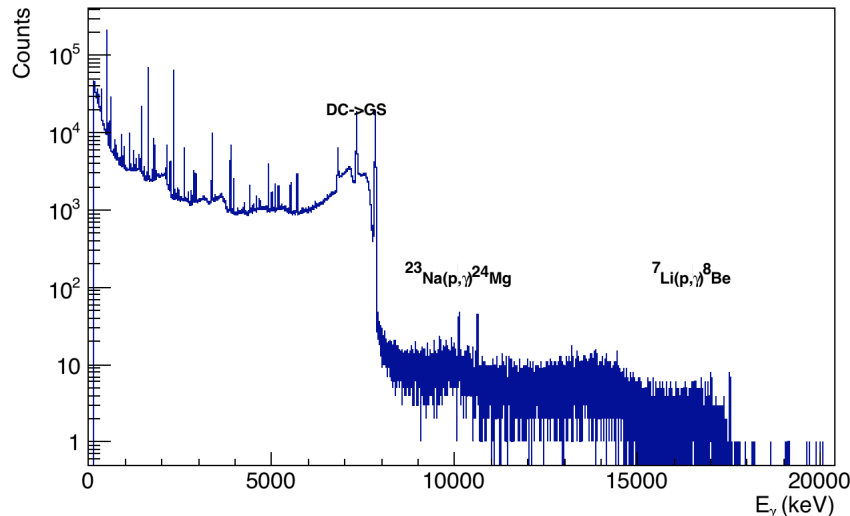


FIGURE 4.17: Gamma spectrum of the $^{13}C(p, \gamma)^{14}N$ reaction at $E_p = 310$ keV. The total charge accumulated is 5.7 C.

Beyond the reference peak at 7843 keV, some peaks are visible. The group at 17500 keV are related to the Direct Capture to the Ground State of $^7Li(p, \gamma)^8Be$ reaction; the group at 10600 keV are emitted by the excitation of the resonance at $E_{R,lab} = 310$ keV of the $^{23}Na(p, \gamma)^{23}Mg$ reaction. Both the contaminants come from traces from the target holder from previous measurements at LUNA400. Both are not influent for the beam induced background of the $^{13}C(\alpha, n)^{16}O$ reaction because cannot open (α, n) channels. For what concerns the Boron contamination, I focused the check on the ^{11}B , the most abundant isotope. Due to its high Q value in the $^{11}B(p, \gamma)^{12}C$ reaction ($Q = 15956$ keV), a peak due to the proton capture at energy 16240 keV should be visible. Another possible combination of gamma is the primary emitted up to the first

excited state at $E_x = 4420$ keV, with an energy of 11820 keV and the secondary gamma emitted of 4420 keV. These γ -rays are not visible, so I can conclude that presence of B in the target can be considered negligible.

The study of gamma spectra from the $^{13}\text{C}(p, \gamma)^{14}\text{N}$ for the study of possible background has been completed with complementary measurements with alpha beam. Possible contaminants for the (α, n) reaction could be present along the beamline (e.g. on the slits or in the copper tube for the cold trap). Many attentions have been paid focusing the beam and monitoring the currents on the slits and on the cold finger, as explained in Section 2.1.1 and prevent to hit the beamline.

Another possibility is that these contaminants can be inside the target itself. We checked presence of impurities in the Ta backings shooting alpha beam on blank supports.

Furthermore we produced evaporated natural carbon targets. The abundance of ^{13}C 1.1%, so the $^{13}\text{C}(\alpha, n)^{16}\text{O}$ yield should be negligible in this case. The $^{12}\text{C}(\alpha, n)^{15}\text{O}$ has a negative Q-value ($Q=-8500$ keV), so this channel cannot be opened. An enhancement in the count rate could be seen as presence of pollutant evaporated on the Ta backing during the evaporation.

The count rate of the spectra acquired have been compared with the natural background.

Spectra normalized by time are shown in Figure 4.18 In Table 4.7 information of long runs have been summarized: neutron detection rates are compatible within the error.

Red, blue and green spectra indicate the neutron spectra of environmental

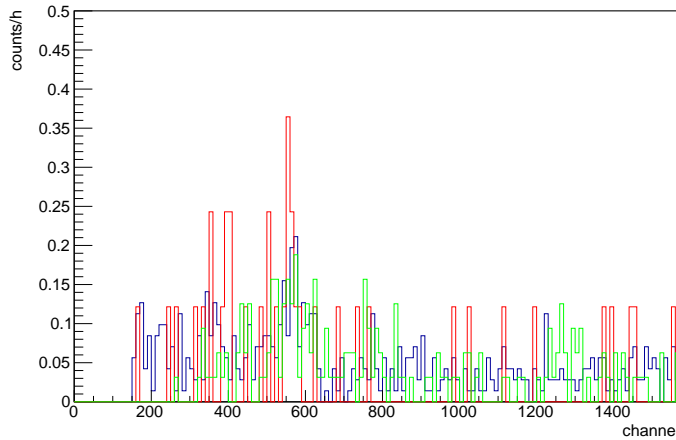


FIGURE 4.18: Spectra acquired for the evaluation of possible Alpha Beam Induced Background: blue, green and red spectra are the natural background, the blank backing and the natural target, respectively.

TABLE 4.7: Quantities measured for the evaluation of possible Alpha Beam Induced Background

target	charge (μC)	time (h)	counts in ROI	count rate
blank	12842105	31.83	83 ± 9	2.61 ± 0.28
natural carbon	3996410	6.54	21 ± 4	3.21 ± 0.611

background, of irradiation on Ta backing and irradiation on evaporated natural carbon target.

4.5 Conclusions after the characterization

All the tests performed by mean of the $^{13}\text{C}(p, \gamma)^{14}\text{N}$ reaction on the enriched target were successful and revealed that the target evaporation have high reproducibility and uniformity on the Ta backing within a level of 5%.

Moreover after the test under a higher intensity proton beam, with an average current of 100 uA, we are confident that they can withstand at a long proton charge irradiation, with a degradation of the order 20% after 33C. An Helium beam irradiation, with a mass that has a factor 4 higher than an Hydrogen beam, can have a much worse effect on the target and in the next chapter I will explain the method I found to face this puzzle.

Thanks to the tail of the resonance at $E_{p,lab} = 551$ keV that still contributes in the energy range of LUNA400, the reaction rate is high enough to collect high counts statistics in the peak of the proton capture with a small amount of charge and causing a negligible degradation.

So the idea, that will be explained in more details in next chapter, it to alternate long alpha runs for the cross section measurements and short proton runs for the target monitoring.

The analysis of the gamma spectra, will permit to interpret the target modification due to the alpha irradiation, and correct data acquired for the cross section measurement.

Chapter 5

Data analysis and results

In this Chapter I will describe the data analysis performed to extract the $^{13}\text{C}(\alpha, n)^{16}\text{O}$ absolute cross section value.

In my PhD work I developed an analysis based on an alternation of proton and alpha beam irradiations on the ^{13}C target.

The analysis procedure is divided in two steps: the first is devoted to analyse the spectra of $^{13}\text{C}(p, \gamma)^{14}\text{N}$ and evaluate the target modifications as a function of the charge by means of a gamma shape analysis (Section 5.1).

In the second step, the target parameters extracted from the previous investigation have been used for the evaluation of cross section of the $^{13}\text{C}(\alpha, n)^{16}\text{O}$ reaction (Section 5.2).

In the last section I will compare my results with previous data in the literature (Section 5.3).

5.1 The gamma shape analysis with $^{13}\text{C}(p, \gamma)^{14}\text{N}$

Here, I will described an innovative method for monitoring of target modifications and the consequent necessary correction of the data during the cross section analysis.

As highlighted in Chapter 4, the tail of the broad resonance at $E_R = 551$ keV ($\Gamma = 23$ keV) of the $^{13}\text{C}(p, \gamma)^{14}\text{N}$ reaction increases the reaction rate in the energy region covered by LUNA, permitting to collect statistics with less than 3% uncertainty in short time.

By means of the $^{13}\text{C}(p, \gamma)^{14}\text{N}$ reaction we have collected information on the status of the target, used then in the $^{13}\text{C}(\alpha, n)^{16}\text{O}$ cross section data analysis. For this reason the working group decided to alternate proton irradiations and alpha ones on the ^{13}C targets.

As I will show, this allows to monitor the target conditions during heavy irradiation and to correct $^{13}\text{C}(\alpha, n)^{16}\text{O}$ yield measured in each partial run for the loss due to degradation.

The strategy of measurement for each ^{13}C target has been summarized in Table 5.1:

The cycle of measurement was typically stopped after four alpha irradiations.

All the proton references runs have been acquired at $E_{p,lab} = 310$ keV. This energy represents a good compromise since, on one side, there is still high counting statistics and on the other side it is far away from possible beam induced background due to the reaction $^{19}\text{F}(p, \alpha\gamma)^{16}\text{O}$ reaction at $E_{p,lab} = 340$ keV.

TABLE 5.1: Scheme of a cycle of measurement for a ^{13}C target

beam	run name
proton	p_ref1
alpha	alpha_1
proton	p_ref2
alpha	alpha_2
proton	p_ref3
...	

In order to correlate the ^{13}C target status between $^{13}\text{C}(\alpha, n)^{16}\text{O}$ and $^{13}\text{C}(p, \gamma)^{14}\text{N}$ measurements, one should take into account the different nuclear process behaviour of the two projectiles inside a carbon target.

In particular, the contribution to the total yield of target nuclei at different depths can be affected by target degradation to a different extent for the two reactions. So I have assumed to divide the thick target in thin slices of thickness dE , corresponding to 1 keV, in which the cross section and stopping power are considered constant.

The yield between E and $E + dE$ is given by:

$$dY(E, E + dE) = \frac{\sigma(E)}{\epsilon_{eff}(E)} dE \quad (5.1)$$

I used formula 5.1 to perform a numerical simulation on the reaction yield as a function of the target depth for $^{13}\text{C}(\alpha, n)^{16}\text{O}$ as well as for $^{13}\text{C}(p, \gamma)^{14}\text{N}$.

$^{13}\text{C}(p, \gamma)^{14}\text{N}$ cross section was calculated, as explained in Chapter 4, as the incoherent sum between the direct capture component, evaluated by King et al.[77], and the high energy tail of the broad resonance at $E_p = 551$ keV [75]. $^{13}\text{C}(\alpha, n)^{16}\text{O}$ cross section was calculated from Heil's R-matrix extrapolation [34].

The stopping power of Helium and Hydrogen projectiles in Carbon in formula 5.1 has been extracted from SRIM2008 [50], assuming pure ^{13}C target stoichiometry.

Figure 5.1 shows the normalization of the $^{13}\text{C}(\alpha, n)^{16}\text{O}$ yield with respect to the yield in the first target slice (blue crosses) and the yield ratio of the $^{13}\text{C}(p, \gamma)^{14}\text{N}$ in green stars.

In Figure 5.1, depth on x-axis is in nanometers, in order to directly compare the depths of the target, since the energy loss is different at the same depth due to different stopping power between alphas and protons projectiles.

The depth in unit of length d as a function of energy loss ΔE of a beam with energy E_b is given by:

$$d = \int_{E_b - \Delta E}^{E_b} \left(\frac{dE}{dx} \right)^{-1} dE \quad (5.2)$$

As one can observe, the yield decreases much faster for the $^{13}\text{C}(\alpha, n)^{16}\text{O}$ reaction than for the $^{13}\text{C}(p, \gamma)^{14}\text{N}$ one. From this consideration it is evident that the target thickness is not a crucial quantity in the cross section analysis, pointing out that the targets modifications in their surface layers is more important.

In Figure 5.2 the comparison of the peak of the $DC \rightarrow GS$ transition of

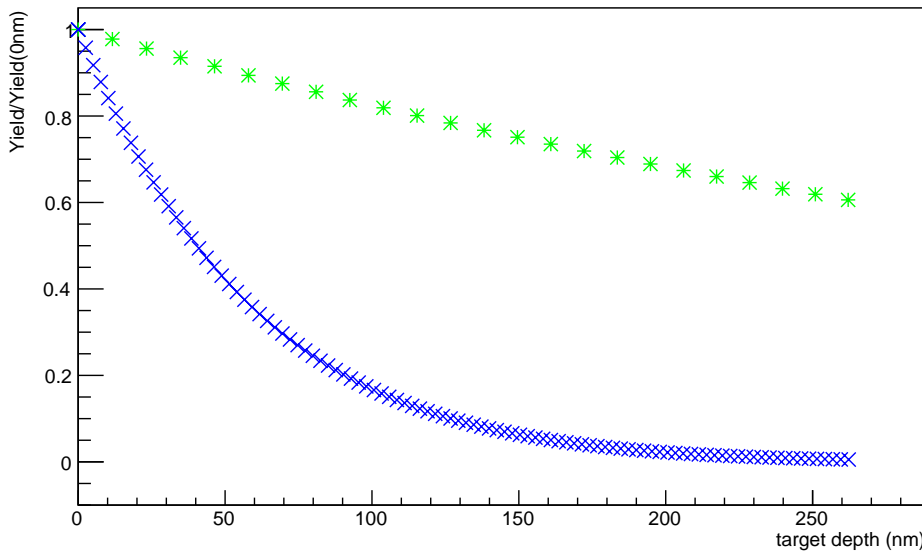


FIGURE 5.1: Reaction yield as a function of the target depth: green stars and blue crosses indicate $^{13}\text{C}(p, \gamma)^{14}\text{N}$ and $^{13}\text{C}(\alpha, n)^{16}\text{O}$, respectively. Depth on x axis is in nm for a direct comparison of the two reaction yields.

$^{13}\text{C}(p, \gamma)^{14}\text{N}$ for four γ -ray spectra acquired on the same target is shown. The blue spectrum has been acquired bombarding the fresh target with a proton beam, while red, green and violet spectra have been acquired after a total charge of 1, 2 and 3 C of alpha.

One can observe that, with increasing alpha charge, the peaks show the reduction of the yield and a slight widening.

This effect can be related to the modification of the target stoichiometry: a change in the ratio between inactive and active nuclei can occur, increasing the second term in formula 4.4.

Based on formula 5.1, an increase of the effective stopping power, $\epsilon_{eff}(E)$, will reduce the reaction yield.

In order to analyse the γ -ray peak, I have introduced a gamma line shape method. I have taken into account that the shape of the primary peak comes from the behaviour of the cross section and from the energy loss of the projectiles in carbon, both changing with beam energy decreasing in the target. The formula 5.1 can be written as:

$$dY(E_\gamma, E_\gamma + dE) \propto \frac{\sigma(E_\gamma)}{\epsilon_{eff}(E_\gamma)} \Sigma(E_\gamma) r_{HPGe}(E_\gamma, \sigma_{HPGe}(E_\gamma)) dE \quad (5.3)$$

where Σ defines the energy particle distribution as a function of target thickness due to the straggling effect and the term $r_{HPGe}(E_\gamma, \sigma_{HPGe}(E_\gamma))$ is the energy resolution of the HPGe detector. In equation 5.3 one can transform

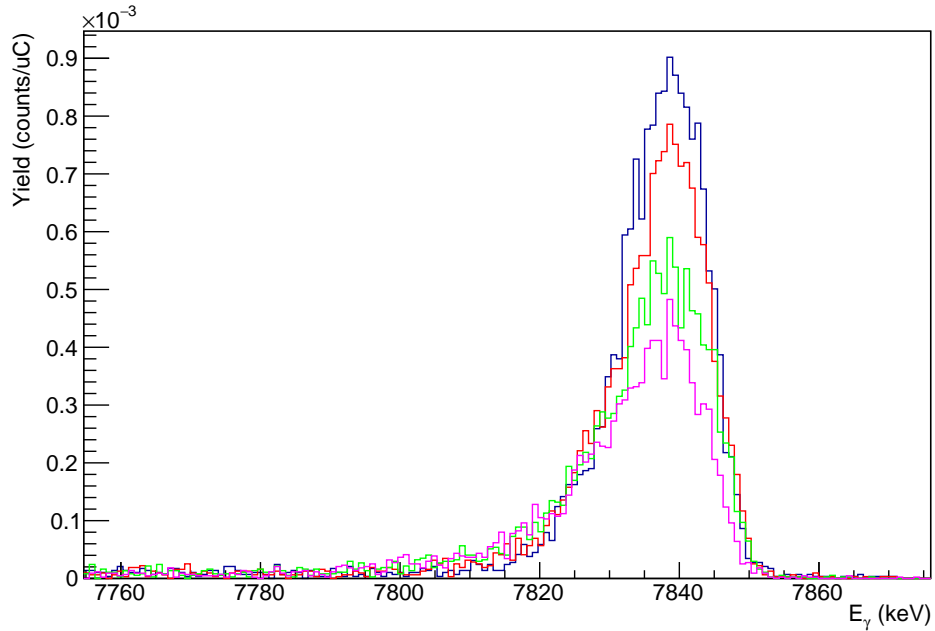


FIGURE 5.2: (Colour online) Comparison $DC \rightarrow GS$ transition in γ -ray spectra acquired on the same target at different accumulated alpha charge: blue, red, green and violet spectra have been acquired on a fresh target and after 1C, 2C and 3C of alpha, respectively. The yield decreased clearly with the increasing of the cumulative charge.

from the γ -ray energy E_γ to the corresponding energy E_p at which the reaction takes place, using the relationship

$$E_p = \frac{1}{\mu}(E_\gamma - Q + \Delta E_{rec} - \Delta E_{Dopp}) \quad (5.4)$$

where μ is the reduct mass of the projectile-target system.
The third term in brackets in equation 5.4 reflects a correction for the recoil energy of the emitting nucleus:

$$\Delta E_{rec} = \frac{E_\gamma^2}{2M_B c^2} \quad (5.5)$$

where M_B is the mass of the compound nucleus (here ^{14}N).
Finally, the Doppler shift of the γ -rays emitted from a nucleus moving at a velocity v affects the observed γ -ray energy:

$$\Delta E_{Dopp} = \frac{v}{c} E_\gamma \cos\theta \quad (5.6)$$

where θ is the angle between the beam direction and the γ -ray detector.

5.1.1 The straggling effect distribution

The energy particle distribution as a function of target thickness due to the straggling effect has been performed with TRIM simulations [50], which provides the energies of particles transmitted beyond a fixed target layer.

The distribution of N particle diffused in thickness d , can be approximated with a Gaussian probability density function (pdf), where the average value comes from the energy loss formula and the FWHM is estimated using the so called Bohr approximation:

$$FWHM(d) = 2\sqrt{2\ln 2} \sqrt{4\pi e^4 Z_p^2 Z_t N d} = 1.20 \cdot 10^{-12} \sqrt{Z_p^2 Z_t N d} \quad (5.7)$$

where Z_p , Z_t , N and d are the atomic number of projectile and target, the target density (in atoms/cm^3) and the depth (in cm) reached by the projectile, respectively. The deepest goes the projectile, the largest is the energy distribution. I run numerical simulations with $N = 10000$ events increasing target thickness from 10 nm up to 300 nm in steps of 10 nm.

An example is shown in Figure 5.3: in the lego plot the diffusion of a proton beam at $E_{p,lab} = 310 as a function of the ^{13}C target depth is reported.$

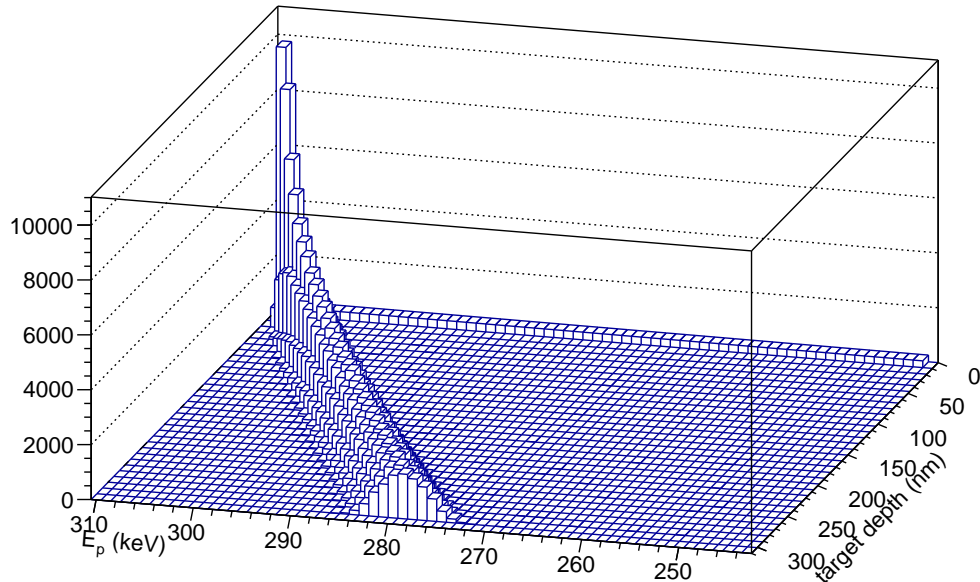


FIGURE 5.3: Straggling effect simulated using SRIM 2008 [50].

I built the probability density function given by the straggling effect summing all the contributions of each layer and normalizing for the overall number of projectiles.

5.1.2 The HPGe energy resolution

In the formula 5.3, the term $r_{HPGe}(E_\gamma, \sigma_{HPGe}(E_\gamma))$, has been extrapolated at higher energies considering the secondary γ -rays emitted at $E_\gamma = 2312, 4915$

and 5619 keV, since the Direct capture peak at $E_\gamma = 7843$ keV cannot be approximated with a gaussian fit.

The three peaks have been fitted with a Gaussian curve plus a linear background: an example of fit is show in Figure 5.4.

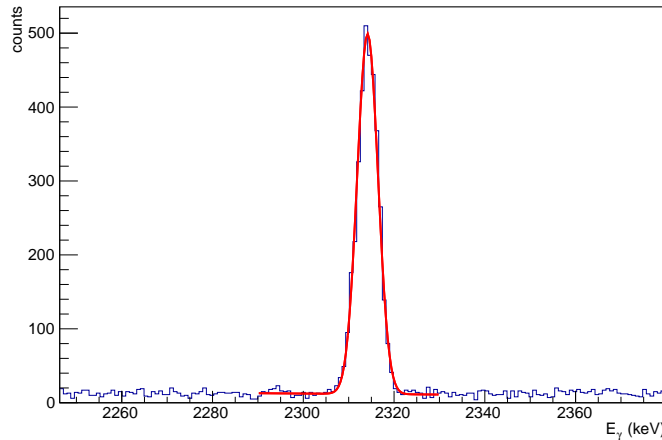


FIGURE 5.4: Example of fit at $E_\gamma = 2312$ keV secondary γ line for the evaluation of the energy resolution

The FWHM¹ of each secondary peak is plotted in Figure 5.5; their values have been also reported in Table 5.2; this procedure has been repeated for three different targets to check the reproducibility.

TABLE 5.2: Full Width Half Maximum fitted for three secondary peaks: in the last column the extrapolation at 7843 keV.

Target	E_γ (keV)	σ_{HPGe} (keV)	σ_{HPGe} at 7843 keV
MT1	2312	2.20 ± 0.033	5.58 ± 1.72
	4915	3.56 ± 0.37	
	5691	5.21 ± 0.72	
MT2	2312	2.2938 ± 0.036	5.55 ± 0.82
	4915	4.05 ± 0.2967	
	5691	4.02 ± 0.5177	
MT10	2312	2.17 ± 0.015	4.59 ± 0.71
	4915	3.509 ± 0.16	
	5619	3.782 ± 0.29	

The FWHM of the resolution depends linearly on the square root of gamma energy, due to the Fano factor [54].

In Figure 5.5, it is evident that error bars for $E_\gamma = 4915$ and 5619 keV are at the level of 10% due to the low statistic acquired: the extrapolation at higher energy cause an uncertainty of the FWHM at $E_\gamma = 7843$ keV around 20%, so in the final analysis I decide to constrain $\sigma_{HPGe}(7843 \text{ keV})$ to vary between 4 and 6 keV.

¹ $\sigma_{HPGe}(E_\gamma)$ is related to the FWHM by means of $\sigma_{HPGe}(E_\gamma) = \text{FWHM}/2.36$

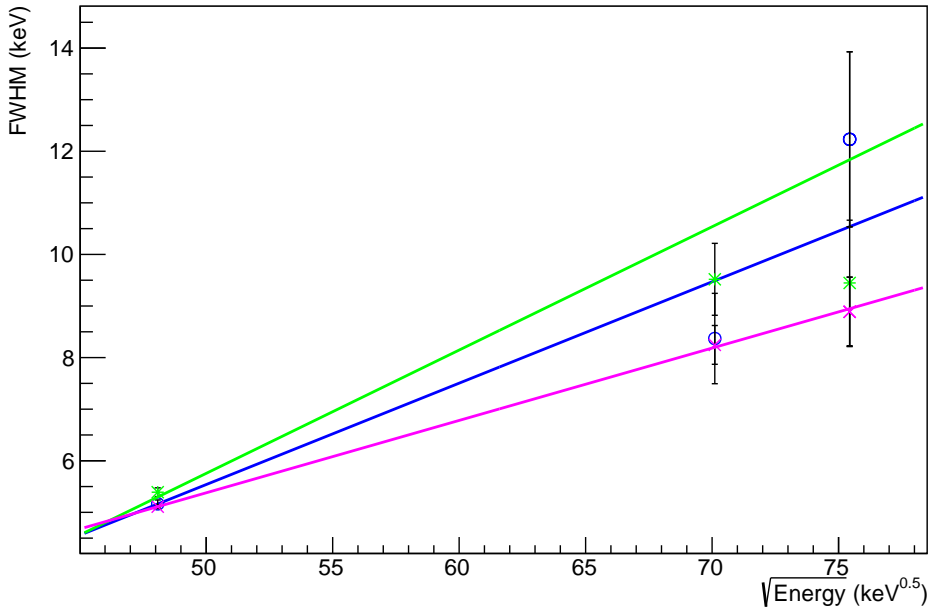


FIGURE 5.5: (Colour online) The three colours represents the curves of different γ -ray spectra emitted by the $^{13}C(p, \gamma)^{14}N$ on three different targets

5.1.3 Analysis on target stoichiometry

The effective stopping power is the crucial quantity in our data analysis. During the cross section measurements, the target composition can change since light elements could be implanted modifying the target stoichiometry. The goal of this analysis is to estimate the modification of the target composition as a function of the cumulative charge Q on target. One can write:

$$\sum \frac{N_i}{N_a} \epsilon_i = k(Q) \quad (5.8)$$

assuming $k(Q)$ as a free parameter in the fitting procedure of the γ -spectrum. The reference run named p_ref1 is always acquired with a fresh target so the contribution to this term is zero.

Then in the following runs, the infinitive yield (formula 5.3) can be parametrized as:

$$dY(E_\gamma, E_\gamma + dE) \propto \frac{\sigma(E_\gamma)}{\epsilon_{^{13}C}(E_\gamma) + k(Q)} \Sigma(E_\gamma) r_{HPGe}(E_\gamma, \sigma_{HPGe}) dE \quad (5.9)$$

The parametrization 5.9 allows to be independent from the type of contaminant nuclei in the target.

I simulated the stopping power of protons propagating in different targets made of pure Hydrogen, Carbon, Oxygen and Tantalum (red cross, black stars, green dots and blue triangles, respectively). The comparison is shown in Figure 5.6.

It is evident that the behaviour of stopping power for all the materials has

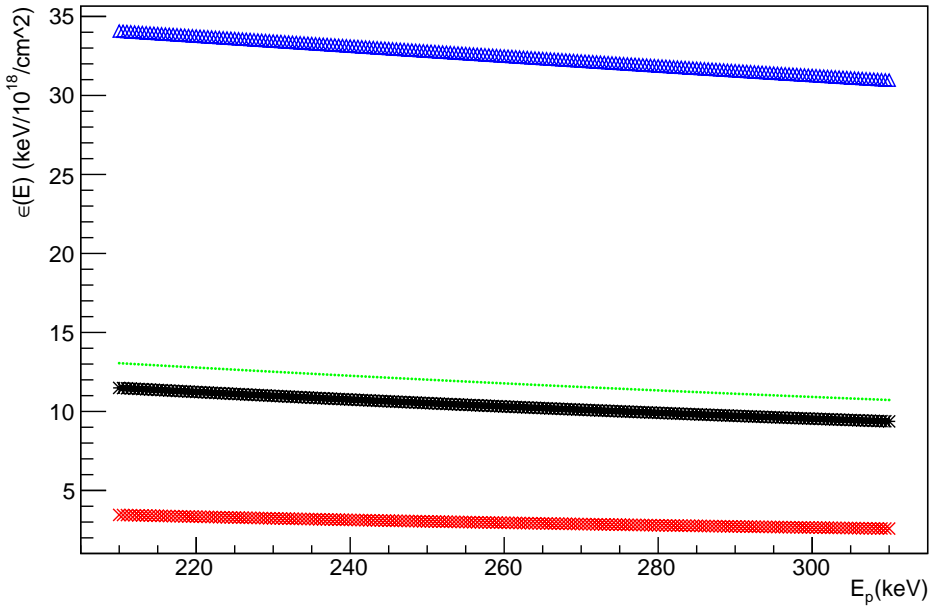


FIGURE 5.6: (Colour online) Comparison of stopping power of proton projectiles in pure materials, Hydrogen, Carbon, Oxygen and Tantalum, indicated by red cross, black stars, green dots and blue triangles respectively. The behaviour of stopping power for all the materials has the same trend as a function of projectile energy.

the same trend as a function of projectile energy.

This means that each curve can be appropriately scaled respect to another to yield the the same contribution in the stopping power.

Fixing a value of $(N_i/N_a)_X$ for the inactive material X , it is always possible to find another value $(N_i/N_a)_Y$ for a different inactive material Y , such as:

$$\left(\frac{N_i}{N_a}\right)_X \epsilon_X(E) = \left(\frac{N_i}{N_a}\right)_Y \epsilon_Y(E) \quad (5.10)$$

so the contribution of the second term in the formula 4.4 is the same, independently from the contaminant in the target.

Based on relation 5.10, I assume, somewhat arbitrarily, Oxygen as inactive nuclei.

A comparison of the behaviour of $(N_i/N_a)\epsilon(E)$ for protons in three different nuclei: Oxygen, Hydrogen and Tantalum is reported in fig 5.7.

Fixing $(N_i/N_a)_O = 0.1$ and scaling the stopping power of the other two nuclei, the condition in equation 5.10 was found with $N_i/N_a = 0.37$ and 0.038 for Hydrogen and Tantalum, respectively.

Figure 5.7 shows the comparison of $N_i/N_a\epsilon(E)_Y$ between Oxygen, Hydrogen and Tantalum.

The comparison among the three trands shows an agreement in the proton energy range used in the analysis within 1%.

I repeated the same numerical simulation for the stopping power of alpha projectiles.

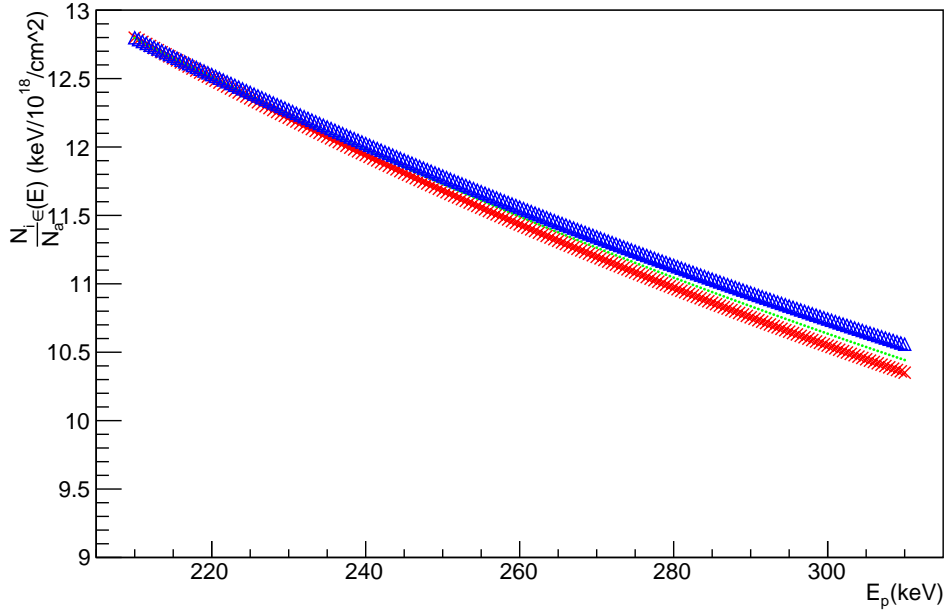


FIGURE 5.7: (Colour online) Inactive contribution to stopping power for different pollutants with appropriate values of N_i/N_a : Hydrogen, Oxygen and Tantalum, are indicated by red cross, green dots and blue triangles respectively. Discrepancy between curves is less than 1%.

Results are shown in Figure 5.8 and 5.9.

Also in this case I assumed $N_i/N_a = 0.1$ for Oxygen as reference inactive contaminant, and I calculated $N_i/N_a = 0.32$ and $N_i/N_a = 0.04$ for Hydrogen and Tantalum, respectively.

Also in the case of alpha particle projectiles the trend of stopping power in the energy region of interest of our measurements is parallel for the different nuclides, so the rescaling procedure can be used also in this case.

This permits us to use the value of $\frac{N_i}{N_a}$ obtained from the $^{13}\text{C}(p, \gamma)^{14}\text{N}$ spectra analysis, in the $^{13}\text{C}(\alpha, n)^{16}\text{O}$ cross section.

Based on Table 5.1, I assumed that the target stoichiometry during each alpha run alpha_i, was the same of target stoichiometry during the previous proton reference run p_refi.

This double numerical simulation gives us the confidence that it is possible to choose an arbitrary inactive contaminant nuclei, \bar{I} .

Combining 5.9 with 5.8 one obtains 5.11.

In this case the yield in a bin of width dE is:

$$dY(E_\gamma, E_\gamma + dE) \propto \frac{\sigma(E_\gamma)}{\epsilon_{^{13}\text{C}}(E_\gamma) + \frac{N_I}{N_a}(Q)\epsilon_{\bar{I}}(E_\gamma)} \Sigma(E_\gamma(E_p)) r_{HPGe}(E_\gamma, \sigma_{HPGe}) dE \quad (5.11)$$

Applying the 5.11 in the fitting procedure I obtain the gamma shape fit shown in Figure 5.10.

In the first reference run, p_ref1, I assumed $N_i/N_a = 0$ and three free parameters:

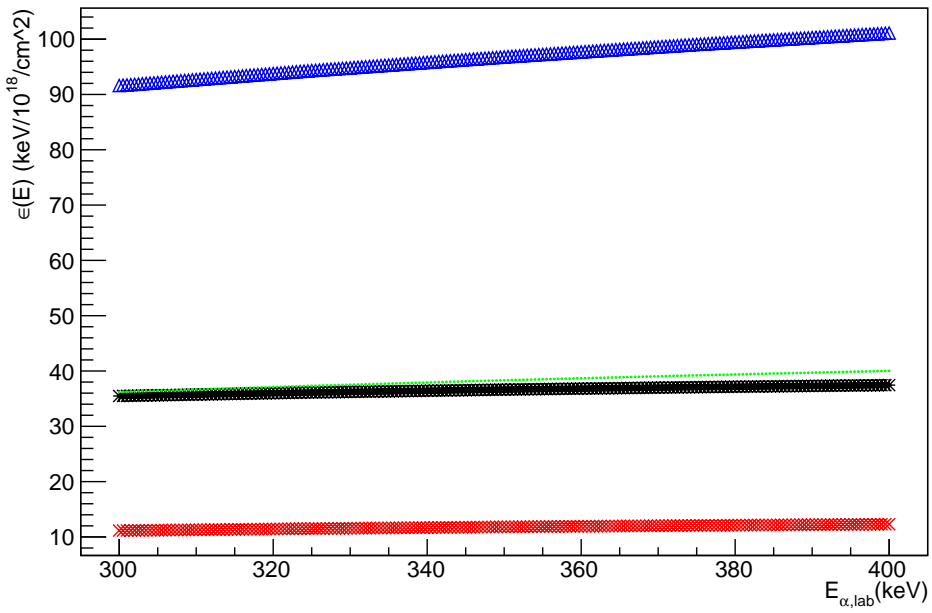


FIGURE 5.8: (Colour online) Comparison of stopping power of alpha projectiles in pure materials, Hydrogen, Carbon, Oxygen and Tantalum, indicated by red cross, black stars, green dots and blue triangles respectively. The behaviour of stopping power for all the materials has the same trend as a function of projectile energy.

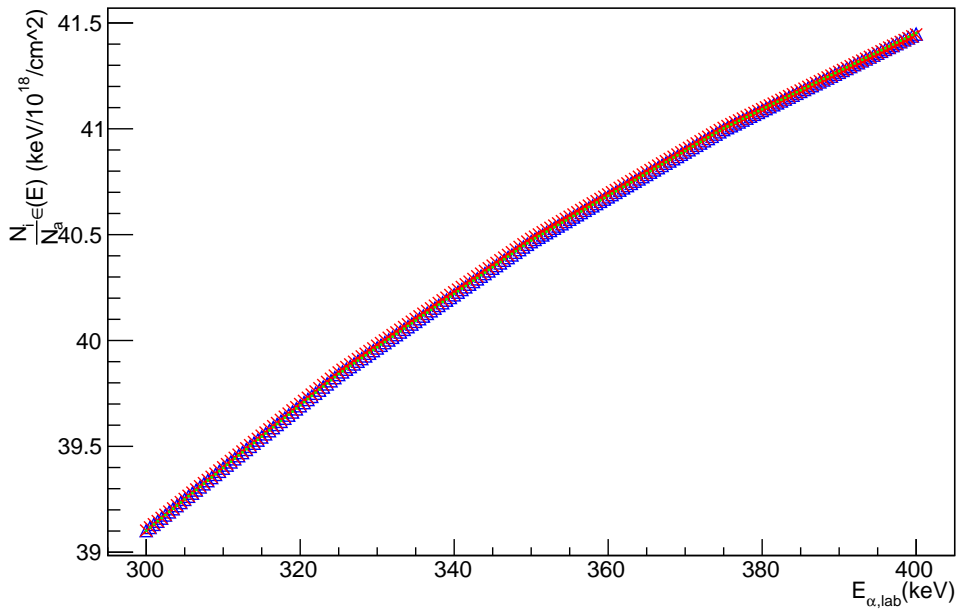


FIGURE 5.9: (Colour online) Inactive contribution to the stopping power for alpha particles in different pollutants with appropriate values of N_i/N_a : Hydrogen, Oxygen and Tantalum, are indicated by red cross, green dots and blue triangles respectively. Discrepancy between curves is less than 1%.

- a normalization constant k
- the FWHM of the energy resolution at 7843 keV, confined between 4 and 6 keV from the analysis described
- the target thickness ΔE that can be extracted from the implementation of the straggling distribution that improves the fitting of the peak falling edge

This fitting procedure has been applied for all the targets used for the cross section analysis.

In the γ -ray spectra acquired after the p_ref1 (the target cycle is in Table 5.1), the three parameters above have been constrained with the values obtained during the fitting procedure of ref1, while N_i/N_a is let as a free parameter.

I point out that the low energy edge of the gamma shape fit, in Figure 5.10,

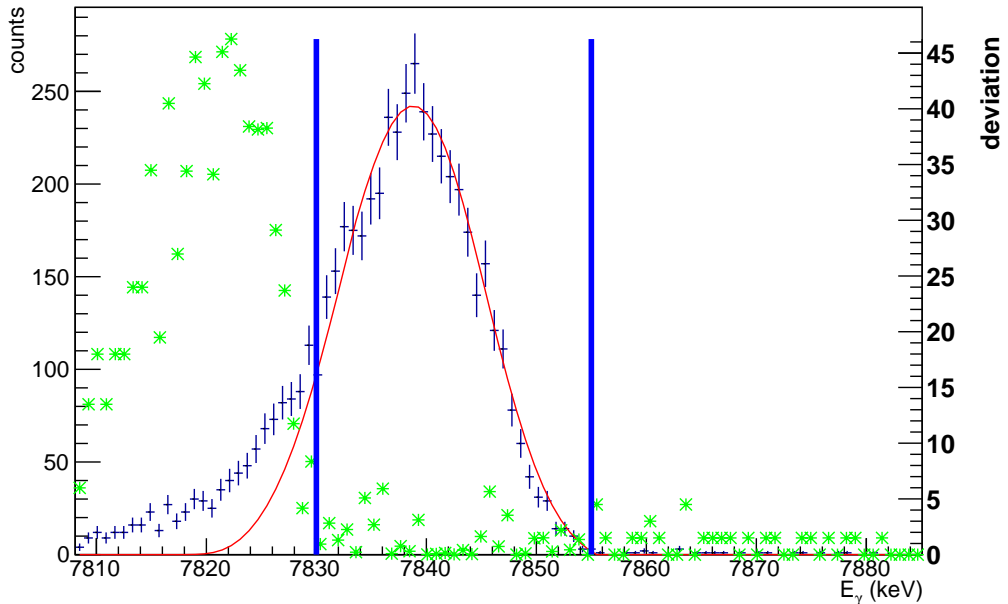


FIGURE 5.10: (Colour online): the red curve is the gamma shape fit on the experimental spectrum. The fit was performed in the region delimited by the two blue bars. Green stars represent the deviation between fit and data (right Y axis).

is excluded from the fitting procedure due to a possible background contribution not yet identified.

However, this cut does not effect the cross section analysis because, as highlighted, $^{13}\text{C}(\alpha, n)^{16}\text{O}$ yield in negligible in the deepest layers of the target with respect to the target surface.

In Figure 5.10, green stars indicate the fit discrepancy with the experimental data: relative values are on the secondary Y axis.

In Figure 5.11, N_i/N_a values are plotted as a function of the cumulative charge for three different target analysed (each colour represents a target). The circles are the values fitted during the γ -rays spectra analysis, the triangles are the extrapolated values of the stoichiometry ratio used in the neutron

analysis.

Due to the fact that the behaviour for each target is different, I will evaluate the degradation of each target separately, avoiding to add possible systematic uncertainties.

The uncertainty on the stoichiometric ratio N_i/N_a at 1σ has been determined calculating the extremes of the interval $[N_i/N_a - \sigma, N_i/N_a + \sigma]$ in the least square applying the condition $\chi^2 = \chi^2_{min} + 1$, as shown in Figure 5.12.

The uncertainty $\delta_{Ni/Na}/(Ni/Na)$ related to the contamination relative to

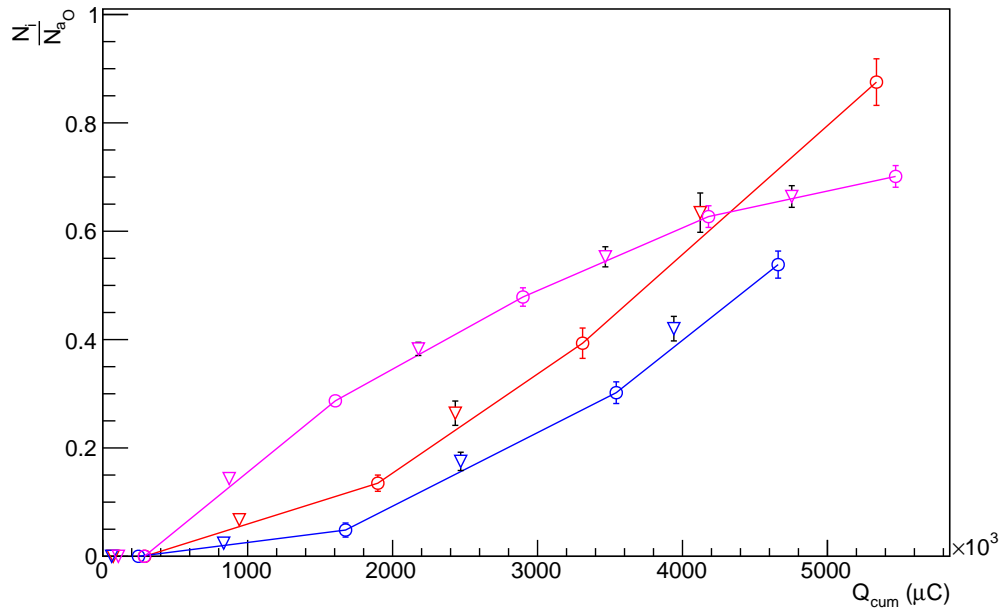


FIGURE 5.11: (Colour online) The stoichiometric ratio $(N_i/N_a)_O$ is plotted as a function of cumulative charge Q_{cum} on three different targets, represented by different colours. Uncertainties are evaluated in the least square method with the condition $\chi^2 = \chi^2_{min} + 1$.

the Oxygen nucleus is in the range $6\% < \delta_{Ni/Na}/(Ni/Na) < 10\%$. All values evaluated with the fitting procedure are listed in Appendix A. One example is in Table 5.3.

TABLE 5.3: Fit parameters for a target (T12). In the right part of the table there are the parameters fit with the proton run analysis; on the left part there are the extrapolated stoichiometric ratio used during the alpha run analysis.

	proton run								alpha run			
	run	σ_{HPGe}	$\Delta x(nm)$	$k(a.u)$	χ^2_{red}	Qpart	Qcum	Ni/Na	$\delta(Ni/Na)$	Q_{av}	Ni/Na_{av}	$\delta(Ni/Na)_{av}$
T12	T12_ref1	3.671	182.023	0.0359	1.81	289409	289409	0	0	72352.25	0	
	T12_ref2	3.848	181.417	0.042	1.74	316837	1898246	0.048	0.013	942266	0.024	0.010
	T12_ref3	4.23	180.000	0.037	1.81	371293	3310837	0.302	0.02	2432509	0.175	0.017
	T12_ref4	4.757	181.417	0.0437	2.48	437066	5338284	0.538	0.025	4122470.75	0.420	0.022

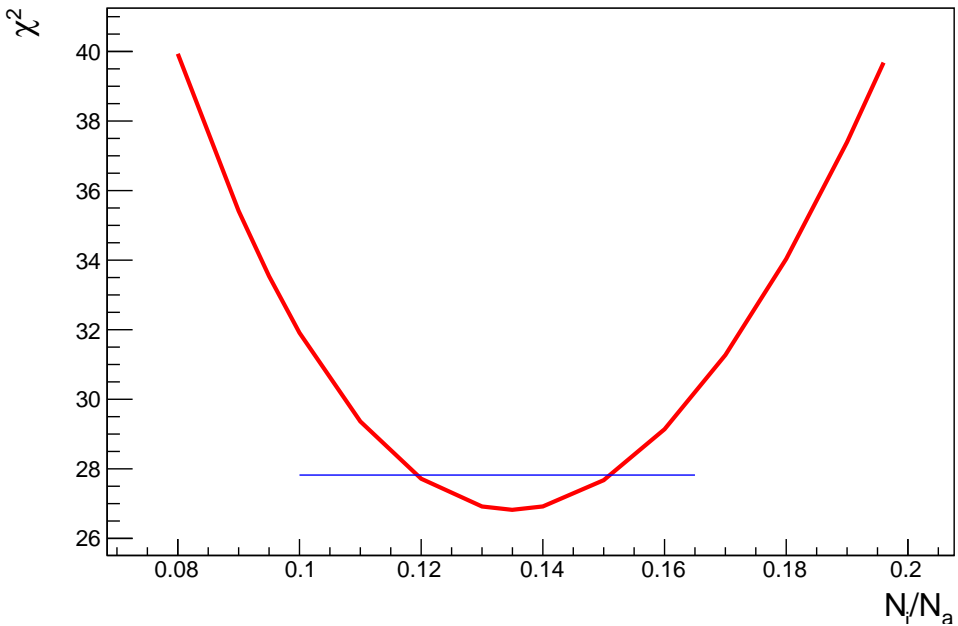


FIGURE 5.12: (Colour online): the red quadratic curve indicates the χ^2 value as a function of the free parameter value; the blue line indicates the level of the the $\chi^2_{min} + 1$. The two points where the two curve intercept indicate the uncertainty interval at 1σ .

5.2 $^{13}\text{C}(\alpha, n)^{16}\text{O}$ cross section at low energy

In my PhD work, the $^{13}\text{C}(\alpha, n)^{16}\text{O}$ absolute cross section measurement has been performed in the energy range $275 < E < 305$ keV.

Thanks to low background environment and the intense beam delivered by the LUNA accelerator, we have been able to measured for the first time below the lowest point in literature measured by Drotleff.[2] at $E= 280$ keV.

The two experimental setups used have been described in Chapter 3.

Using ^3He counters embedded in a polyethylene moderator as detectors, we lose the possibility to reconstruct the energy spectrum.

The experimental quantity measured is the integral neutron yield Y_n , written as in formula 5.12:

$$Y_n = \frac{N_n}{Q} = \int_{E_{\alpha,beam} - \Delta E}^{E_{\alpha,beam}} \eta(E_n) \frac{\sigma(E_\alpha)}{\epsilon_{eff}(E_\alpha)} \Sigma(E_\alpha) dE \quad (5.12)$$

where N_n is the net number of neutrons detected after a target irradiation with charge Q .

The effective stopping power $\epsilon_{eff}(E_\alpha) = \epsilon_C(E_\alpha) + \frac{N_i}{N_a} \epsilon_O(E_\alpha)$ is dependent on the stoichiometric ratio extrapolated from the gamma shape analysis fitting procedure, explained in previous section.

$\Sigma(E_\alpha)$ is the alpha energy distribution diffused in the target due to straggling effect.

I repeated the numerical simulation using TRIM increasing the target layers' thickness from 10 up to 300 nm in steps of 3 nm.

I summed all the contribution from each layer and I built the probability density function of energy of the alpha particles, shown in Figure 5.13: the pdf is smeared out only in the last layers of the target, where the reaction contribution is negligible. In the shallow layers, the probability density function is flat and contributes at the same level in the target, so it can be neglected.

$\eta(E_n)$ is the setup efficiency, evaluated by means of Geant4 simulations validated using the $^{51}V(p,n)^{51}Cr$ reaction in Chapter 3. Functions 3.7 and 3.8 parametrize the efficiency curves of the two setup used during the measurements.

In the alpha energy range $360 < E_{\alpha,lab} < 400$, I assumed an average neutron energy of 2.5 MeV, corresponding to setup efficiency of 34.1% and 31.4% for Single target and Multi target setup, respectively.

$\sigma(E_\alpha)$ is the cross section to be measured. In first approximation I used the

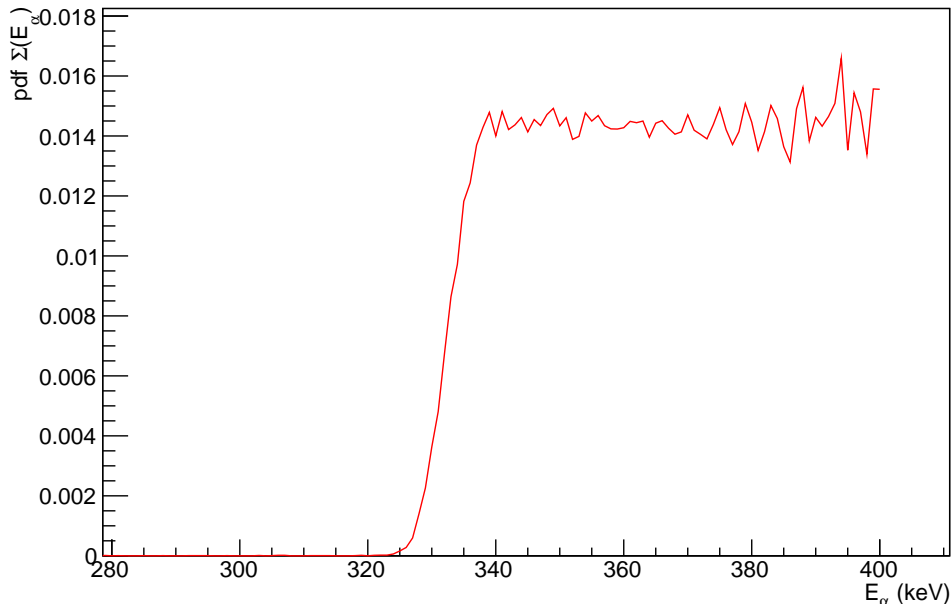


FIGURE 5.13: Probability density function of alpha energy due to straggling effect: it is smeared out only in the last layers of the target

behaviour of the cross section estimated by Heil $\sigma_{Heil}(E_\alpha)$. For the analysis of a run with beam energy E_{α^*} , I will write the cross section term as in formula 5.13:

$$\sigma(E_\alpha) = \sigma_0(E_{\alpha^*}) \frac{\sigma_{Heil}(E_\alpha)}{\sigma_{Heil}(E_{\alpha^*})} \quad (5.13)$$

where $\sigma_0(E_{\alpha^*})$ is the value of the $^{13}C(\alpha, n)^{16}O$ cross section at energy E_{α^*} extrapolated from the data acquired.

This procedure allows the cross section to be determined at the value of the beam energy within the accelerator machine precision, without necessity to introduce the effective energy [78].

Substituting the 5.13 in 5.12 one obtains

$$Y_n(E_\alpha*) = \frac{N_n}{Q} = \sigma_0(E_\alpha*) \int_{E_\alpha* - \Delta E}^{E_\alpha*} \eta(E_n) \frac{\sigma_{Heil}(E_\alpha)}{\epsilon_{eff}(E_\alpha)} dE \quad (5.14)$$

Refering to equation 5.12, the reaction yield at $E_{\alpha,lab} = 400, 380$ and 360 keV is compared: in Figure 5.14 they are represented by red, green and blue spectra, respectively.

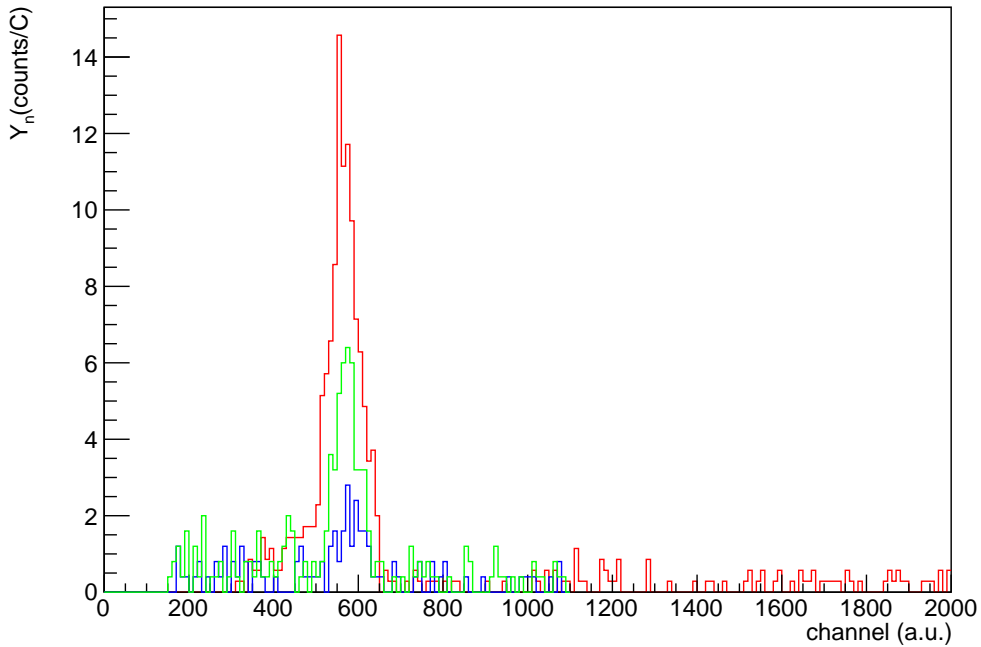


FIGURE 5.14: (colours online) Comparison of sum spectra per unit of charge for three different energies: red, green and blue spectra indicate yield at beam energy of 400, 380 and 360 keV, respectively.

The background of 3.3 counts per hour in the region of interest between channels 200 and 700 (Section 3.3.3) has been subtracted to each raw spectrum. In Table 5.4 are listed the main quantities measured at each incident energy, together with the number of targets used to reach at least a statistical uncertainty lower than 10%.

In the Plot in Figure 5.15 all the measurement referring to $E_\alpha = 400$ keV are shown.

Different colours and symbols represent irradiations on different targets: on X axis there is the numbering of alpha run. The error bars indicates only statistical uncertainty.

The cross section value $\bar{\sigma}$ and the overall uncertainty $\delta_{\bar{\sigma}}^2$ have been estimated with the weighted average on n measurements with value σ_i and uncertainty

TABLE 5.4: Summary of measurements performed in the first campaign: the charge Q_{tot} accumulated and the number of net counts N_n have been used to evaluate the reaction yield

E_{α} (keV)	E_{cm} (keV)	targets used	Setup used	Q_{tot} (C)	N_n
400	275.29	5	MT	14.3	1990
390	298.23	5	MT	16.8	1137
380	290.59	6	MT	17	736
370	282.94	6	ST	13.7	438
360	275.29	9	MT	20.4	394
340	260	4	ST	15.2	63

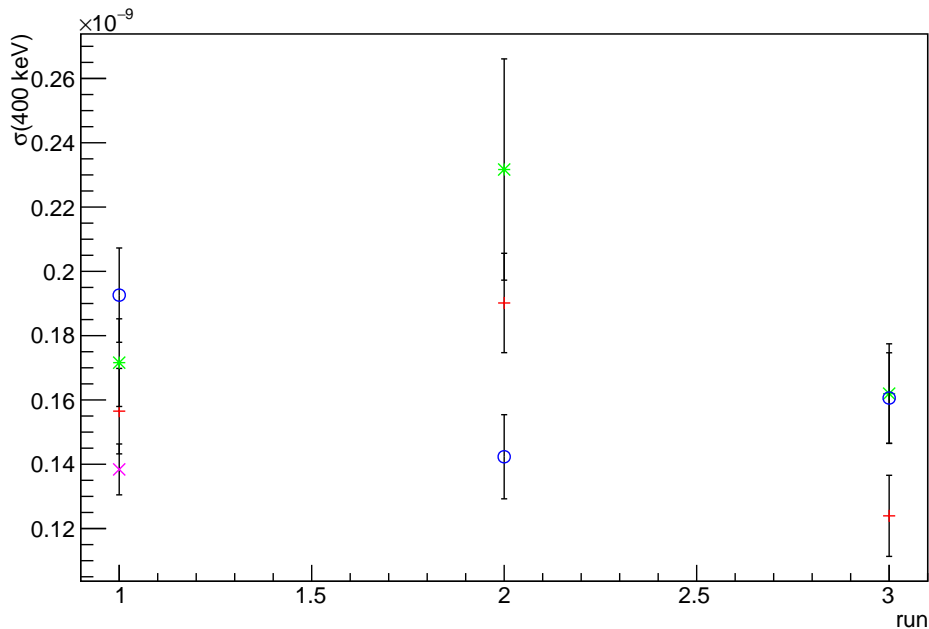


FIGURE 5.15: (Colour online) Cross section evaluation for different targets (each target is represented by one colour): on x-axis the alpha run relative to the measurement.

δ_i :

$$\bar{\sigma} = \frac{\sum_{i=1}^n \frac{\sigma_i}{\delta_i^2}}{\sum_{i=1}^n \frac{1}{\delta_i^2}} \quad \delta_{\bar{\sigma}}^2 = \frac{1}{\sum_{i=1}^n \frac{1}{\delta_i^2}} \quad (5.15)$$

5.2.1 Calculation for different contaminants

In order to be confident in my analysis, I verified if the choice of a particular contaminant for the degradation evaluation could introduce systematic uncertainties. The investigation was performed on a target irradiated with energy beam $E_{\alpha} = 400$ keV: this target had three alpha irradiations interspersed with four reference proton runs.

The inactive nuclide has been changed with one lighter and one heavier than

Oxygen: I choose Hydrogen and Tantalum, respectively.

Figure 5.16 shows the degradation curve for the three contaminant nuclei: red, green and blue curves represent the equivalent pollution of the target considering Tantalum, Oxygen and Hydrogen, respectively.

Error bars are at the level of 5%, the average uncertainty coming from the evaluation of N_i / N_a from the fit.

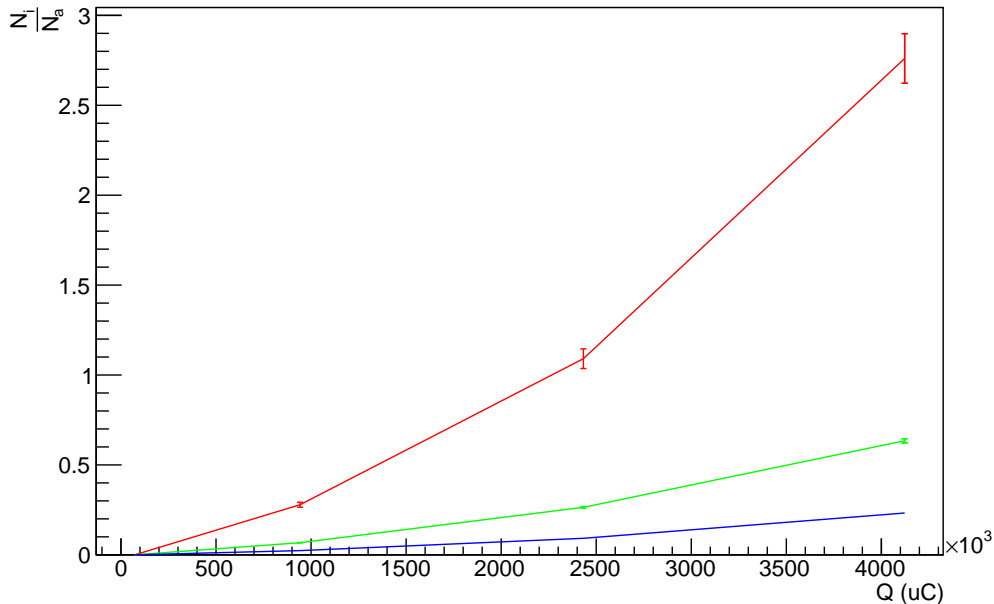


FIGURE 5.16: (Colour online) Diagram of degradation evaluation for the same target assuming different contaminants: red, green and blue curves show the equivalent pollution of a carbon target with Hydrogen, Oxygen and Tantalum, respectively.

The lighter is the inactive nuclei element, the steeper is the curve. This is due mainly to the fact that the stopping power in light elements is lower.

In order to have the same effect in the stopping power formula, to a lower stopping power should correspond an higher value of N_i / N_a .

The correction was included in the analysis for the cross section evaluation.

The three cross section points evaluated during each alpha run are compared per each possible contaminant. Results are shown in Figure 5.17: error bars of points include only statistical uncertainty.

We can observe that all the points in different runs have the same values within uncertainties. In Table 5.5 the cross section value obtained using the formulas 5.15.

I can conclude that the arbitrary choice of the type of contaminant nuclei does not add any systematic uncertainty in the cross section estimation.

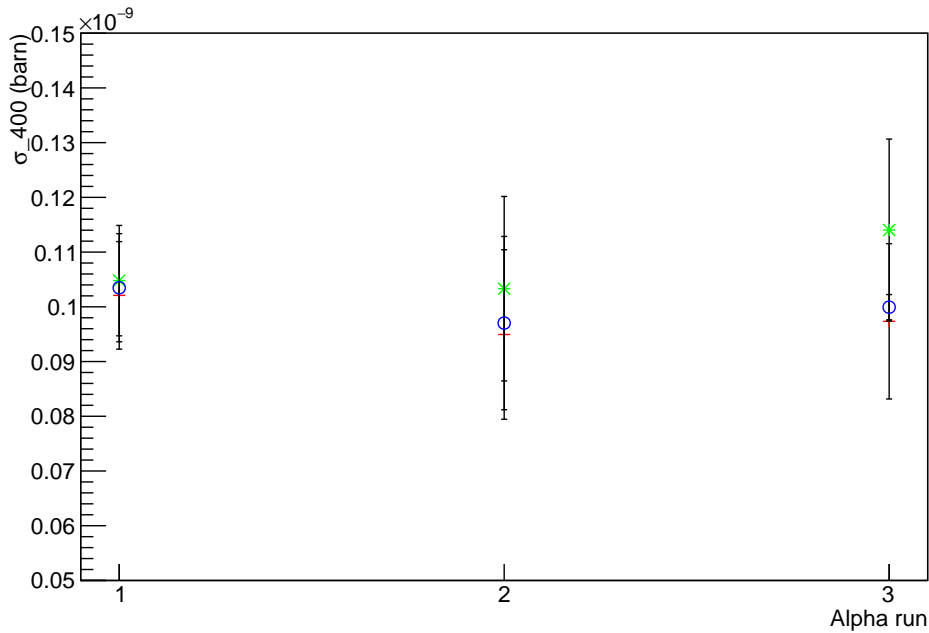


FIGURE 5.17: (Colour online) Cross section evaluation three alpha run of the same target MT2 assuming different contaminant during the evaluation: red, green and blue points represent points evaluated with Hydrogen, Oxygen and Tantalum, respectively. For all the runs cross section values correspond within uncertainty.

TABLE 5.5: Cross section evaluated considering different possible inactive nuclei in the analysis. Values agree within the uncertainties.

Inactive nuclide	σ (barn)	δ (barn)
Oxygen	1.002E-10	2.22E-12
Hydrogen	1.062E-10	7.68E-12
Tantalum	0.996E-10	7.16E-12

5.3 Results and uncertainties

Considering the analysis approach described in the previous section, the $^{13}\text{C}(\alpha, n)^{16}\text{O}$ reaction cross section was measured at six different energies $360 < E_{\alpha, \text{lab}} < 400$ keV, in 10 keV plus the point at $E_{\alpha, \text{lab}} = 340$ keV.

The cross section values are listed in Table 5.6 with their statistical and systematic uncertainties.

All the measurements have been performed to get statistical uncertainties lower than 10%, including the propagation of the background subtraction to the raw counts.

More crucial is the control of systematic uncertainties, main contributions come from:

- the integration of the charge on the target at 3%
- the stopping power from SRIM compilation at 6%

- the target degradation uncertainty on the value N_i/N_a between 6% and 10%
- the efficiency measurement at 5%

TABLE 5.6: Experimental cross section

$E_{\alpha,lab}$ (keV)	E	$\sigma(E)(10^{-11} \text{ barn})(\pm \text{stat} \pm \text{syst})$
400	305.88	$14.70 \pm 0.39 \pm 1.47$
390	298.23	$8.94 \pm 0.32 \pm 0.89$
380	290.59	$5.03 \pm 0.19 \pm 0.50$
370	282.94	$3.43 \pm 0.14 \pm 0.34$
360	275.29	$2.10 \pm 0.13 \pm 0.21$
340	260.00	$0.72 \pm 0.10 \pm 0.07$

Our analysis approach give us a robust ground to assume that the effective energy associated to the S(E)-factor, can be associated at the alpha beam at which the cross section measurements have been performed.

Thanks to the accurate energy resolution and the long term machine stability provided by the LUNA accelerator, the beam energy propagation uncertainty is less than 1%, so negligible with respect other uncertainty sources.

The S(E)-factor data are reported in Table 5.7.

TABLE 5.7: Experimental S(E)-factor of $^{13}\text{C}(\alpha, n)^{16}\text{O}$

E (keV)	S(E)-factor (10^5 MeV b) ($\pm \text{stat} \pm \text{syst}$)
305.88	$9.233 \pm 0.243 \pm 0.923$
298.23	$8.833 \pm 0.319 \pm 0.883$
380.59	$7.961 \pm 0.308 \pm 0.796$
282.94	$8.856 \pm 0.375 \pm 0.941$
275.29	$9.052 \pm 0.545 \pm 0.905$
260	$9.258 \pm 1.606 \pm 0.926$

The comparison between previous direct measurements and our S(E)-factor values is shown in Figure 5.18, where blue circles, green stars and red triangles indicate the experimental points measured in the present work, the Drotleff's and the Heil's data, respectively. The red curve is the R-matrix fit performed by Heil [34].

In Figure 5.18, one can observe that in this PhD work we measured the cross section at an unprecedented lower energy point, 20 keV down the lower energy point measured by Drotleff.

I would like also to point out that almost all the cross section measurements have an overall uncertainty of the 10% as the prefixed goal. Special attention reserves the lowest cross section points at 360 and 340 keV, which have an overall uncertainty of 14% and 17%, respectively, due to the poor statistic acquired.

In Figure 5.19, the overall relative uncertainty, per each point in the three datasets, is compared: blue circles, green stars and red triangles, corresponding to the experimental points measured in this PhD work, Drotleff's and by

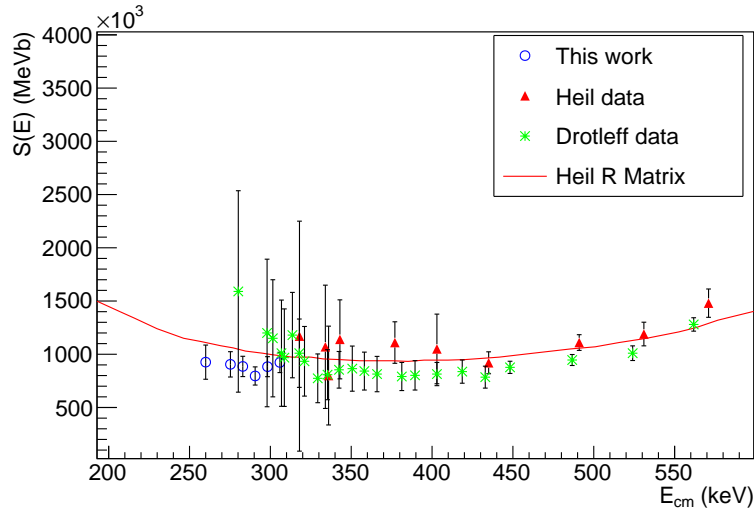


FIGURE 5.18: (Colour online) Comparison of the present LUNA $S(E)$ -factor (blue circles) with the previous data in literature: green stars and red triangles indicate the experimental point measured by Drotleff [2] and by Heil, respectively. The red curve is the R Matrix by Heil [34].

Heil, respectively.

The unbelievable reduction of the overall uncertainties in the present work can be mainly addressed to two reasons: the background reduction in LNGS that causes an important improvement in the statistical uncertainty together with an accurate monitoring of the target behaviour that didn't add other systematic errors.

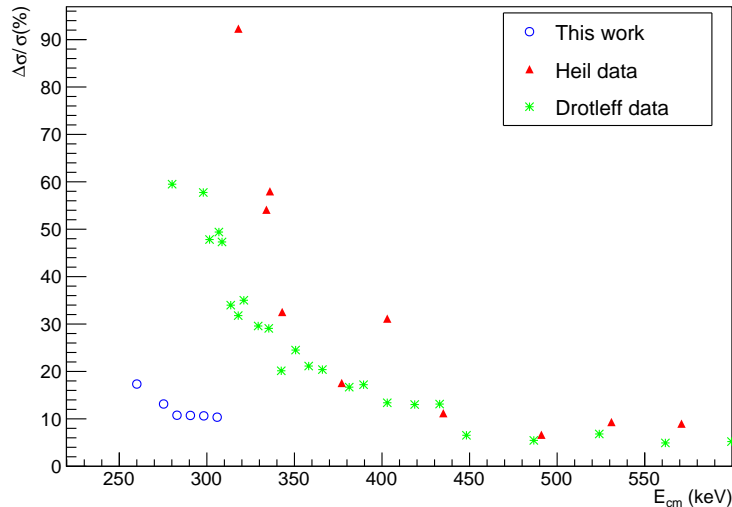


FIGURE 5.19: (Colour online) Overall relative uncertainty corresponding to each data point of three different datasets: blue circles, green stars and red triangles indicate the experimental points measured in this PhD work, in Drotleff [2] and in Heil [34], respectively.

In order to have a simultaneous fit of a calculated R-matrix function for different data sets including the present data, one needs to have a clear separation among statistical and systematic uncertainties budget, as it was debated in Shürmann et al's paper [79]. Unfortunately the literature data for the $^{13}\text{C}(\alpha, n)^{16}\text{O}$ reaction are poor in information except the Heil's dataset. Anyway, I used the open source Azure2 [80] code to perform a very preliminary fit.

I used three different data sets: the point at low energy from this work, Heil et al.'s points and Drotleff et al's ones that cover an high energy range up to 1 MeV. I decided to not use Harissopoulos et al.'s data because of the underestimation of the uncertainties due to a partial calibration validation of the simulation (See chapter 1).

I included six energy resonances as input parameters in the Azure code : $E_1 = 6.356 \text{ MeV } J^\pi = 1/2^+$, $E_2 = 7.165 \text{ MeV } J^\pi = 5/2^-$, $E_3 = 7.202 \text{ MeV } J^\pi = 3/2^+$, $E_4 = 7.379 \text{ MeV } J^\pi = 5/2^+$, $E_5 = 7.382 \text{ MeV } J^\pi = 5/2^-$ and $E_6 = 7.447 \text{ MeV } J^\pi = 3/2^-$, with the corresponding background poles with the same J^π , set at energy of 30 MeV.

The channel radius values are the same used for Heil's fit: 4.0 and 5.2 fm for the $^{16}\text{O} + n$ channel and for the $^{13}\text{C} + \alpha$ channel, respectively.

The preliminary S(E)-factor fit is shown in Figure 5.20.

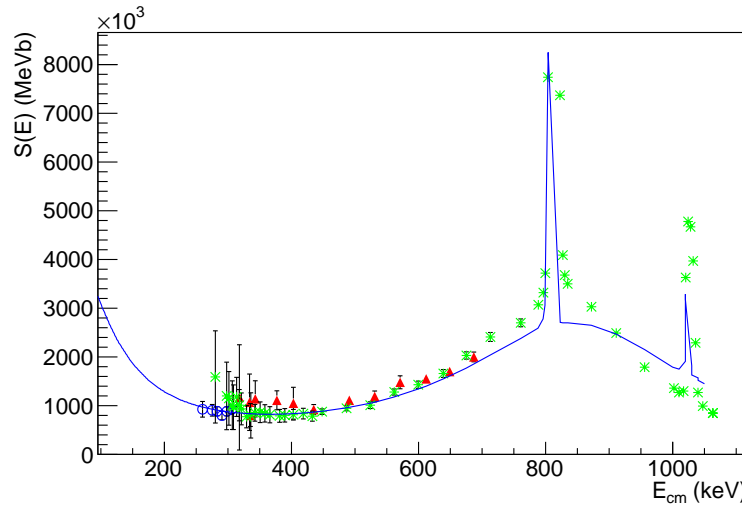


FIGURE 5.20: (Colour online) Three data sets, blue circles from this work, green stars from Drotleff and red triangles from Heil. The blue line is preliminary fit. For details see the text.

Even if the goal of my PhD work it is not to perform a global R-matrix fit, however one can point out that an open issue exists in the high energy range. This could be the consequence of the need to quantify and keep under control the systematic uncertainties also for high energy data points.

Conclusions

In my thesis work I have presented results of the new measurement of the absolute cross section of the $^{13}\text{C}(\alpha, n)^{16}\text{O}$ reaction ($Q=2.215 \text{ MeV}$), the main neutron source for s process in low mass AGB stars. The environmental temperature is around 10^8 K , that is translate in a Gamow window $140 < E < 230 \text{ keV}$, well below the Coulombian barrier. Before this PhD work, the state of the art presented measurements in the energy range $280 < E < 8000 \text{ keV}$. In particular, measurements in the low energy region are affected by uncertainties larger than 50%. The main experimental problems are due to a low reaction rate with the decreasing of energy that is hidden by the an environmental background of the cosmic neutron background and fission in materials used for the setup design. Another problem is the difficulty to check the target modification under an alpha beam (build up effect, degradation, contamination).

The extrapolation of high energy data is a tricky process due to the presence of a near threshold resonance at $E_x = (-3 \pm 8) \text{ keV}$ of the ^{17}O compound nucleus that contribute to the $^{13}\text{C}(\alpha, n)^{16}\text{O}$ cross section in the Gamow window. Complementary indirect measurements, as the Trojan Horse Method or the ANC calculation, allow to avoid the experimental problems of the repulsion of the Coulomb barrier and the screening effect, that in the case of this reaction is negligible, but a normalization with respect to direct experimental data is needed. For all this reasons a direct measurement approaching the Gamow window with an overall uncertainty around 10% is crucial.

In the LUNA (Laboratory for Underground Nuclear Astrophysics) collaboration framework, I had the unique opportunity to perform the $^{13}\text{C}(\alpha, n)^{16}\text{O}$ reaction cross section measurement taking advantage of a low environmental background thanks to the natural shielding of 3400 meters water equivalent that suppresses the neutron cosmic background by three orders of magnitude and the high intense alpha beam ($\langle I \rangle = 200 \mu\text{A}$) provided by the LUNA 400 accelerator with an excellent energy resolution (100 eV).

Moreover ^3He counters with a stainless steel case have been used for the measurements. This permitted to reduce the alpha intrinsic background of the detector, coming from uranium and thorium impurities in the case, by one order of magnitude with respect normal aluminium case counters.

The overall background estimated in the region of interest is at the level of $3.34 \pm 0.11 \text{ counts/h}$, with the possibility to perform a measurement with an excellent signal to noise ratio down to low energies. A direct measurement of the $^{13}\text{C}(\alpha, n)^{16}\text{O}$ reaction in an energy window $340 < E_{lab} < 400 \text{ keV}$, has been performed. The final detector placement was chosen after a long simulation campaign performed with a devoted tool based on the Geant4 code. 18 ^3He counters have been set in two concentric rings around the target chamber: 6 counters with 25 cm active length and 12 counters with 40 cm of active

length are embedded in a polyethylene moderator at 6 and 11 cm from the target, respectively.

Two setup have been designed : the Multi Target (MT) chamber and the Single Target Chamber. The MT setup, where it is possible to mount three targets per time, was used in the first part of the measurement. With this setup we had the possibility to change the irradiated target without breaking the vacuum and preserving the chamber experimental condition. This has been fundamental for a precise and detailed target characterization with as low as possible systematic uncertainties. The ST setup was mounted in the mounted later because it has a smaller target chamber and a larger efficiency in our energy region of interest, that is crucial to approach the Gamow window going down in energy. For both the setups, special efforts were made to calibrate the corresponding efficiency curve. An experimental campaign to validate the simulations' results have been performed by means of the threshold $^{51}V(p, n)^{51}Cr$ at MTA ATOMKI and permitted to evaluate the efficiency in the energy region of interest within an uncertainty of 5%: in particular the efficiency for the setup are 34% and 31% for the ST and MT chambers, respectively.

A huge study on the targets used has been performed as well, to keep under control possible systematic uncertainty already highlighted in the literature. For the measurement, 99% enriched ^{13}C powder have been evaporated onto Tantalum backing. A deep target characterisation study has been fundamental for the choice of the strategy of data acquisition and analysis for the $^{13}C(\alpha, n)^{16}O$ cross section.

An alternation of proton beam and alpha beam was used during the experimental measurement: the $\gamma - rays$ spectra emitted by $^{13}C(p, \gamma)^{14}N$ reaction and acquired with a HPGe detector were used for a gamma shape analysis on the DC \rightarrow GS peak. An innovative analysis it has been developed with the final goal to quantity the target modification as a function of cumulative alpha charge. With the impinging of the alpha beam on target, we can contaminate the target with inactive nuclei and consequently the effective stopping power changes. This causes a yield reduction and a different shape in the peak under analysis. I demonstrated that this analysis is independent of the nucleus assumed as contaminant: this is due to parallel behaviour of the stopping power of elements in the energy region of interest of the analysis. For this reason I chose the Oxygen as reference contaminant nucleus and I estimated the ratio of inactive and active nuclei in the target as a free parameter in the fit. This value is extracted from the gamma shape with with an uncertainty between 5% and 10%.

The modification in the target composition was used as correction in the experimental neutron yield, defined as the number of neutron detected per unit of charge on the target. Thanks to this attention for all the experimental aspects, we have performed a measurement with unprecedented overall uncertainties between 10% and 15%, with a clear separation between statistical and systematic uncertainties.

In this work we were able to measure the $^{13}C(\alpha, n)^{16}O$ cross section in an energy range $260 < E < 305$ keV, measuring the lowest point ever measured with a direct measurement going down of 20 keV with respect to the lowest point measured by Drotleff et al [2].

This will help to put more constrain on the near threshold resonance once a complete R-matrix will be performed. To further improve the situation, the $^{13}\text{C}(\alpha, n)^{16}\text{O}$ reaction cross section measurement will continue in two directions. In the short period, the first half of 2019, at LUNA 400 accelerator another data taking campaign will be performed in order to increase the statistic at low energy points (340, 320 and 300 keV). In 2020-2021 the LUNA MV facility will be installed at LNGS providing an alpha beam up to 3.6 MeV energy. This will allow to measure the $^{13}\text{C}(\alpha, n)^{16}\text{O}$ at higher energies that will give the unique possibility to provide a complete data set over a wide energy range with well known systematic uncertainties. This approach will establish a robust extrapolation over the full Gamow peak.

Appendix A

Measurement runs

In this appendix I will list the runs on the targets used for the $^{13}\text{C}(\alpha, n)^{16}\text{O}$ cross section evaluation at each energy.

On the left part of the table I inserted the values of the parameters fitted in the gamma shape: the standard deviation of the gaussian function that parametrize the energy resolution of the HPGe σ_{HPGe} , target thickness in nm Δx , the normalization constant k and the degradation parameter Ni/Na .

In the right part of tables the extrapolated values of the stoichiometric ratio used for the $^{13}\text{C}(\alpha, n)^{16}\text{O}$ analysis.

$$E_{\alpha, \text{lab}} = 400 \text{ keV}$$

	proton run								alpha run			
	run	σ_{HPGe}	$\Delta x(\text{nm})$	$k(a.u)$	χ^2_{red}	Qpart	Qcum	Ni/Na	$\delta(\text{Ni/Na})$	Q_{av}	Ni/Na_{av}	$\delta(Ni/Na)_{\text{av}}$
T12	T12_ref1	3.671	182.023	0.0359	1.81	289409	289409	0	0	72352.25	0	
	T12_ref2	3.848	181.417	0.042	1.74	316837	1898246	0.048	0.013	942266	0.024	0.010 alpha1
	T12_ref3	4.23	180.000	0.037	1.81	371293	3310837	0.302	0.02	2432509	0.175	0.017 alhpas2
	T12_ref4	4.757	181.417	0.0437	2.48	437066	5338284	0.538	0.025	4122470.75	0.420	0.022 alpha3

	proton run								alpha run			
	run	σ_{HPGe}	$\Delta x(\text{nm})$	$k(a.u)$	χ^2_{red}	Qpart	Qcum	Ni/Na	$\delta(\text{Ni/Na})$	Q_{av}	Ni/Na_{av}	$\delta(Ni/Na)_{\text{av}}$
T22	T22_ref1	5.8	179.999	0.066	1.95	196412	196412	0	0	73654.5	0	0
	T22_ref2	5.8	179.999	0.064	1.49	204725	1401958	0.173	0.017	749042.875	0.087	0.012 alpha1
	T22_ref3	4.751	165.675	0.054	3.07	340779	2764406	0.293	0.015	2014994	0.233	0.016 alpha2
	T22_ref4	4.478	165.676	0.057137114	3.44	282797	4092916	0.695	0.028	3350714	0.494	0.022 alpha3

	proton run								alpha run			
	run	σ_{HPGe}	$\Delta x(\text{nm})$	$k(a.u)$	χ^2_{red}	Qpart	Qcum	Ni/Na	$\delta(\text{Ni/Na})$	Q_{av}	Ni/Na_{av}	$\delta(Ni/Na)_{\text{av}}$
T25	T25_ref1	5.445	130	0.0449	1.98	224144	224144	0	0	84054	0	0
	T25_ref2	5.177	130	0.044	1.43	232350	1456924	0.106	0.016	783472.25	0.053	0.011 alpha1
	T25_ref3	5.420	130	0.045	2.08	255608	2739658	0.128	0.013	2037296.25	0.117	0.0146 alpha2
	T25_ref4	5.445	130	0.045	2.75	240761	3984669	0.184	0.018	3300117.375	0.156	0.0157 alpha3

	proton run								alpha run			
	run	σ_{HPGe}	$\Delta x(\text{nm})$	$k(a.u)$	χ^2_{red}	Qpart	Qcum	Ni/Na	$\delta(\text{Ni/Na})$	Q_{av}	Ni/Na_{av}	$\delta(Ni/Na)_{\text{av}}$
T32	T32_ref1	5.188	140	0.049	1.22	209248	290052	0	0	118870	0	0
	T32_ref2	5.093	140	0.049	2.03	211490	1727367	0.221	0.004	956117.25	0.110	0.003 alpha1
	T32_ref3	5.379	140	0.049	2.25	223661	2989181	0.227	0.025	2303880.125	0.224	0.0178 alpha2
	T32_ref4	5.379	140	0.049	1.9	213569	4293787	0.207	0.018	3586830.25	0.217	0.022 alpha3

	proton run								alpha run			
	run	σ_{HPGe}	$\Delta x(\text{nm})$	$k(a.u)$	χ^2_{red}	Qpart	Qcum	Ni/Na	$\delta(\text{Ni/Na})$	Q_{av}	Ni/Na_{av}	$\delta(Ni/Na)_{\text{av}}$
MT10	MT10_ref1	5.201	170	0.058	2.61	717441	717441	0	0	179360.25	0	0
	MT10_ref2	5.18	170	0.058	2.13	254118	4507951	0.565	0.025	2369806.25	0.282	0.0177 alpha1

$$E_{\alpha, \text{lab}} = 390 \text{ keV}$$

	proton run								alpha run			
	run	σ_{HPGe}	$\Delta x(nm)$	$k(a.u)$	χ^2_{red}	Qpart	Qcum	Ni/Na	$\delta(Ni/Na)$	Q_{av}	Ni/Ni_{av}	$\delta(Ni/Ni_{av})$
MT1	MT1_ref1	4.629	140	0.040	2.53	248744	248746	0		93279.75	0	0
	MT1_ref2	3.81	143.578	0.039	2.96	292409	2519230	0.275	0.018	1316343.625	0.138	0.0128
	MT1_ref3	3.655	144.415	0.039	5.74	358938	4317272	0.806	0.033	3336832.625	0.540	0.026

	proton run							alpha run				
	run	σ_{HPGe}	$\Delta x(nm)$	$k(a.u)$	X_{red}^2	Qpart	Qcum	Ni/Na	$\delta(Ni/Na)$	Q_w	Ni/Na_{av}	$\delta(Ni/Na)_{av}$
MT11	MT11_ref1	4.194203	170	0.042951784	2.39	220075	220075	0		82528.125	0	0
	MT11_ref2	3.910	169.95	0.0429	2.67	242154	1962863	0.234	0.023	1033690.375	0.117	0.016
	MT11_ref3	3.910	171.932402	0.043	2.12	233034	3722495	0.304	0.022	2783280.5	0.269	0.023

MT7	proton run								alpha run			
	run	σ_{HPGe}	$\Delta x(nm)$	$k(a.u)$	χ^2_{red}	Qpart	Qcum	Ni/Na	$\delta(Ni/Na)$	Q_{av}	Ni/Na_{av}	$\delta(Ni/Na)_{av}$
	MT17-ref1	3.523	169.202	0.043	1.43	218656	218656	0		81996	0	0
MT17-ref2	3.363	171.219	0.043	2.53	5777111	5266285	1.273	0.035	2642924.625	0.636	0.025	alpha1

MT6	proton run								alpha run			
	run	σ_{HPGe}	$\Delta x(nm)$	$k(a.u)$	X_{red}^2	Qpart	Qcum	Ni/Na	$\delta(Ni/Na)$	Q_{av}	Ni/Na_{av}	$\delta(Ni/Na)_{av}$
	MT6_refl	4.053	171.3217452	0.03923673	1.94	247676	247676	0		92878.5	0	0
MT6_ref2	3.36	171.219	0.0426	1.23	226102	3669068	0.602	0.03	1899149.75	0.301	0.021	alpha1

$$E_{\alpha,lab} = 380 \text{ keV}$$

T21	proton run								alpha run			
	run	σ_{HPGe}	$\Delta x(nm)$	$k(a.u)$	χ^2_{red}	Qpart	Qcum	Ni/Na	$\delta(Ni/Na)$	Q_{av}	Ni/Na_{av}	$\delta(Ni/Na)_{av}$
	T21_ref1	4.685	160.00	0.046	1.4	175429	175429	0		65785.875	0	0
	T21_ref2	4.695	163.118	0.0470	2.34	267094	3332448	0.154	0.015	1698623.125	0.076	0.010

MT3	proton run								alpha run			
	run	σ_{HPGe}	$\Delta x(nm)$	$k(a.u)$	χ^2_{red}	Qpart	Qcum	Ni/Na	$\delta(Ni/Na)$	Q_{av}	Ni/Na_{av}	$\delta(Ni/Na)_{av}$
	MT3_ref1	5.102	139.568	0.043	1.49	129601	129601	0		48600.375	0	0
MT3_ref2	5.102	139.569	0.043	2.29	201870	3285503	0.535	0.0305	1666118.125	0.268	0.022	alpha1

MT4	proton run								alpha run			
	run	σ_{HPCe}	$\Delta x(nm)$	$k(a.u)$	χ^2_{red}	Qpart	Qcum	Ni/Na	$\delta(Ni/Na)$	Q_{av}	Ni/Na_{av}	$\delta(Ni/Na)_{av}$
	MT4_ref2	4.686	160.00	0.046	1.32	83622	265412	0		122253.25	0	0
	MT4_ref3	4.686	160.00	0.047	1.59	482504	4030809	1.615	0.038	2077344.75	0.808	0.027

T20	proton run								alpha run			
	run	σ_{HPGe}	$\Delta x(nm)$	$k(a.u)$	χ^2_{red}	Qpart	Qcum	Ni/Na	$\delta(Ni/Na)$	Q_{av}	Ni/Na_{av}	$\delta(Ni/Na)_{av}$
	T20-ref1	4.685	160.00	0.046	1.79	207767	207767	0		77912.625	0	0
	T20-ref2	4.686	160.00	0.047	2.51	203272	3228374	0.1666752153	0.018	1666690.625	0.083	0.013

$$E_{\alpha,lab} = 370 \text{ keV}$$

T30	proton run								alpha run				
	run	σ_{HPGe}	$\Delta x(nm)$	$k(a.u)$	χ^2_{red}	Qpart	Qcum	Ni/Na	$\delta(Ni/Na)$	Q_{av}	Ni/N_{av}	$\delta(Ni/N_{av})_{av}$	
	T30_refl	4.33	230.00	0.074	1.13	160155	160155	0		60058.125	0	0	
	T30_ref2	4.950	229.1334	0.073	1.22	192218	3012905	0.221	0.017	1542483.375	0.110	0.012	alpha1

T13	proton run								alpha run				
	run	σ_{HPGe}	$\Delta x(nm)$	$k(a.u)$	χ^2_{red}	Qpart	Qcum	Ni/Na	$\delta(Ni/Na)$	Q_{av}	Ni/Ni_{av}	$\delta(Ni/Ni)_{av}$	
	T13_refl	3.865	189.99	0.054	2.15	205388	205388	0		77020.5	0	0	
	T13_ref2	3.947	190.396	0.054	1.42	217978	2784304	0.202	0.016	1441925.25	0.101	0.011	alpha1

T16	proton run								alpha run			
	run	σ_{HPGe}	$\Delta x(nm)$	$k(a.u)$	χ^2_{red}	Qpar	Qcum	Ni/Na	$\delta(Ni/Na)$	Q_{av}	Ni/Na_{av}	$\delta(Ni/Na)_{av}$
	T16_refl	5.345	202.559	0.080	1.7	162403	162403	0		60901.125	0	0
T16_ref2	5.175	202.558	0.080	3.13	168708	2421491	0.487	0.023	1250558.125	0.243	0.016	alpha1

T23	proton run								alpha run			
	run	σ_{HPGe}	$\Delta x (nm)$	$k(a.u)$	χ^2_{red}	Qpart	Qcum	Ni/Na	$\delta(\text{Ni}/\text{Na})$	Q_{av}	Ni/Ni_{av}	$\delta(Ni/Ni)_{av}$
	T23_ref1	5.523	201.726	0.071	1.47	154679	154679	0		58004.625	0	0
T23_ref2	5.842	200.00	0.071	2.25	187457	2875744	0.510	0.026	1472444.5	0.255	0.018	alpha1

T29	proton run								alpha run				
	run	σ_{HPGe}	$\Delta x(nm)$	$k(a.u)$	χ^2_{red}	Qpar	Qcum	Ni/Na	$\delta(Ni/Na)$	Q_{av}	Ni/Na_{av}	$\delta(Ni/Na)_{av}$	
	T29_refl	5.484	199.99	0.073	1.34	145143	145143	0		54428.625	0	0	
	T29_ref2	5.484	199.99	0.073	2.44	172222	2451618	0.258	0.018	1258709.875	0.129	0.012	alpha1

T26	proton run									alpha run			
	run	σ_{HPGe}	$\Delta x(nm)$	$k(a.u)$	χ^2_{red}	Qpart	Qcum	Ni/Na	$\delta(Ni/Na)$	Q_{av}	Ni/Ni_{av}	$\delta(Ni/Ni_{av})$	
	T26_ref1	5.523	201.726	0.073	1.72	149056	149056	0		55896	0	0	
	T26_ref2	4.964	203.499	0.072	1.39	162538	1339595	0.108	0.015	705376.25	0.054	0.010	alpha1

$$E_{\alpha,lab} = 360 \text{ keV}$$

MT15	proton run								alpha run			
	run	σ_{HPGe}	$\Delta x(nm)$	$k(a.u)$	χ^2_{red}	Qpart	Qcum	Ni/Na	$\delta(Ni/Na)$	Q_{av}	Ni/Ni_{av}	$\delta(Ni/Na)_{av}$
	MT15_ref1	4.903	199.00	0.063	1.89	166409	166409	0		62403.375	0	0
MT15_ref2	4.323	190.865	0.057	1.75	222274	3700498	0.552	0.026	1884868.125	0.276	0.018	alpha1

MT13	proton run								alpha run			
	run	σ_{HPGe}	$\Delta x(nm)$	$k(a.u)$	χ^2_{red}	Qpart	Qcum	Ni/Na	$\delta(Ni/Na)$	Q_{av}	Ni/Na_{av}	$\delta(Ni/Na)_{av}$
	MT13_ref1	3.99	181.763	0.049	1.78	219494	219494	0		82310.25	0	0
MT13_ref2	5.195	179.99	0.050	1.88	281590	3070356	0.70	0.01	1582289.5	0.355	0.007	alpha1

MT18	proton run								alpha run			
	run	σ_{HPGe}	$\Delta x \text{ (nm)}$	$k \text{ (a.u.)}$	χ^2_{red}	Qpart	Qcum	Ni/Na	$\delta(\text{Ni/Na})$	Q_{av}	Ni/Ni_{av}	$\delta(Ni/Na)_{av}$
	MT18_refl	4.496	182.306	0.049	1.55	232715	232715	0		87268.125	0	0
MT18_ref2	5.297	179.99	0.05	2.59	228280	3585036	0.541	0.027	1851251.125	0.271	0.019	alpha1

MT17	proton run								alpha run			
	run	$\sigma_{H\bar{P}G\bar{e}}$	$\Delta x (nm)$	$k(a.u)$	χ^2_{red}	Qpart	Qcum	Ni/Na	$\delta(Ni/Na)$	Q_{av}	Ni/Ni_{av}	$\delta(Ni/Ni)_{av}$
	MT17_ref1	4.443	199.99	0.0601	1.28	140854	140854	0		52820.25	0	0
MT17_ref2	4.443	199.99	0.067	2.5	148437	2549951	0.641867119	0.03	1309241.125	0.32	0.021	alpha1

MT20	proton run								alpha run			
	run	σ_{HGPe}	$\Delta x \text{ (nm)}$	$k \text{ (a.u.)}$	X_{red}^2	Qpart	Qcum	Ni/Na	$\delta(\text{Ni/Na})$	Q_{av}	Ni/N_{hadav}	$\delta(Ni/Na)_{av}$
	MT20_refl	5.362	143.487	0.0484	1.13	144457	144457	0		54171.375	0	0
MT20_ref2	5.583	140.00	0.0495	1.47	69800	3176332	0.670	0.055	1633612.375	0.335	0.039	alpha1

MT24	proton run								alpha run			
	run	σ_{HGG}	$\Delta x(nm)$	$k(a.u)$	χ^2_{red}	Qpart	Qcum	Ni/Na	$\delta(Ni/Na)$	Q_{av}	Ni/N_{av}	$\delta(Ni/Na)_{av}$
	MT24_ref1	5.651	122.781	0.048	2.08	131024	131024	0		49134	0	0
MT24_ref2	5.651	128.781	0.051	4.91	158089	2758535	0.492	0.039	1408640.375	0.246	0.028	alpha1

$$E_{\alpha,lab} = 340 \text{ keV}$$

T51	proton run								alpha run			
	run	σ_{HPGe}	$\Delta x\,(nm)$	$k\,(a.u)$	χ^2_{red}	Qpar	Qcum	Ni/Na	$\delta(Ni/Na)$	Q_{av}	Ni/Ni_{av}	$\delta(Ni/Na)_{av}$
	T51_ref2	5.513	230	0.082	1.32	304705	304705	0	0	114264.375	0	0
	T51_ref3	5.5627	230	0.082	1.96	285683	1532492	0.084441949	0.015	844800	0.042	0.011
	T51_ref4	5.562	230	0.082	2.31	258188	2800226	0.212841018	0.018	2098375.125	0.148	0.016
	T51_ref5	5.5627	230	0.082	1.75	222141	4028400	0.557169406	0.025	3534271.875	0.385	0.0218
	T51_ref6	5.5627	230	0.082	1.88	209999	5015296	0.560575917	0.025	4467830.5	0.559	0.025

	proton run									alpha run			
	run	σ_{HPGe}	$\Delta x(nm)$	$k(a.u)$	χ^2_{red}	Qpart	Qcum	Ni/Na	$\delta(Ni/Na)$	Q_{av}	Ni/Na_{av}	$\delta(Ni/Na)_{av}$	
T38	T38_ref1	5.514	230.000	0.083	1.45	304705.000	304705.000	0.000		114264.375	0.000	0.000	
	T38_ref2	5.812	230.000	0.104	1.87	285683.000	1532492.000	0.102	0.010	844800.000	0.051	0.007	alpha1
	T38_ref3	5.812	230.000	0.104	2.05	258188.000	2800226.000	0.280	0.016	2098375.125	0.191	0.013	alpha2
	T38_ref4	5.812	230.000	0.104	1.98	222141.000	4028400.000	0.621	0.024	3354271.875	0.451	0.020	alpha3
	T38_ref5	5.812	230.000	0.104	2.54	209999.000	5015296.000	0.701	0.024	4467830.500	0.661	0.024	alpha4

	proton run									alpha run			
	run	σ_{HPGe}	$\Delta x(nm)$	$k(a.u)$	χ^2_{red}	Qpart	Qcum	Ni/Na	$\delta(Ni/Na)$	Q_{av}	Ni/Na_{av}	$\delta(Ni/Na)_{av}$	
T61	T61_ref1	5.307	190.506	0.068	2.03	304705.000	304705.000	0.000		114264.375	0.000	0.000	
	T61_ref2	5.655	190.000	0.068	1.97	285683.000	1532492.000	0.033	0.009	844800.000	0.017	0.007	alpha1
	T61_ref3	5.655	190.000	0.068	1.54	258188.000	2800226.000	0.140	0.012	2098375.125	0.087	0.011	alpha2
	T61_ref4	5.862	190.000	0.068	2.75	222141.000	4028400.000	0.292	0.018	3354271.875	0.216	0.015	alpha3
	T61_ref5	5.357	191.515	0.066	2.38	209999.000	5015296.000	0.403	0.021	4467830.500	0.348	0.020	alpha4

Bibliography

- [1] S. Cristallo, M. La Cognata, C. Massimi, A. Best, S. Palmerini, O. Straniero, O. Trippella, M. Busso, G. F. Ciani, F. Mingrone, L. Pierconti, and D. Vescovi. The importance of the $^{13}\text{C}(\alpha, n)^{16}\text{O}$ reaction in asymptotic giant branch stars. *The Astrophysical Journal*, 859(2):105, 2018.
- [2] H. W. Drotleff, A. Denker, H. Knee, M. Soine, G. Wolf, J. W. Hammer, U. Greife, C. Rolfs, and H. P. Trautvetter. Reaction rates of the s-process neutron sources $\text{Ne}22(\alpha, n)\text{Mg}25$ and $\text{C}13(\alpha, n)\text{O}16$. *Astrophysical Journal*, 414:735–739, September 1993.
- [3] A. M. Mukhamedzhanov, Shubhchintak, and C. A. Bertulani. Sub-threshold resonances and resonances in the r -matrix method for binary reactions and in the trojan horse method. *Phys. Rev. C*, 96:024623, Aug 2017.
- [4] M. La Cognata, C. Spitaleri, O. Trippella, G. G. Kiss, G. V. Rogachev, A. M. Mukhamedzhanov, M. Avila, G. L. Guardo, E. Koshchiy, A. Kuchera, L. Lamia, S. M. R. Puglia, S. Romano, D. Santiago, and R. Spartá. On the measurement of the $^{13}\text{C}(\alpha, n)^{16}\text{O}$ S-factor at negative energies and its influence on the s-process. *The Astrophysical Journal*, 777(2):143, 2013.
- [5] A. Formicola, G. Imbriani, M. Junker, D. Bemmerer, R. Bonetti, C. Brosgini, C. Casella, P. Corvisiero, H. Costantini, G. Gervino, C. Gustavino, A. Lemut, P. Prati, V. Roca, C. Rolfs, M. Romano, D. Schürmann, F. Strieder, F. Terrasi, H.-P. Trautvetter, and S. Zavatarelli. The LUNA II 400kV accelerator. *Nuclear Instruments and Methods in Physics Research Section A: Accelerators, Spectrometers, Detectors and Associated Equipment*, 507(3):609 – 616, 2003.
- [6] C.E. Rolfs and W.S. Rodney. *Cauldrons in the Cosmos: Nuclear Astrophysics*. Theoretical Astrophysics. University of Chicago Press, 1988.
- [7] E. E. Salpeter. Electrons Screening and Thermonuclear Reactions. *Australian Journal of Physics*, 7:373, September 1954.
- [8] C. Spitaleri, C. A. Bertulani, L. Fortunato, and A. Vitturi. The electron screening puzzle and nuclear clustering. *Physics Letters B*, 755:275–278, April 2016.
- [9] C. Spitaleri, S. Cherubini, A. Del Zoppo, A. Di Pietro, P. Figuerab, M. Gulino, M. Lattuada, Dstroke; Miljanić, A. Musumarra, M.G. Pellegriti, R.G. Pizzone, C. Rolfs, S. Romano, S. Tudisco, and A. Tumino. The Trojan Horse Method in nuclear astrophysics. *Nuclear Physics A*, 719:C99 – C106, 2003.

- [10] Tumino, Aurora, Spitaleri, Claudio, Cherubini, Silvio, D'Agata, Giuseppe, Giovanni Luca, Guardo, Gulino, Marisa, Indelicato, Iolanda, La Cognata, Marco, Lamia, Livio, Rosario Gianluca, Pizzone, Giuseppe Gabriele, Rapisarda, Romano, Stefano, Maria Letizia, Sergi, and Spartá, Roberta. The trojan horse method in nuclear astrophysics. *EPJ Web Conf.*, 184:01016, 2018.
- [11] I. Iben, Jr. Stellar Evolution.VI. Evolution from the Main Sequence to the Red-Giant Branch for Stars of Mass $1M_{\odot}$, $1.25 M_{\odot}$, and $1.5 M_{\odot}$. *Astrophysical Journal*, 147:624, February 1967.
- [12] V. Castellani, M. Marconi, and O. Straniero. On the convective envelope of AGB stars. *Astronomy and Astrophysics*, 340:160–162, December 1998.
- [13] O. Straniero, R. Gallino, and S. Cristallo. s process in low-mass asymptotic giant branch stars. *Nuclear Physics A*, 777:311–339, October 2006.
- [14] W. Merrill, P. Technetium in the stars. *Science*, 115:479–89, 1952.
- [15] R. H. Sanders. S-Process Nucleosynthesis in Thermal Relaxation Cycles. *Astrophysical Journal*, 150:971, December 1967.
- [16] Tadao Mitsui. Low-energy neutrino physics with KamLAND. *Nuclear Physics B - Proceedings Supplements*, 217(1):89 – 94, 2011. Proceedings of the Neutrino Oscillation Workshop (NOW 2010).
- [17] M. Agostini, S. Appel, G. Bellini, J. Benziger, D. Bick, G. Bonfini, D. Bravo, B. Caccianiga, F. Calaprice, A. Caminata, P. Cavalcante, A. Chepurnov, K. Choi, D. D'Angelo, S. Davini, A. Derbin, L. Di Noto, I. Drachnev, A. Empl, A. Etenko, G. Fiorentini, K. Fomenko, D. Franco, F. Gabriele, C. Galbiati, C. Ghiano, M. Giammarchi, M. Goeger-Neff, A. Goretti, M. Gromov, C. Hagner, T. Houdy, E. Hungerford, Aldo Ianni, Andrea Ianni, K. Jedrzejczak, M. Kaiser, V. Kobychev, D. Koralev, G. Korga, D. Kryn, M. Laubenstein, B. Lehnert, E. Litvinovich, F. Lombardi, P. Lombardi, L. Ludhova, G. Lukyanchenko, I. Machulin, S. Manecki, W. Maneschg, F. Mantovani, S. Marcocci, E. Meroni, M. Meyer, L. Miramonti, M. Misiaszek, M. Montuschi, P. Mosteiro, V. Muratova, B. Neumair, L. Oberauer, M. Obolensky, F. Ortica, K. Otis, L. Pagani, M. Pallavicini, L. Papp, L. Perasso, A. Pocar, G. Ranucci, A. Razeto, A. Re, B. Ricci, A. Romani, R. Roncin, N. Rossi, S. Schönert, D. Semenov, H. Simgen, M. Skorokhvatov, O. Smirnov, A. Sotnikov, S. Sukhotin, Y. Suvorov, R. Tartaglia, G. Testera, J. Thurn, M. Toropova, E. Unzhakov, R. B. Vogelaar, F. von Feilitzsch, H. Wang, S. Weinz, J. Winter, M. Wojcik, M. Wurm, Z. Yokley, O. Zaimidoroga, S. Zavatarelli, K. Zuber, and G. Zuzel. Spectroscopy of geoneutrinos from 2056 days of Borexino data. *Phys. Rev. D*, 92:031101, Aug 2015.
- [18] M. Wójcik and G. Zuzel. ^{226}Ra , ^{210}Pb , ^{210}Bi and ^{210}Po deposition and removal from surfaces and liquids. *Journal of Radioanalytical and Nuclear Chemistry*, 296(2):639–645, May 2013.
- [19] S. Harissopoulos, H. W. Becker, J. W. Hammer, A. Lagoyannis, C. Rolfs, and F. Strieder. Cross section of the $^{13}\text{C}(\alpha, n)^{16}\text{O}$ reaction: A background for the measurement of geo-neutrinos. *Phys. Rev. C*, 72:062801, Dec 2005.

- [20] D. R. Tilley, H. R. Weller, and C. M. Cheves. Energy levels of light nuclei $A = 16\text{--}17$. *Nucl. Phys.*, A564:1–183, 1993.
- [21] Keeley, N., Kemper, K. W., and Rusek, K. A cautionary tale: The coulomb modified anc for the $1/2^+$ 2 state in ^{17}O . *Eur. Phys. J. A*, 54(5):71, 2018.
- [22] D.R. Tilley, H.R. Weller, and C.M. Cheves. Energy levels of light nuclei $A = 16\text{--}17$. *Nuclear Physics A*, 564(1):1 – 183, 1993.
- [23] E. D. Johnson, G. V. Rogachev, A. M. Mukhamedzhanov, L. T. Baby, S. Brown, W. T. Cluff, A. M. Crisp, E. Diffenderfer, V. Z. Goldberg, B. W. Green, T. Hinnens, C. R. Hoffman, K. W. Kemper, O. Momotyuk, P. Peplowski, A. Pipidis, R. Reynolds, and B. T. Roeder. Astrophysical reaction rate for the neutron-generator reaction $^{13}\text{C}(\alpha, n)^{16}\text{O}$ in asymptotic giant branch stars. *Phys. Rev. Lett.*, 97:192701, Nov 2006.
- [24] M. G. Pellegriti, F. Hammache, P. Roussel, L. Audouin, D. Beaumel, P. Descouvemont, S. Fortier, L. Gaudefroy, J. Kiener, A. Lefebvre-Schuhl, M. Stanoiu, V. Tatischeff, and M. Vilmay. Indirect study of the $^{13}\text{C}(\alpha, n)^{16}\text{O}$ reaction via the $^{13}\text{C}(^7\text{Li}, t)^{17}\text{O}$ transfer reaction. *Phys. Rev. C*, 77:042801, Apr 2008.
- [25] B. Guo, Z. H. Li, M. Lugaro, J. Buntain, D. Y. Pang, Y. J. Li, J. Su, S. Q. Yan, X. X. Bai, Y. S. Chen, Q. W. Fan, S. J. Jin, A. I. Karakas, E. T. Li, Z. C. Li, G. Lian, J. C. Liu, X. Liu, J. R. Shi, N. C. Shu, B. X. Wang, Y. B. Wang, S. Zeng, and W. P. Liu. New Determination of the $^{13}\text{C}(\alpha, n)^{16}\text{O}$ Reaction Rate and its Influence on the s-process Nucleosynthesis in AGB Stars. "Astroparticle Journal", 756:193, September 2012.
- [26] M. L. Avila, G. V. Rogachev, E. Koshchiy, L. T. Baby, J. Belarge, K. W. Kemper, A. N. Kuchera, and D. Santiago-Gonzalez. New measurement of the α asymptotic normalization coefficient of the $1/2^+$ state in ^{17}O at 6.356 mev that dominates the $^{13}\text{C}(\alpha, n)^{16}\text{O}$ reaction rate at temperatures relevant for the s process. *Phys. Rev. C*, 91:048801, Apr 2015.
- [27] O. Trippella and M. La Cognata. Concurrent application of anc and thm to assess the $^{13}\text{C}(\alpha, n)^{16}\text{O}$ absolute cross section at astrophysical energies and possible consequences for neutron production in low-mass agb stars. *The Astrophysical Journal*, 837(1):41, 2017.
- [28] T. Faestermann, P. Mohr, R. Hertenberger, and H.-F. Wirth. Broad levels in ^{17}O and their relevance for the astrophysical s process. *Phys. Rev. C*, 92:052802, Nov 2015.
- [29] A. M. Mukhamedzhanov, Shubhchintak, and C. A. Bertulani. Sub-threshold resonances and resonances in the *r*-matrix method for binary reactions and in the trojan horse method. *Phys. Rev. C*, 96:024623, Aug 2017.
- [30] K. K. Sekharan, A. S. Divatia, M. K. Mehta, S. S. Kerekatte, and K. B. Nambiar. $^{13}\text{C}(\alpha, n)^{16}\text{O}$ reaction cross section between 1.95 and 5.57 MeV. *Phys. Rev.*, 156:1187–1190, Apr 1967.

- [31] Cary N. Davids. A study of (α, n) reactions on ${}^9\text{Be}$ and ${}^{13}\text{C}$ at low energies. *Nuclear Physics A*, 110(3):619 – 636, 1968.
- [32] J. K. Bair and F. X. Haas. Total Neutron Yield from the Reactions C-13 (α, n) O-16 and O-17, O-18 (α, n) Ne-20, Ne-21. *Phys. Rev., C*7:1356–1364, 1973.
- [33] C. R. Brune, I. Licot, and R. W. Kavanagh. Low-energy resonances in ${}^{13}\text{C}(\alpha, n)$. *Phys. Rev. C*, 48:3119–3121, Dec 1993.
- [34] M. Heil, R. Detwiler, R. E. Azuma, A. Couture, J. Daly, J. Görres, F. Käppeler, R. Reifarth, P. Tischhauser, C. Ugalde, and M. Wiescher. The ${}^{13}\text{C}(\alpha, n)$ reaction and its role as a neutron source for the *s* process. *Phys. Rev. C*, 78:025803, Aug 2008.
- [35] F. Ajzenberg-Selove. Energy levels of light nuclei $A = 16\text{-}17$. *Nucl. Phys.*, A460:1–110, 1986.
- [36] C. Angulo, M. Arnould, M. Rayet, P. Descouvemont, D. Baye, C. Leclercq-Willain, A. Coc, S. Barhoumi, P. Aguer, C. Rolfs, R. Kunz, J. W. Hammer, A. Mayer, T. Paradellis, S. Kossionides, C. Chronidou, K. Spyrou, S. degl'Innocenti, G. Fiorentini, B. Ricci, S. Zavatarelli, C. Providencia, H. Wolters, J. Soares, C. Grama, J. Rahighi, A. Shotter, and M. Lamehi Rachti. A compilation of charged-particle induced thermonuclear reaction rates. *Nuclear Physics A*, 656:3–183, August 1999.
- [37] G. Fiorentini, G. L. Fogli, E. Lisi, F. Mantovani, and A. M. Rotunno. Mantle geoneutrinos in KamLAND and Borexino. *Phys. Rev. D*, 86:033004, Aug 2012.
- [38] Peter Mohr. Revised cross section of the ${}^{13}\text{C}(\alpha, n){}^{16}\text{O}$ reaction between 5 and 8 MeV. *Phys. Rev. C*, 97:064613, Jun 2018.
- [39] S. Kubono, K. Abe, S. Kato, T. Teranishi, M. Kurokawa, X. Liu, N. Imai, K. Kumagai, P. Strasser, M. H. Tanaka, Y. Fuchi, C. S. Lee, Y. K. Kwon, L. Lee, J. H. Ha, and Y. K. Kim. Determination of the Subthreshold State Contribution in ${}^{13}\text{C}(\alpha, n){}^{16}\text{O}$, the Main Neutron-Source Reaction for the *s* Process. *Physical Review Letters*, 90(6):062501, February 2003.
- [40] M. Heil, A. Couture, J. Daly, R. Detwiler, J. Görres, G. Hale, F. Käppeler, R. Reifarth, U. Giesen, E. Stech, P. Tischhauser, C. Ugalde, and M. Wiescher. A measurement of the ${}^{13}\text{C}(\alpha, \alpha)$ differential cross section and its application to the ${}^{13}\text{C}(\alpha, n)$ reaction. *Nuclear Physics A*, 688(1):499 – 501, 2001. Nuclei in the Cosmos.
- [41] U. Greife, C. Arpesella, C.A. Barnes, F. Bartolucci, E. Bellotti, C. Broggini, P. Corvisiero, G. Fiorentini, A. Fubini, G. Gervino, F. Gorris, C. Gustavino, M. Junker, R.W. Kavanagh, A. Lanza, G. Mezzorani, P. Prati, P. Quarati, W.S. Rodney, C. Rolfs, W.H. Schulte, H.P. Trautvetter, and D. Zahnow. Laboratory for Underground Nuclear Astrophysics (LUNA). *Nuclear Instruments and Methods in Physics Research Section A: Accelerators, Spectrometers, Detectors and Associated Equipment*, 350(1):327 – 337, 1994.

- [42] Donald E. Groom, Nikolai V. Mokhov, and Sergei I. Striganov. Muon stopping power and range tables 10 MeV -100 TeV. *Atomic Data and Nuclear Data Tables*, 78(2):183 – 356, 2001.
- [43] D.-M. Mei and A. Hime. Muon-induced background study for underground laboratories. *Phys. Rev. D*, 73:053004, Mar 2006.
- [44] H Costantini, A Formicola, G Imbriani, M Junker, C Rolfs, and F Strieder. LUNA: a Laboratory for Underground Nuclear Astrophysics. *Reports on Progress in Physics*, 72(8):086301, 2009.
- [45] Andreas Best, Joachim Görres, Matthias Junker, Karl-Ludwig Kratz, Matthias Laubenstein, Alexander Long, Stefano Nisi, Karl Smith, and Michael Wiescher. Low energy neutron background in deep underground laboratories. *Nuclear Instruments and Methods in Physics Research Section A: Accelerators, Spectrometers, Detectors and Associated Equipment*, 812:1 – 6, 2016.
- [46] F. Arneodo, A. Borio di Tiglione, F. Cavanna, A. C. Y. Chen, R. Dolfini, R. Nardò, G. P. M. A. Rappoldi, G. L. Raselli, M. Rossella, C. R. M. Tatananni, and M. Terrani. Neutron background measurements in the Hall C of the Gran Sasso Laboratory. *Nuovo Cimento A Serie*, 112:819, August 1999.
- [47] Dariusz Malczewski, Jan Kisiel, and Jerzy Dorda. Gamma background measurements in the Gran Sasso National Laboratory. *Journal of Radioanalytical and Nuclear Chemistry*, 295(1):749–754, Jan 2013.
- [48] J. D. Dirk, M. E. Nelson, J. F. Ziegler, A. Thompson, and T. H. Zabel. Terrestrial thermal neutrons. *IEEE Transactions on Nuclear Science*, 50(6):2060–2064, Dec 2003.
- [49] P. Belli, R. Bernabei, S. d'Angelo, M. P. de Pascale, L. Paoluzi, R. Santonacci, N. Taborgna, N. Iucci, and G. Villoresi. Deep underground neutron flux measurement with large BF₃ counters. *Il Nuovo Cimento A (1965-1970)*, 101(6):959–966, Jun 1989.
- [50] J. F. Ziegler, J. P. Biersack, and Matthias D. Ziegler. *SRIM, the stopping and range of ions in matter*. SRIM Co., 2008.
- [51] T. L. Rucker. Methodologies for the practical determination and use of method detection limits. *Journal of Radioanalytical and Nuclear Chemistry*, 192(2):345–350, May 1995.
- [52] H. J. Assenbaum, K. Langanke, and C. Rolfs. Effects of electron screening on low-energy fusion cross sections. *Zeitschrift fur Physik A Hadrons and Nuclei*, 327:461–468, December 1987.
- [53] S. Agostinelli, J. Allison, K. Amako, J. Apostolakis, H. Araujo, P. Arce, M. Asai, D. Axen, S. Banerjee, G. Barrand, F. Behner, L. Bellagamba, J. Boudreau, L. Broglia, A. Brunengo, H. Burkhardt, S. Chauvie, J. Chuma, R. Chytracek, G. Cooperman, G. Cosmo, P. Degtyarenko,

- A. Dell'Acqua, G. Depaola, D. Dietrich, R. Enami, A. Feliciello, C. Ferguson, H. Fesefeldt, G. Folger, F. Foppiano, A. Forti, S. Garelli, S. Gianni, R. Giannitrapani, D. Gibin, J.J. Gómez Cadenas, I. González, G. Gracia Abril, G. Greeniaus, W. Greiner, V. Grichine, A. Grossheim, S. Guatelli, P. Gumplinger, R. Hamatsu, K. Hashimoto, H. Hasui, A. Heikkinen, A. Howard, V. Ivanchenko, A. Johnson, F.W. Jones, J. Kallenbach, N. Kanaya, M. Kawabata, Y. Kawabata, M. Kawaguti, S. Kelner, P. Kent, A. Kimura, T. Kodama, R. Kokoulin, M. Kossov, H. Kurashige, E. Lamanna, T. Lampén, V. Lara, V. Lefebure, F. Lei, M. Liendl, W. Lockman, F. Longo, S. Magni, M. Maire, E. Medernach, K. Minamimoto, P. Mora de Freitas, Y. Morita, K. Murakami, M. Nagamatu, R. Nartallo, P. Nieminen, T. Nishimura, K. Ohtsubo, M. Okamura, S. O'Neale, Y. Oohata, K. Paech, J. Perl, A. Pfeiffer, M.G. Pia, F. Ranjard, A. Rybin, S. Sadilov, E. Di Salvo, G. Santin, T. Sasaki, N. Savvas, Y. Sawada, S. Scherer, S. Sei, V. Sirotenko, D. Smith, N. Starkov, H. Stoecker, J. Sulkimo, M. Takahata, S. Tanaka, E. Tcherniaev, E. Safai Tehrani, M. Tropeano, P. Truscott, H. Uno, L. Urban, P. Urban, M. Verderi, A. Walkden, W. Wander, H. Weber, J.P. Wellisch, T. Wenau, D.C. Williams, D. Wright, T. Yamada, H. Yoshida, and D. Zschiesche. Geant4—a simulation toolkit. *Nuclear Instruments and Methods in Physics Research Section A: Accelerators, Spectrometers, Detectors and Associated Equipment*, 506(3):250 – 303, 2003.
- [54] G.F. Knoll. *Radiation Detection and Measurement*. Wiley, 2000.
- [55] T.J. Langford, C.D. Bass, E.J. Beise, H. Breuer, D.K. Erwin, C.R. Heimbach, and J.S. Nico. Event identification in ^{3}He proportional counters using risetime discrimination. *Nuclear Instruments and Methods in Physics Research Section A: Accelerators, Spectrometers, Detectors and Associated Equipment*, 717:51 – 57, 2013.
- [56] J. Balibrea-Correa, G.F. Ciani, R. Buompane, F. Cavanna, L. Csereki, R. Depalo, F. Ferraro, and A. Best. Improved pulse shape discrimination for high pressure ^{3}He counters. *Nuclear Instruments and Methods in Physics Research Section A: Accelerators, Spectrometers, Detectors and Associated Equipment*, 906:103 – 109, 2018.
- [57] L. Swiderski, M. Moszynski, D. Wolski, J. Iwanowska, T. Szczesniak, G. Pausch, C. Plettner, J. Stein, P. Schotanus, C. Hurlbut, and J. Szabelski. Comparison of neutron detection efficiency of a He-3 counter and a boron-10 loaded liquid scintillator. *IEEE Transactions on Nuclear Science*, 57(5):2857–2861, Oct 2010.
- [58] Matthew J.I. Balmer, Kelum A.A. Gamage, and Graeme C. Taylor. Comparative analysis of pulse shape discrimination methods in a ^{6}Li loaded plastic scintillator. *Nuclear Instruments and Methods in Physics Research Section A: Accelerators, Spectrometers, Detectors and Associated Equipment*, 788:146 – 153, 2015.
- [59] Emilio Mendoza, Daniel Cano-Ott, Tatsumi Koi, and Carlos Guerrero. New standard evaluated neutron cross section libraries for the geant4

code and first verification. *IEEE Transactions on Nuclear Science*, 61:2357–2364, 2014.

- [60] Sascha Falahat, Andreas Best, Manoel Couder, Joachim Görres, Karl-Ludwig Kratz, Uli Ott, Ed Stech, and Michael Wiescher. A 3he neutron detector for the measurement of (α, n) reactions. *Nuclear Instruments and Methods in Physics Research Section A: Accelerators, Spectrometers, Detectors and Associated Equipment*, 700:53 – 58, 2013.
- [61] A. Tarifeño-Saldivia, J.L. Tain, C. Domingo-Pardo, F. Calviño, G. Cortes, V.H. Phong, A. Riego, J. Agramunt, A. Algara, N. Brewer, R. Caballero-Folch, P.J. Coleman-Smith, T. Davinson, I. Dillmann, A. Estradé, C.J. Griffin, R. Grzywacz, L.J. Harkness-Brennan, G.G. Kiss, M. Kogimtzis, M. Labiche, I.H. Lazarus, G. Lorusso, K. Matsui, K. Miernik, F. Montes, A.I. Morales, S. Nishimura, R.D. Page, Z.S. Podolyák, V.F.E. Pucknell, B.C. Rasco, P. Regan, B. Rubio, K.P. Rykaczewski, Y. Saito, H. Sakurai, J. Simpson, E. Sokol, R. Surman, A. Svirkhin, S.L. Thomas, A. Tolosa, and P. Woods. Conceptual design of a hybrid neutron-gamma detector for study of β -delayed neutrons at the rib facility of riken. *Journal of Instrumentation*, 12(04):P04006, 2017.
- [62] A. Smith, R. Holt, and J. Whalen. Neutron interaction with Carbon-12 in the few-Mev region. *Nuclear Science and Engineering*, 70(3):281–293, 1979.
- [63] F.G.Perey and W.E.Kinney. Elastic and inelastic scattering cross sections in the energy range 5.2 - 8.7 mev. *U.S.AEC Nucl.Cross Sections Advisory Comm. Repts*, 42:190, 1978/11.
- [64] Chance Elliott, Vipin Vijayakumar, Wesley Zink, and Richard Hansen. National instruments labview: A programming environment for laboratory automation and measurement. *JALA: Journal of the Association for Laboratory Automation*, 12(1):17–24, 2007.
- [65] J.W. Marsh, D.J. Thomas, and M. Burke. High resolution measurements of neutron energy spectra from ambe and amb neutron sources. *Nuclear Instruments and Methods in Physics Research Section A: Accelerators, Spectrometers, Detectors and Associated Equipment*, 366(2):340 – 348, 1995.
- [66] W.P. Poenitz. Experimental determination of the efficiency of the grey neutron detector. *Nuclear Instruments and Methods*, 72(1):120 – 122, 1969.
- [67] J. Pereira, P. Hosmer, G. Lorusso, P. Santi, A. Couture, J. Daly, M. Del Santo, T. Elliot, J. Görres, C. Herlitzius, K.-L. Kratz, L.O. Lamm, H.Y. Lee, F. Montes, M. Ouellette, E. Pellegrini, P. Reeder, H. Schatz, F. Schertz, L. Schnorrenberger, K. Smith, E. Stech, E. Strandberg, C. Ugalde, M. Wiescher, and A. Wöhr. The neutron long counter NERO for studies of β -delayed neutron emission in the r-process. *Nuclear Instruments and Methods in Physics Research Section A: Accelerators, Spectrometers, Detectors and Associated Equipment*, 618(1):275 – 283, 2010.
- [68] G. Deconninck and J. Royen. La reaction 51v(p,n)51cr comme source de neutrons monoenergetiques. *Nuclear Instruments and Methods*, 75(2):266 – 270, 1969.

- [69] D.A. Vermilyea. The kinetics of formation and structure of anodic oxide films on tantalum. *Acta Metallurgica*, 1(3):282 – 294, 1953.
- [70] M. Ohring. *The Materials Science of Thin Films*. Referex Engineering. Academic Press, 1992.
- [71] B. W. Filippone, A. J. Elwyn, C. N. Davids, and D. D. Koetke. Proton capture cross section of ^7Be and the flux of high energy solar neutrinos. *Phys. Rev. C*, 28:2222–2229, Dec 1983.
- [72] F. Ajzenberg-Selove. Energy levels of light nuclei $A = 13 - 15$. *Nuclear Physics A*, 523(1):1 – 196, 1991.
- [73] LUNA Collaboration, Caciolli, A., Scott, D. A., Di Leva, A., Formicola, A., Aliotta, M., Anders, M., Bellini, A., Bemmerer, D., Broggini, C., Campeggio, M., Corvisiero, P., Depalo, R., Elekes, Z., Fülöp, Zs., Gervino, G., Guglielmetti, A., Gustavino, C., Gyürky, Gy., Imbriani, G., Junker, M., Marta, M., Menegazzo, R., Napolitani, E., Prati, P., Rigato, V., Roca, V., Rolfs, C., Rossi Alvarez, C., Somorjai, E., Salvo, C., Straniero, O., Strieder, F., Szücs, T., Terrasi, F., Trautvetter, H. P., and Trezzi, D. Preparation and characterisation of isotopically enriched ta^{205} targets for nuclear astrophysics studies. *Eur. Phys. J. A*, 48(10):144, 2012.
- [74] Luca Lista. Statistical Methods for Data Analysis in Particle Physics. *Lect. Notes Phys.*, 909:pp.1–172, 2016.
- [75] G Genard, P Descouvemont, and G Terwagne. S-factor measurement of the $^{13}\text{C}(p, \gamma)^{14}\text{N}$ reaction in reverse kinematics. *Journal of Physics: Conference Series*, 202(1):012015, 2010.
- [76] Christian Iliadis. *Nuclear Physics of Stars*. Wiley-VCH, 1 2008.
- [77] J.D. King, R.E. Azuma, J.B. Vise, J. Gorres, C. Rolfs, H.P. Trautvetter, and A.E. Vlieks. Cross section and astrophysical s-factor for the $^{13}\text{C}(p, \gamma)^{14}\text{N}$ reaction. *Nuclear Physics A*, 567(2):354 – 376, 1994.
- [78] Carl R. Brune and Daniel B. Sayre. Energy deconvolution of cross-section measurements with an application to the $^{12}\text{C}(\alpha, \gamma)^{16}\text{O}$ reaction. *Nuclear Instruments and Methods in Physics Research Section A: Accelerators, Spectrometers, Detectors and Associated Equipment*, 698:49 – 59, 2013.
- [79] D. Schürmann, L. Gialanella, R. Kunz, and F. Strieder. The astrophysical S factor of $^{12}\text{C}(\alpha, \gamma)^{16}\text{O}$ at stellar energy. *Physics Letters B*, 711(1):35 – 40, 2012.
- [80] Richard Deboer, Richard Azuma, C R Brune, H Costantini, J Görres, P J Leblanc, E Uberseder, Michael Wiescher, E C Simpson, and Claudio Ugalde. Azure, an R-matrix computer code. *PoS*, 01 2008.

Acknowledgements

È importante per me, alla fine di questo percorso, ringraziare le persone che hanno contribuito a questo lavoro, senza le quali non sarebbe stato possibile tutto ciò. Grazie mille alla Dottoressa Alba Formicola e al Professor Filippo Terrasi, che hanno “solamente” fatto il loro lavoro, ma con passione immensa, trasmettendomi l’entusiamo e la pazienza necessarii per raggiungere la meta. E son sicuro che il fatto di essere tutti del Sud ha fatto tantissimo. Spero di aver assorbito un po’ dei loro trucchi del mestiere.

Grazie al gruppo LUNA del Gran Sasso. Grazie Matthias Junker, Laszlo Csereki Donatello Ciccotti, Lucio di Paolo per aver vissuto con le le quotidianità.

Grazie infinite alla pazienza dei ragazzi dell’officina meccanica e del laboratorio di chimica per la meticolosità nella preparazione dei backing di Tantillo.

Un grande grazie al gruppo napoletano: Andreas Best , Gianluca Imbrani, Antonino Di Leva, Javier Balibrea Correa per avermi ospitato ed esser stati sempre presenti nonostante la distanza.

Anche a Napoli l’officina meccanica è stata fondamentale per la preparazione dei moderatori.

Thanks a lot to the MTA Atomki, mainly in the person of Dr Zsolt Fülöp and György Gyürky, for hosting me during the evaporation campaigns and teaching me secrets of target production and for the usage of the Tandem and the Van Der Graaf accelerators.

Grazie al Dott. Roberto Perrino, dell’INFN di Lecce, che mi ha avviato al mondo di Labview e senza il quale la programmazione della DAQ non sarebbe stata possibile.

A tutta la collaborazione LUNA va il mio grazie per il supporto, per i turni di misura e per il fatto di non essermi mai sentito solo.

Thanks a lot to the referees, for their precious comments that enriched the work.

Grazie a chi ai Laboratori Nazionali del Gran Sasso mi ha supportato e mi ha insegnato qualcosa, anche la cosa piú piccola.

Al GSSI grazie per avermi dato la possibilità di lavorare presso i Laboratori Nazionali del Gran Sasso, ambiente in cui si respira l’internazionalità della ricerca. Un ringraziamento speciale lo devo a Francesco Vissani che dal

primo momento non mi ha fatto sentire fuori luogo.

To all my PhD students colleagues and friends. It is beautiful to meet people coming from all over the World and be sure that we will meet again somewhere that still I do not know in the World. We are and we will be always a good team!!.

Alla mia famiglia, mamma, papá, Ciroluca, gli zii ma soprattutto ai nonni che non hanno capito ancora cosa faccio ma tifano “alla cieca”, anzi con il cuore.

A Marilicia per l'amore con cui mi segue SEMPRE, anche solo con il pensiero.